

NOVEL DIRECT REDOX FUEL CELL:
MEMBRANELESS LOW PRECIOUS METAL CATALYST
ELECTRODE ASSEMBLY

by

Mohammad Saad Dara

B.A.Sc., University of British Columbia, 2010

A THESIS SUBMITTED IN PARTIAL FULFILLMENT OF
THE REQUIREMENTS FOR THE DEGREE OF

MASTER OF APPLIED SCIENCE

in

THE FACULTY OF GRADUATE STUDIES
(Chemical and Biological Engineering)

THE UNIVERSITY OF BRITISH COLUMBIA
(Vancouver)

October 2012

© Mohammad Saad Dara, 2012

Abstract

The direct fuel redox fuel cell (DFRFC) substitutes the oxygen reduction cathode of low temperature fuel cells such as polymer electrolyte membrane fuel cells (PEMFC) and direct methanol fuel cells (DMFC) with an iron redox cathode of a redox flow battery. This approach helps address many of the issues with low temperature fuel cells. For both the PEMFC and DMFC the iron redox cathode eliminates precious metal content from the cathode. With respect to the PEMFC the inherent liquid nature of the iron redox cathode provides both heat and water management to the system which significantly reduces the balance-of-plant components. On the other hand, the issues of fuel crossover for the DMFC are no longer a concern as methanol is not electrochemically active at the carbon cathode used for the ferric reduction reaction. However, the use of metal redox ions in conjunction with a membrane of the same polarity introduces issues of membrane contamination which significantly reduce membrane conductivity resulting in increased ohmic overpotentials and losses in fuel cell performance. In addition, crossover of the redox catholyte can result in anode depolarization.

In this work a novel membraneless direct liquid redox fuel cell is demonstrated. The membraneless design utilizes 3-D electrode(s), the engineering of which allows control of the reactant concentration gradients. This control of the reactant gradient allows for more complete reactant utilization which mitigate catholyte crossover and allow for the elimination of the PEM. The PEM in the DFRFC used in this work is replaced with an open-spacer and liquid acid electrolyte. In addition, this novel membraneless electrode assembly design is completely scalable and flexible to different platforms, fuels, oxidants and electrolytes. In this work a membraneless direct hydrogen redox fuel cell and membraneless

direct methanol redox fuel cell based on the 3-D electrode concept and controlled concentration gradient are demonstrated. In addition, the use of the liquid acid electrolyte in the membraneless direct hydrogen redox fuel cell allowed for improved ionic conductivity to the anode catalyst layer. This allowed for significant reductions in precious metal catalyst content to be made from the hydrogen oxidation anode.

Preface

A portion of chapter 6.3 has been published. A. Lam, M. S. Dara, D.P. Wilkinson and K.Fatih (2012). Aerobic and Anaerobic Operation of an Active Direct Methanol Fuel Cell. *Electrochemistry Communications* 17:22-25. I, Mohammad Saad Dara, performed all the testing for the direct methanol redox fuel cell while a portion of the data for the direct methanol fuel cell was generated by Alfred Lam. I was responsible for writing of most of the transcript.

A portion of chapter 6.2 has also been submitted for publication. M. S. Dara, D.P. Wilkinson, A. Lam and K.Fatih (2012). Low Pt-loading Membraneless Hydrogen Redox Fuel Cell. *Electrochemical Society Transactions*, submitted July 2012. All data and experiments presented in this paper were performed by me. I was also responsible for the entire writing of this paper.

Table of Contents

Abstract.....	ii
Preface	iv
Table of Contents.....	v
List of Tables	viii
List of Figures.....	ix
Symbols and Nomenclature	xii
Glossary	xiv
Acknowledgements.....	xv
Dedication.....	xvi
1 Introduction.....	1
1.1 A Very Brief History of Fuel Cells.....	2
1.2 Types of Fuel Cells	4
1.3 Fundamental Principles of Fuel Cell Technology	8
1.4 Fuel Cell Thermodynamics: Effect of Temperature	10
1.5 Fuel Cell Thermodynamics: Effect of Pressure	11
1.6 Fuel Cell Thermodynamics: Effect of Concentration	12
1.7 Fuel Cell Thermodynamics: Efficiency	13
1.8 Fuel Cell Operating Fundamentals: Overpotential	15
1.8.1 Activation Overpotential	18
1.8.2 Ohmic Overpotential	21
1.8.3 Mass-transport Overpotential.....	23
1.9 Low Temperature Fuel Cells	24
1.9.1 The Polymer Electrolyte Membrane Fuel Cell	24
1.9.2 The Direct Methanol Fuel Cell.....	27
1.9.3 The Membrane Electrode Assembly	30
1.9.4 The Electrodes.....	31
1.9.5 The Membrane	35
1.10 Redox Flow Batteries.....	36
1.10.1 Electrolyte Requirements for Use in the Redox Flow Battery.....	39

1.10.2 Redox Flow Battery Electrodes.....	40
1.10.3 Redox Flow Battery Membrane	41
1.10.4 The Iron Chromium Redox Flow Battery	42
1.11 The Hybrid Redox Fuel Cell.....	46
2 Thesis Research Context.....	50
3 Objectives	51
4 Background to Thesis Research Approach.....	52
5 Experimental Approach and Methods	62
5.1 Fuel Cell Gaskets Fabrication.....	63
5.2 Electrode and Electrode Assembly Fabrication and Treatment.....	64
5.3 Electrolyte Preparation.....	66
5.4 Fuel Cell Testing System.....	67
6 Results and Discussions.....	72
6.1 Development of a Membraneless Electrode Assembly for an Active Fuel Cell System	72
6.1.1 Cell Architecture and Components	74
6.2 The Membraneless Direct Hydrogen Redox Fuel Cell.....	78
6.2.1 Effect of Iron Redox Catholyte Flow Rate.....	78
6.2.2 Repeatability of Experiments.....	82
6.2.3 Effect of Temperature	84
6.2.4 Effect of 3-D Cathode Thickness.....	90
6.2.5 Membraneless DHRFC vs. Conventional MEA DHRFC.....	93
6.2.6 Low Precious Metal Content Membraneless DHRFC	99
6.2.7 Effect of Humidification on Membraneless DHRFC.....	101
6.2.8 Fuel Cell Resistance	104
6.2.9 Apparent Exchange Current Density Calculations.....	110
6.2.10 Comparison with Incumbent PEMFC Technology.....	112
6.2.11 Durability Study for the Membraneless DHRFC.....	115
6.3 Demonstration of Flexibility of Membraneless Design.....	122
6.3.1 The Membraneless DMRFC	122
6.3.2 Comparison with Conventional MEA DMFC	130

6.3.3 Membraneless DMRFC Durability	132
7 Conclusions	134
8 Future Work and Recommendations	140
References.....	144
Appendix A – Catalyst Spraying Instructions	152
Appendix B – Detailed Dimensions of Flow Field Channels and Flow Field Plates.....	157
Appendix C – iR-Corrected Polarization and Power Density Curves	160
Appendix D – Publications and Presentations.....	167

List of Tables

Table 1.1: Summary of the range of operation, range of power application and key properties of different fuel cells	7
Table 1.2: A list of some commonly used reference electrodes.....	9
Table 1.3: Suggestions for redox couples that may be used in a RFB system.....	40
Table 6.1: Amount of ferric ions consumed at different current densities at different flow rates.....	81
Table 6.2: Effect of temperature on resistance and associated ohmic losses at different current densities.....	85
Table 6.3: Effect of humidification on resistance and associated ohmic losses at different current densities.....	102
Table 6.4: Summary of apparent exchange current densities for the ferric reduction reaction on carbon.....	111
Table 6.5: Comparison of the components used for the gas/liquid membraneless DHRFC and the liquid/liquid membraneless DMRFC.....	123

List of Figures

Figure 1.1: Schematic of the first demonstration of the fuel cell by Sir William Grove.....	2
Figure 1.2: Example polarization curve showing different contributing mechanisms to fuel cell performance losses. Also shown is the effect of improving performance in each of the characteristic regions on the polarization curve	15
Figure 1.3: Graphical representation of the Butler-Volmer equation.....	19
Figure 1.4: A schematic of the PEMFC along with the relevant electrochemical reactions	25
Figure 1.5: Schematic of a DMFC with the relevant electrochemical reactions	27
Figure 1.6: Schematic and operation of a generic redox flow battery.....	37
Figure 1.7: Schematic and relevant electrochemical reactions in a Fe/Cr Redox Flow Battery	42
Figure 1.8: A schematic of the DFRFC using the $\text{Fe}^{3+}/\text{Fe}^{2+}$ redox couple and methanol fuel with the relevant electrochemical reactions	46
Figure 4.1: Polytetrafluoroethylene chain that forms the Nafion backbone.....	53
Figure 4.2: Structure of Nafion showing the sulfonated side chain that allows proton conduction to be possible	53
Figure 4.3: Schematic showing the basic operation of laminar flow based fuel cells.....	56
Figure 4.4: Schematic showing the basic operation of mixed reactant fuel cells.....	58
Figure 4.5: Illustration of the thin-film triple phase boundary (TPB) showing poor utilization of catalyst due to a limited reaction zone	60
Figure 4.6: Illustration of a concentration gradient developing across the thickness of a 3-D electrode when liquid reactants are used.....	60
Figure 4.7: Illustration showing the proposed replacement of the membrane with a 3-D electrode structure, supporting electrolyte and an open-spacer	61
Figure 5.1: Schematic of the 4 cm ² fuel cell used for testing showing all components	69
Figure 5.2: Schematic of the direct methanol redox fuel cell testing system showing all components used for temperature, flow and pressure control.....	70
Figure 5.3: Schematic of the direct hydrogen redox fuel cell testing system showing all components used for temperature, flow and pressure control.....	71
Figure 6.1: Conceptual schematic of the membraneless electrode assembly utilizing the 3-D cathode, conventional anode and open-spacer in the DHRFC.....	77
Figure 6.2: Dynamic contact angle measurements of a Sigracet 25 DA GDL showing contact angle of 166°	77
Figure 6.3: Effect of iron redox catholyte flow rates on fuel cell performance at 60°C. a) Polarization and power density curves. b) Close-up of activation region.....	80
Figure 6.4: Fuel cell performance repeatability with new components for all three runs at 60°C.....	82
Figure 6.5: Fuel cell performance repeatability with the same membraneless electrode assembly at 60°C.....	83

Figure 6.6: Effect of temperature on fuel cell performance. a) Polarization and power density curves. b) Close-up of activation region	86
Figure 6.7: Effect of temperature on theoretical Nernst potential	87
Figure 6.8: Effect of temperature on conductivity of different iron salts	87
Figure 6.9: Effect of temperature and concentration of Fe^{3+} ions on theoretical cell Nernst potential	88
Figure 6.10: Effect of 3-D cathode thickness on fuel cell performance at 60°C	90
Figure 6.11: Schematic explanation of unutilized 3-D cathode contributing to fuel cell resistance with increasing current density.....	92
Figure 6.12: Comparison of fuel cell performance with the same electrode architectures with and without a Nafion 112 membrane at 60°C	93
Figure 6.13: Polarization curves of the Nafion® 112 DHRFC with and without a humidified hydrogen fuel.....	95
Figure 6.14: Comparison of polarization curves of the non-humidified fuel membraneless DHRFC with a humidified and non-humidified fuel Nafion® DHRFC.....	96
Figure 6.15: Effect of anode Pt catalyst content on fuel cell performance at 60°C	99
Figure 6.16: Effect of hydrogen fuel humidification on fuel cell performance for different anodes at 60°C . a) Polarization and power density curves. b) Close up of activation region.....	103
Figure 6.17: Membraneless DHRFC resistance and voltage as a function of bladder pressure using the membraneless electrode assembly with a 3.24 cm^2 square open-spacer with a catholyte and flow rate of 6 ml/min $2\text{ M Fe}(\text{ClO}_4)_3$ and a fuel flow rate of 105 ml/min non-humidified hydrogen.....	104
Figure 6.18: Comparison of iR-corrected and non-iR corrected fuel cell performance curves at 60°C	105
Figure 6.19: Membraneless DHRFC resistance as a function of LCR meter frequency with a catholyte and flow rate of 6 ml/min $2\text{ M Fe}(\text{ClO}_4)_3$ and a fuel flow rate of 105 ml/min non-humidified hydrogen.....	105
Figure 6.20: Conductivity of different concentrations of hydrochloric acid as a function of temperature.....	108
Figure 6.21: Conductivity of 0.5 M HClO_4 before bubbling with hydrogen and after bubbling with hydrogen as a function of temperature.....	109
Figure 6.22: Comparison of iR-corrected DHRFC and PEMFC polarization (a) and power density (b) curves at 60°C	114
Figure 6.23: Durability testing of the DHRFC under different current densities.....	117
Figure 6.24: Durability testing of the DHRFC under different current densities with expected degradation due to concentration change of the iron redox catholyte.....	119
Figure 6.25: Effect of catholyte state of charge (SOC) on membranless DHRFC performance.. ..	121
Figure 6.26: Comparison of different 3-D cathode architectures on membraneless DMRFC performance. a) Polarization and power density curves. b) Anode and cathode (iR-corrected) reference potentials	124
Figure 6.27: Different architectures for the 3-D cathode used in the membraneless DMRFC	125

Figure 6.28: Comparison of membraneless DMRFC performance with a conventional Nafion 117 based DMRFC. a) Polarization and power density curves. b) Anode and cathode (iR-corrected) reference potentials.....	128
Figure 6.29: Comparison of membraneless DMRFC performance with a membraneless and Nafion® 117 DMFC	130
Figure 6.30: 4 hour durability of the membraneless DMRFC and DMFC at 100 mA/cm ²	132
Figure B.1: Detailed drawings of the anode flow channels.....	158
Figure B.2: Detailed drawings of the cathode flow channels.....	159
Figure C.1: iR-corrected polarization curves for the effect of iron redox catholyte flow rates of fuel cell performance at 60°C	161
Figure C.2: iR-corrected fuel cell performance repeatability with new components for all three runs at 60°C.....	161
Figure C.3: iR-corrected fuel cell performance repeatability with the same membraneless electrode assembly at 60°C	162
Figure C.4: iR-corrected polarization curves for the effect of temperature on fuel cell performance.....	162
Figure C.5: iR-corrected polarization curves for the effect of 3-D cathode thickness on fuel cell performance at 60°C.....	163
Figure C.6: iR-corrected comparison of polarization curves of the non-humidified fuel membraneless DHRFC with a humidified and non-humidified fuel Nafion® 112 DHRFC.....	163
Figure C.7: iR-corrected polarization curves showing the effect of anode Pt catalyst content on fuel cell performance at 60°C	164
Figure C.8: Effect of hydrogen fuel humidification on fuel cell performance for different anodes at 60°C.....	164
Figure C.9: iR-corrected comparison of different 3-D cathode architectures on membraneless DMRFC performance.....	165
Figure C.10: iR-corrected comparison of membraneless DMRFC performance with a conventional Nafion 117 based DMRFC	166

Symbols and Nomenclature

$(\text{SO}_3)^-$	Sulfonic group
$(\text{SO}_4)^{2-}$	Sulfate
a	Activity
A	electrode area (cm^2)
C_B	Bulk concentration of the electroactive species (mol/cm^3)
Cl^-	Chloride
C_R^*	Reactant concentration at the catalyst surface (mol/cm^3)
D	diffusion coefficient (cm^2/s)
E	Electrochemical Potential (V)
E°	Standard Electrode Potential (V)
E°_{cell}	Standard Cell Potential (V)
F	Faraday constant (96485 C mor^{-1})
Fe^{2+}	Ferrous
Fe^{3+}	Ferric
G	Gibbs Free Energy (kJ)
H	Enthalpy (kJ)
H^+	Proton
HClO_4	Perchloric Acide
I	Current (A)
i	Current Density (mA/cm^2)
i_L	limiting current density (amps/cm^2)
i_o	exchange current density (amps/cm^2)
k_m	Mass transfer coefficient (m/s)
n	number of electron involved in the electrode process
P	Pressure (kPa)
P	Power density (mW/cm^2)
P_1, P_2	Pressure at state 1, Pressure at state 2 (kPa)
R	Ideal gas constant ($8.314 \text{ J K}^{-1} \text{ mol}^{-1}$) or general resistance (ohm)
Pol.	Polarization of cell
R_{cell}	Cell Resistance (ohms)
S	Entropy (kJ)
s	Stoichiometric coefficient
T	Temperature (K)
t	Time (seconds)
V	Volume (cm^3)
Φ_i	Current efficiency (dimensionless)
Φ_{overall}	Overall efficiency (dimensionless)
Φ_r	Reactant efficiency (dimensionless)
Φ_{th}	Thermodynamic efficiency (dimensionless)

Φ_v	Voltage efficiency (dimensionless)
α_a	Anodic charge transfer coefficient (dimensionless)
α_c	Cathodic charge transfer coefficient (dimensionless)
η	overpotential (Tafel equation)

Glossary

AFC	Alkaline Fuel Cell
CCM	Catalyst Coated Membrane
CERC	Clean Energy Research Centre
CHBE	Chemical and Biological Engineering
DFRFC	Direct Fuel Redox Fuel Cell
DHRFC	Direct Hydrogen Redox Fuel Cell
DMFC	Direct Methanol Fuel Cell
DMRFC	Direct Methanol Redox Fuel Cell
GDL	Gas Diffusion Layer
HHV	High Heating Value
HOR	Hydrogen Oxidation Reaction
LHV	Low Heating Value
MCFC	Molten Carbonate Fuel Cell
MEA	Membrane Electrode Assembly
MOR	Methanol Oxidation Reaction
MPL	Micro-porous Layer
NSERC	Natural Sciences and Engineering Research Council
OCV	Open Circuit Voltage
ORR	Oxygen Reduction Reaction
PAFC	Phosphoric Acid Fuel Cell
PEMFC	Polymer Electrolyte Membrane Fuel Cell
PGM	Precious Group Metal
PTFE	Polytetrafluoroethylene
SOC	State of Charge
SOFC	Solid Oxide Fuel Cell
TPB	Triple Phase Boundary
TPS	Triple Phase Site
UBC	University of British Columbia

Acknowledgements

Football fans after a game often speak about that one moment that turned the tie in their team's favor. But of course that moment is only ever recognized as a turning point in hind sight. For me that moment was near the end of the third year of my undergraduate degree when Dr. David Wilkinson offered me a position as a summer research assistant. That summer I worked alongside then PhD student, Dr. Alan Ilicic. Alan introduced me to many new fundamentals of electrochemistry and was responsible for me developing a deeper interest in electrochemistry. However, it was the beginnings of a career path Dr. Wilkinson allowed me to envision that was for my education a turning point. Since then, his guidance, mentorship and encouragement have tremendously assisted me in my endeavors. This thesis is a small reflection of that.

I have also had the fortune of being surrounded by some extremely gifted colleagues. Their knowledge and intelligence in their respective fields is without question exemplary. The day to day advice that I have received from Alfred Lam and Arman Bonakdarpour has been extremely important for this project. But it is the interest they show you when you approach them, the integrity of their characters and their ability to ensure an enjoyable work-place that sets them apart. The advice provided by Dr. Khalid Fatih of NRC has also been very valuable to the success of this project. I have also had the pleasure of getting to know Greg Afonso, David Bruce, Caroline Cloutier, Simon Fan, Tyler Lewis, Winton Li and Steve Reaume who have made this part of my life an incredibly enjoyable one. I hope they remain a part of my life in the future.

Finally, I wish to mention a few words about my family. Words cannot express the debt of gratitude I owe to my parents. Any success I achieve is a consequence of their guidance, patience, faith and unwavering support. They have made countless sacrifices to ensure their children receive the best possible education. They are a source of inspiration in how to lead your personal and professional lives. My sisters have been for me a source of support and pride. They are a moral barometer that I can always look to for the right course of action.

To my mother

1 Introduction

Gordon E. Moore, the cofounder of Intel, in his 1965 paper described a long-term trend in computing hardware [1]. This trend, which became known as ‘Moore’s Law’, predicted that the numbers of transistors that can be inexpensively placed on an integrated circuit will double every two years. In the over four decades since that paper, his prediction has proved to be uncannily accurate. This trend has allowed for an exponential growth in computing capability of portable electronics such as cell phones, portable music players and laptops that have been made available to the public at increasingly affordable prices. However, the increased ability in computing power has meant an increased demand for higher capacity and longer lasting portable power devices. Currently, rechargeable lithium ion batteries are most commonly used but these are not expected to meet future power demands.

Furthermore, increasing energy demands in both the developed and developing world are reaching a level that not only cannot be sustained by fossil fuel derived power but is also believed to be doing irreversible damage to our environment. Though few may dispute the claim that global warming is a consequence of society’s over-reliance on fossil fuel combustion power it is indisputable that other alternatives to meet our power demands are required. Many renewable alternatives such as solar, wind and tidal power have been proposed. However, the intermittent nature of these energy generation processes has left a large gap in the production, storage and supply of this energy reliably. As such storage and subsequent release of this energy at appropriate times is required. Therefore, an increased need for all types of energy conversion and storage devices for grid-level, stationary,

portable and backup power devices not reliant on dwindling fossil fuel reserves have emerged. One such technology capable of meeting a wide-range of these requirements is the fuel cell.

1.1 A Very Brief History of Fuel Cells

Fuel cells are energy conversion devices that convert chemical energy into electricity, heat and some chemical by-products. A fuel stream (e.g., hydrogen, methanol, formic acid, etc.) is oxidized at the anode and an oxidant is reduced at the cathode. Unlike batteries which store energy in the form of a chemical, fuel cells operate continuously without a need for recharge as long as fuel and oxidant are supplied to the electrochemical reactor from an external source.

The first demonstration of the fuel cell dates back to 1839 when Welsh scientist Sir William Grove developed the “gas battery” where hydrogen and oxygen gas reacted over platinum in a sulfuric acid electrolyte [2]. This device was used to power a water electrolyzer and a schematic along with the reactions involved may be found in Figure 1.1.

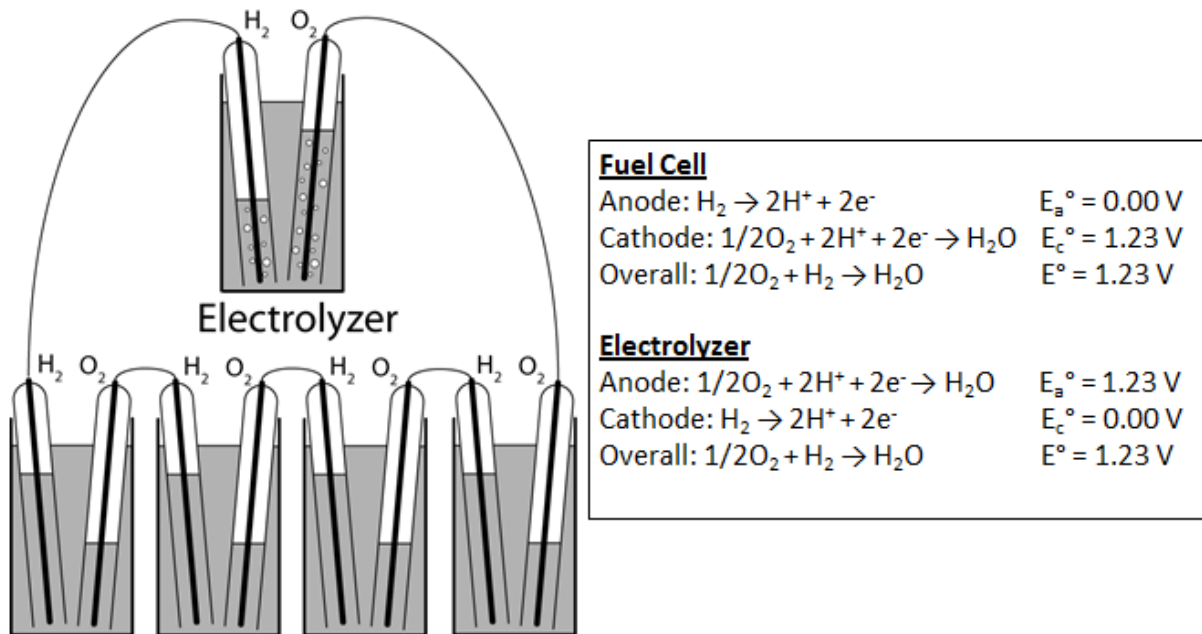


Figure 1.1: Schematic of the first demonstration of the fuel cell by Sir William Grove.

After this discovery much work over the next 80 years was performed on promoting fuel cell technology most notably by Mond and Langer [3]. However, it was not until Francis T. Bacon's work at Cambridge in the 1950s with the invention of the high temperature alkaline hydrogen air fuel cell that fuel cells really started to attract significant attention. After Bacon developed a scale-up of his technology into a 5 kW system for forklifts fuel cell technology was used in applications for the first time when the National Aeronautics Space Administration (NASA) decided to use it on its Apollo missions during the 1960s [4]. While this alkaline technology was evolving the proton exchange membrane was also invented by William Grubb at General Electric in the late 1950s which was designed for use in an acidic hydrogen air fuel cell [5, 6]. Once again NASA was at the forefront of application of this technology using it on their Gemini spacer missions to provide on-board power. With these advances the modern proton exchange membrane fuel cell (PEMFC) was born.

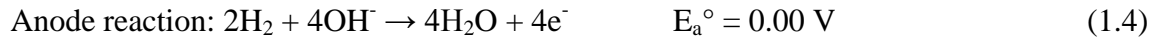
1.2 Types of Fuel Cells

Polymer electrolyte membrane fuel cells (PEMFC) use hydrogen and oxygen with the electrochemical reactions as shown in equations (1.1)-(1.3). They can be operated at temperatures up to 130°C (though they are usually operated below 80°C) and are considered for a wide-range of transportation, stationary and portable power applications. They use ion-exchange membranes as the electrolyte and often require significant balance-of -plant (BOP) components for fuel, heat and water management in the system. Fuel and oxidant flow through the flow fields provides the reactants to the platinum catalyst based electrodes. Proton transport through the proton-exchange membrane to the cathode maintains charge neutrality while its combination with oxygen produces water at the cathode. PEMFCs will be discussed in more detail later.



Direct methanol fuel cells (DMFC) also operate in a similar temperature range as PEMFCs but utilize methanol as the fuel instead of hydrogen without the use of a fuel processing system. The term ‘direct’ refers to the ability of these fuel cells to use methanol fuel directly as opposed to a fuel processing system which uses methanol to supply hydrogen to a H₂/O₂ system. The catalyst at the anode is a platinum and ruthenium mixture which reduces issues with carbon monoxide poisoning of pure Pt-catalyst electrodes. A PEM is used for the electrolyte though the use of a liquid fuel introduces other issues related to overall fuel cell efficiency due to fuel crossover. DMFCs will also be discussed in detail later.

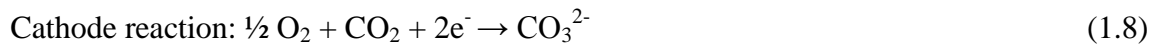
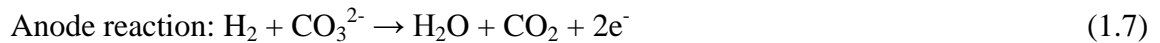
Alkaline fuel cells (AFCs) are operated at a temperature over 65°C up to 250°C. Here, a potassium hydroxide electrolyte which is stored in some matrix (e.g., SiC) is used. The concentration of this electrolyte usually determines the operating temperature of the fuel cell. Like PEMFCs, the AFC uses hydrogen and oxygen as the fuel and oxidant, respectively. But unlike PEMFCs where proton exchange occurs, hydroxide ion exchange occurs through the electrolyte in an AFC. The electrochemical reactions at the anode and cathode are also different as shown in equations (1.4)-(1.6). The product of the fuel cell reaction is still only water. Challenges with AFCs include system and material stability. The possible reaction of CO and CO₂ as impurities in the fuel with the electrolyte can result in potassium carbonate formation. In addition CO₂ impurities in the air can result in carbonate formation at the cathode as well.



Phosphoric acid fuel cells (PAFCs) use as the name suggests phosphoric acid in some matrix as the electrolyte. This allows fuel cell operation at temperatures greater than 150°C due to the stability of the acid at high temperatures. High temperature operation offers several advantages including improved ionic conductivity, reduced effects of CO poisoning of the Pt-catalyst and reduced water management issues as the products are in the vapour phase.

Molten carbonate fuel cells (MCFCs) use different carbon-based fuels (e.g., natural gas, biogas, etc.) and operate at elevated temperatures greater than 600°C using non-precious group metal catalysts and some ceramic matrix to store a carbonate conductive electrolyte

such as lithium carbonate among others. The reactions for a MCFC are shown in equations in (1.7)-(1.9). MCFCs offer several advantages including much higher efficiencies, improved kinetics of the oxygen reduction reaction, ability to use fuels with impurities and reduced vulnerability to CO poisoning due to elevated temperatures. However, elevated temperatures and the corrosive nature of the electrolyte also bring with them system durability issues that make MCFCs less appealing.



Finally, solid oxide fuel cells (SOFCs) operate at a wider range of temperatures than those of MCFCs which can sometimes be as high 850°C. The reactions for a SOFC are shown in equations (1.10)-(1.12). SOFCs use a solid oxide electrolyte (usually some non-porous metal oxide) capable of conducting oxide ions. Like MCFCs, SOFCs do not require PGM-catalysts and the anode and cathode are usually made of yttria stabilized zirconia and lanthanum strontium manganite, respectively. The anode oxidises hydrogen fuel which may be supplied by a hydrocarbon source while the cathode uses an oxygen stream. SOFCs in addition to the advantages common with MCFCs are resistant to sulfur-based impurities allowing the use of fuels derived from coal. However, similar to MCFCs, the SOFC also suffers from durability issues and slow start-up related to elevated temperatures. Table 1.1 provides a summary of the range of operation, key properties and the range of power applications for different fuel cells.



Table 1.1: Summary of the range of operation, range of power application and key properties of different fuel cells.

Fuel Cell	Fuel	Conducting Ion	Operating Temperature (°C)	Power Range (kW)
AFC	H ₂	H ⁺	50-200	1-10
PEMFC	H ₂	H ⁺	30-120	0.001-1000
PAFC	H ₂	H ⁺	200	10-1000
DMFC	CH ₃ OH	H ⁺	20-90	0.001-0.1
MCFC	H ₂	CO ₃ ²⁻	650	1000-10000
SOFC	H ₂ , CO, CH ₄	O ²⁻	500-800	1-10000

1.3 Fundamental Principles of Fuel Cell Technology

Fuel cells follow the basic laws of electrochemistry where a reaction always occurs between an oxidized (Ox) and reduced (Red) species at an electrode/electrolyte interface. At this interface a reaction proceeds by either liberation or consumption of electron(s). In essence fuel cells are a type of galvanic cell in which reactions proceed spontaneously with the completion of an external electrical circuit. This self-driving reaction is what creates electron flow in the external circuit which when connected to an external load allows for useful work to be performed in different energy forms. The electromotive force for this spontaneous cell can be related to the summation of Gibbs free energy of formation of the oxidized ($\Delta G_{f,Ox}^{\circ}$) and reduced ($\Delta G_{f,Red}^{\circ}$) species involved in the cell:

$$\Delta G_{cell}^{\circ} = \sum \Delta G_{f,Red}^{\circ} - \sum \Delta G_{f,Ox}^{\circ} \quad (1.13)$$

The Gibbs free energy change of the cell is related to the standard (298 K, 1 atm) reversible cell potential, E°_{cell} by the expression:

$$\Delta G_{cell}^{\circ} = -nFE_{cell}^{\circ} \quad (1.14)$$

where n is the number of electrons transferred in the reaction and F is Faraday's constant equal to 96485 Coulombs/mol. As the system proceeds to a more "stable" state in a spontaneous system the change in the cell's Gibbs free energy will be negative and thus its reversible cell potential will be positive. By convention the reversible cell potential, E°_{cell} , is defined as the difference between the working and counter electrodes. In fuel cell parlance the cathode, where the reduction reaction takes place is defined as the working electrode while the anode where oxidation takes place is defined as the counter electrode. Thus if electron flows from the anode to the cathode then,

$$E^{\circ}_{cell} = E^{\circ}_{cathode} - E^{\circ}_{anode} \quad (1.15)$$

where $E^{\circ}_{\text{cathode}}$ and E°_{anode} are the standard cathode and anode potentials, respectively, and may be calculated from their appropriate Nernst equations.

The overall fuel cell reaction is a combination of the anodic and cathodic half-cell reactions. As in all of electrochemistry; where absolute single electrode potentials do not exist, potentials are measured against some arbitrary value, i.e., half-cell reactions must be measured against some reference electrode. The reference electrode itself though has its own potential which is measured against the standard hydrogen electrode (SHE), which is given a value of 0 V. A list of some reference electrode potentials can be found in Table 1.2.

Table 1.2: A list of some commonly used reference electrodes.

Abbreviation	Half-cell Reaction	Potential (V vs. SHE)	Electrolyte
Hg/Hg ₂ SO ₄	Hg ₂ SO _{4(s)} + 2e ⁻ → 2Hg _(l) + SO ₄ ²⁻	0.67	Sat'd K ₂ SO ₄
Cu/ CuSO ₄	Cu ²⁺ + 2e ⁻ → Cu _(s)	0.32	Sat'd CuSO ₄
SCE	Hg ₂ Cl _{2(s)} + 2e ⁻ → 2Hg _(l) + Cl ⁻	0.24	Sat'd KCl
Ag/AgCl	AgCl _(s) + e ⁻ → Ag _(s) + Cl ⁻	0.20	Sat'd KCl
Hg/HgO	HgO _(s) + H ₂ O + 2e ⁻ → Hg _(l) + 2OH ⁻	0.14	1 M NaOH
SHE	2H ⁺ + e ⁻ → H _{2(g)}	0.00	[H ⁺] = 1 M

So far fuel cell voltage has only been discussed at ideal conditions. However, fuel cell operation rarely occurs at ideal conditions where the effect of temperature, pressure and concentration can be substantial. The role of these parameters on cell voltage is shown below but if detailed derivations of the equations are required they can easily be found in the literature [7, 8].

1.4 Fuel Cell Thermodynamics: Effect of Temperature

Temperature plays an important role in determining the half-cell potential and thus fuel cell potential. Temperature effects can be seen not only with respect to a change in Gibbs free energy but also with regards to ionic conductivity, electrical conductivity and mass transport. To analyze the effect of temperature on reaction cell potential one may begin with writing the relationship between cell potential and Gibbs free energy with respect to change in temperature,

$$\frac{\partial \Delta G}{\partial T} = -nF \frac{\partial E}{\partial T} \quad (1.16)$$

Realizing that the change in Gibbs free energy with respect to temperature is related to entropy and rearranging equation 1.16 the following may be written,

$$\frac{\Delta S}{nF} = \frac{\partial E}{\partial T} \quad (1.17)$$

Finally integrating equation 1.17 with respect to temperature an equation for cell potential with respect to temperature is as follows,

$$E_T^\circ = E^\circ - \frac{\Delta S^\circ}{nF} (T - T^\circ) \quad (1.18)$$

where E° is the standard reversible cell potential and T° is 298.15 K. The change in entropy, S , with respect to temperature is negligible and so can be ignored. As an approximation the standard change in entropy, ΔS° , may be used.

1.5 Fuel Cell Thermodynamics: Effect of Pressure

When gaseous fuels or oxidants are used in a fuel cell their partial pressures are usually not those at ideal conditions, i.e., some pressure other than 101.3 kPa. In these cases corrections to reaction potential must be made. One may begin in a similar manner to temperature to derive the dependence of equation 1.14 with respect to pressure to achieve,

$$\frac{\partial \Delta G}{\partial P} = -nF \frac{\partial E}{\partial P} \quad (1.19)$$

Once again realizing the change in Gibbs free energy with respect to pressure is related to volume and rearranging equation 1.19 the following equation is derived,

$$\frac{-\Delta V}{nF} = \frac{\partial E}{\partial P} \quad (1.20)$$

This equation can be integrated if the gas is assumed to be ideal allowing for use of the ideal gas law (1.21),

$$\Delta V = \frac{\Delta nRT}{P} \quad (1.21)$$

which is applied to equation 1.20 to give,

$$\frac{-\Delta nRT}{nFP} = \frac{\partial E}{\partial P} \quad (1.22)$$

Equation 1.22 can then be integrated to give the dependence of reaction potential on pressure in the form,

$$E_{e,P2} = E_{T,P1}^{\circ} - \frac{RT}{nF} \ln \left(\frac{P2}{P1} \right) \quad (1.23)$$

where R = ideal gas constant and T = operating temperature in K, and P1 and P2 are the pressures in kPa.

1.6 Fuel Cell Thermodynamics: Effect of Concentration

Reactant concentrations are usually not at ideal conditions and changes in reaction potential with respect to concentration should be accounted for. The reactant concentration has an effect on the activity of the reactant species and as such the fundamental thermodynamic equation relating activity of species to the change in Gibbs free energy, equation 1.24, is used to derive an expression for the effect of concentration on reaction potential.

$$\Delta G = \Delta G^\circ + RT \ln \left(\frac{\prod a_{products,j}^{S_{red,i}}}{\prod a_{products,i}^{S_{ox,i}}} \right) \quad (1.24)$$

Combining this equation with equation 1.14 gives the Nernst equation which describes the effect of concentration on reaction potential,

$$E = E_T^\circ - \frac{RT}{nF} \ln \left(\frac{\prod a_{products,j}^{S_{red,i}}}{\prod a_{products,i}^{S_{ox,i}}} \right) \quad (1.25)$$

where R is the ideal gas constant, T is the temperature in K, n is the number of electrons transferred and F is Faraday's constant (96485 Coulombs/mole).

The activity of different species depends on the reactants and can be summarized as follows:

$$\begin{aligned} \text{Ideal gas: } a_i &= P_i/P_{\text{reference}} \\ \text{Non-ideal gas: } a_i &= y_i P_i/P_{\text{reference}} \\ \text{Ideal solution: } a_i &= C_i/C_{i,\text{reference}} \\ \text{Non-ideal solution: } a_i &= y_i C_i/C_{i,\text{reference}} \\ \text{Solute/ Solvent: } a_i &= 1 \end{aligned}$$

where P_i is pressure in kPa, $P_{i,\text{reference}} = 101.3$ kPa, C_i = concentration in mol/l, $C_{i,\text{reference}} = 1$ mol/l, and y_i = activity coefficient.

1.7 Fuel Cell Thermodynamics: Efficiency

Fuel cell thermodynamic efficiency, ϕ_{th} , refers to the theoretical maximum efficiency that can be achieved with a fuel cell. This is related to the change in enthalpy, H, and Gibbs free energy, G, of the system as follows,

$$\phi_{th} = \frac{\Delta G}{\Delta H} \quad (1.26)$$

This equation can be written for a fuel cell in the form

$$\phi_{th} = \frac{-nFE}{\Delta H} \quad (1.27)$$

where E is the reversible open circuit voltage, F is Faraday's constant (96485 Coulombs/mole) and n is the number of electrons transferred during the reaction.

During calculations of this nature it is important to know the phase of the reactants and products as this can have a large impact on both the enthalpy and Gibbs free energy. The most common occurrence of this involves water generation in PEMFCs (or combustion processes) where the lower heating value (LHV), when water is produced in the gaseous phase and the higher heating value (HHV), when water is produced in the liquid phase must be considered.

Fuel cells almost never operate at conditions of thermodynamic efficiency as other efficiency losses contribute to the overall efficiency as well. These are as follows:

- Current efficiency: ϕ_i , refers to the contribution of the desired reaction to the overall current of the fuel cell. A low current efficiency is associated with the presence of strong unwanted side reactions.
- Voltage efficiency: ϕ_v , refers to all the contributing losses to fuel cell voltage during operation.

- Reactant utilization: ϕ_r , refers to the amount of reactant consumed compared to the amount of reactant supplied and can be defined as follows,

$$\phi_r = \frac{nFC_iV_i}{s_iI} \quad (1.28)$$

where n is the number of electrons transferred, F is Faraday's constant (96485 Coulombs/mole), C_i is the concentration in mol/m³, V_i is the reactant flow rate in m³/s, I is the current in A and s_i is the stoichiometric coefficient.

- Overall fuel cell efficiency: $\phi_{overall}$, is the multiplication of these individual terms as follows,

$$\phi_{overall} = \phi_{th}\phi_i\phi_v \prod \phi_{r,j} \quad (1.29)$$

1.8 Fuel Cell Operating Fundamentals: Overpotential

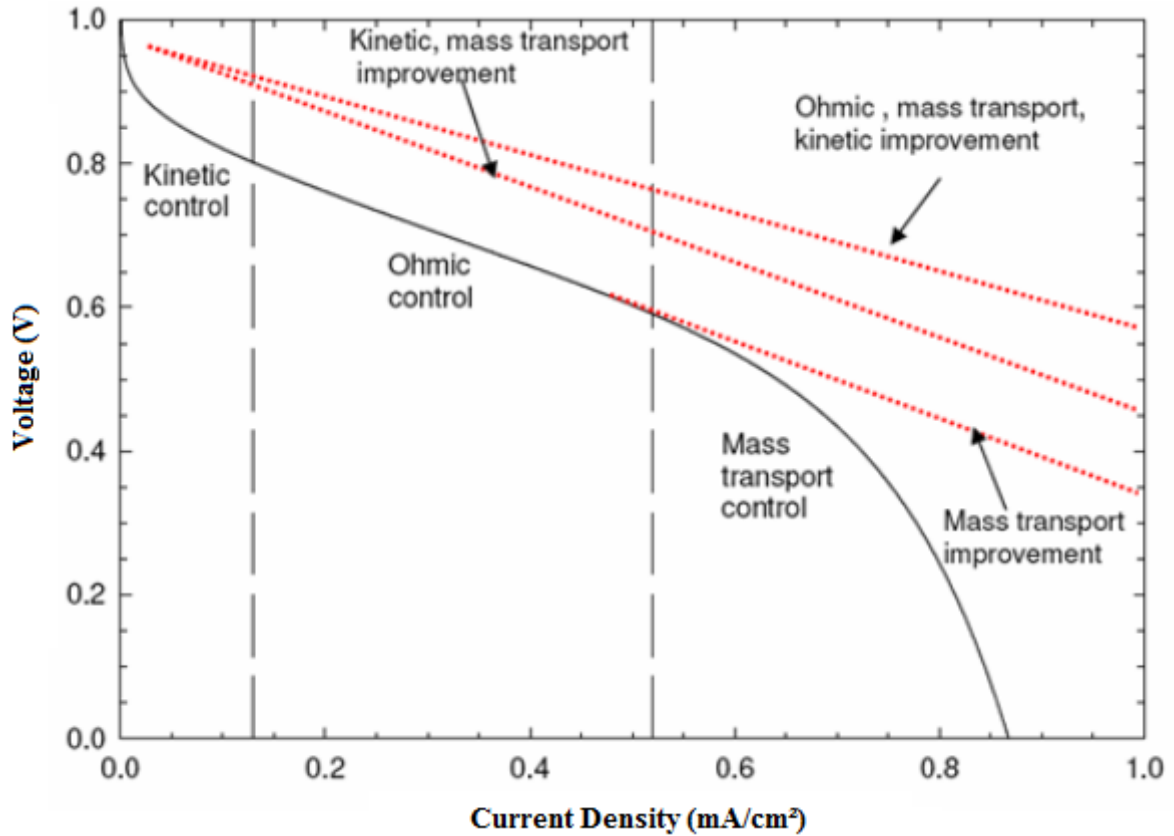


Figure 1.2: Example polarization curve showing different contributing mechanisms to fuel cell performance losses. Also shown is the effect of improving performance in each of the characteristic regions on the polarization curve.

Fuel cells are complex systems with many factors affecting their operating voltage. These include among other factors electrode design, catalyst loading, flow channel design, operating temperature, pressure compression, reactant utilization, product removal, membrane conductivity, solution conductivity and reactant crossover.

Fuel cell operating voltage at open circuit or open circuit voltage (OCV) refers to the cell voltage when no load is applied to the fuel cell, i.e., a current density of 0 mA/cm². It would be expected that the voltage under this condition should equal the theoretical equilibrium cell voltage, E_{cell} , however, this is seldom the case. This is due to reactant

impurities, corrosion or degradation of the electro-catalyst at high voltages and/or reactant crossover. First, impurities in the system can create their own potential resulting to contributions to the overall cell voltage which shift the OCV. Second, in addition to loss of reactant, crossover of the reactant through the membrane can result in electrode depolarization due to mixed-potentials in the system by shifting the potential of the opposite electrode (fuel crossover – cathode depolarization, oxidant crossover – anode depolarization). These shifts result in a discrepancy between the measured OCV and the theoretical equilibrium cell voltage while the magnitude and direction of the shift indicates the degree of crossover and impurities, and the contributing reactant(s).

Voltage losses in a fuel cell under load occur due to different mechanisms. These losses are termed overpotential and can apply to an electrolytic or galvanic cell. In a galvanic cell such as a fuel cell overpotential refers to the amount of energy that is lost compared to what would be predicted by thermodynamic values. There are three main mechanisms that lead to voltage losses in a fuel cell; kinetic or activation overpotentials, ohmic overpotentials, and concentration or mass-transport overpotentials. These can be written in terms of the cell potential as follows:

$$E_{\text{cell}} = E_c - E_a - |\eta_{\text{c,s}}| - |\eta_{\text{a,s}}| - IR_{\text{cell}} - |\eta_{\text{c,c}}| - |\eta_{\text{a,c}}| \quad (1.30)$$

where $|\eta_{\text{c,s}}|$ is cathodic activation overpotential, $|\eta_{\text{a,s}}|$ is anodic activation overpotential, $|\eta_{\text{c,c}}|$ is the cathodic concentration overpotential, $|\eta_{\text{a,c}}|$ is the anodic concentration overpotential, I is the operating current in Amps, and R_{cell} is the internal cell resistance in ohms.

Fuel cell performance is evaluated by the development of characteristic polarization and power density curves. Polarization curves, an example of which is shown in Figure 1.2, are generally galvanostatic measurements of steady state voltage for different operating

conditions. Fuel cell voltage losses due to the different mechanisms (activation, ohmic, mass-transport) can be seen in three distinct regions of the polarization curve. These voltage losses are discussed in detail later in this section.

Power density curves are used to demonstrate the peak power a fuel cell may be able to provide. Power, P , can be calculated by:

$$P = iE_{\text{cell}} \quad (1.31)$$

where E_{cell} = equilibrium cell voltage and i is the operating current density in A/cm².

1.8.1 Activation Overpotential

The Butler-Volmer equation defines the activation overpotential in terms of the temperature, T, current density, i, and the reaction mechanism with the following relationships,

$$i = i_o \left[\exp\left(\frac{\alpha_a F}{RT} \eta_s\right) - \exp\left(\frac{\alpha_c F}{RT} \eta_s\right) \right] \quad (1.32)$$

$$\alpha_a = (1 - \beta_s)n \quad (1.33)$$

$$\alpha_c = \beta_s n \quad (1.34)$$

where β_s is the symmetry factor describing which of the anodic or cathodic processes is favoured, α_a and α_c are the charge transfer coefficients, n is the number of electrons transferred in the rate determining step, η_s is the overpotential in V, F is Faraday's constant (96485 Coulombs/mole), R is the ideal gas constant, T is temperature in K and i_o is the exchange current density in A/m². The Butler-Volmer equation is represented graphically as shown in Figure 1.3.

Here, the region, $|\eta_s| \geq 50 \text{ mV}$, has a linear approximation and is represented by the Tafel equation,

$$|\eta_s| = b(\log |i|) + a \quad (1.35)$$

$$b = \frac{2.303RT}{\alpha F} \quad (1.36)$$

$$a = b(\log i_o) \quad (1.37)$$

For cathodic processes, $|\eta_s| = -\eta_{s,c}$; $\alpha = \alpha_c$; $|i| = -i_c$ while for anodic processes, $|\eta_s| = \eta_{s,a}$; $\alpha = \alpha_a$; $|i| = i_a$.

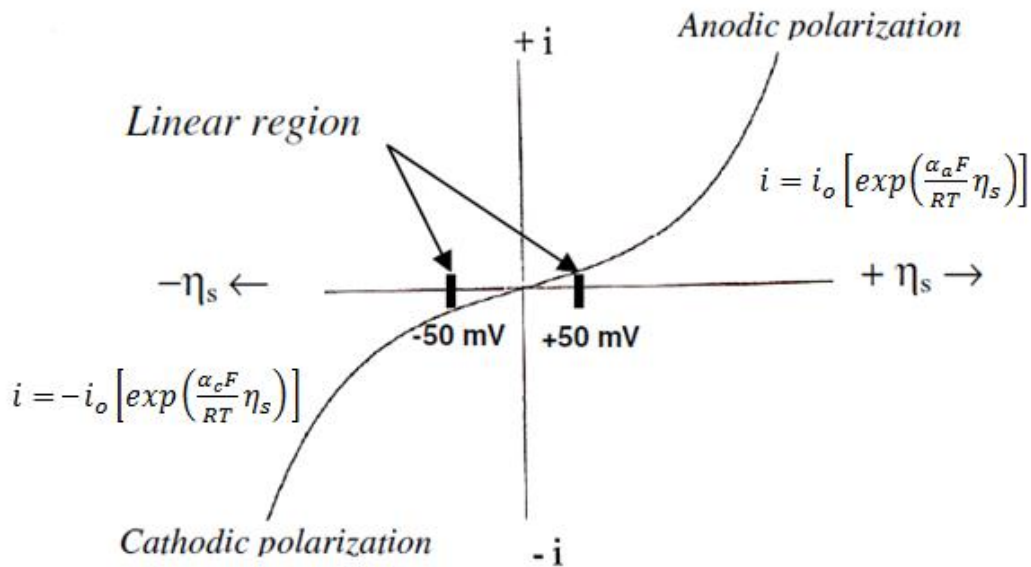


Figure 1.3: Graphical representation of the Butler-Volmer equation.

Under activation control, when the concentration of the reactant can be assumed to be the same at both the electrode surface and bulk solution the Tafel slope, b , and intercept, a , are used to indicate the effectiveness of electrode design at lowering the activation overpotential as low as possible. An electrode with a low Tafel slope, b and a high exchange current density, i_o , are desired. Exchange current density is defined as “the rate of exchange between the reactant and product states at equilibrium”. It includes several terms and can be written in the form:

$$i_o = nF c_R^* e^{-\frac{\Delta G^\ddagger}{RT}} \quad (1.38)$$

where c_R^* is the reactant surface concentration and ΔG^\ddagger is the activation barrier. Successful fuel cell design minimizes activation overpotentials by having a high exchange current density, i_o . Strategies for reducing activation overpotentials include:

1. Increasing reactant concentration which linearly increases exchange current density

2. Decreasing the activation barrier by using catalysts that have a high exchange current density associated with the desired reaction
3. Increasing temperature to provide more thermal energy to the reactants which increases the exchange current density
4. Increasing the number of potential reaction sites. As the reaction occurs on a surface area basis increasing the surface area of the catalyst but keeping the geometric area constant can have a large impact on the exchange current density.

1.8.2 Ohmic Overpotential

Ohmic overpotentials refer to voltage losses due to the resistance of all the electronic and ionic components in the system and can be written as an equation in the form,

$$iR_{cell} = i \sum_n R_n = i \sum_n \frac{\tau}{\kappa A} \quad (1.39)$$

where R_{cell} is the overall cell resistance in ohms, τ is the thickness of the component in cm, κ is the specific conductivity of the component in S/cm and A is the geometric area in cm².

Most conventional low temperature fuel cells utilize polymer electrolyte membranes. The conductivity of a polymer electrolyte membrane is dependent on its hydration levels which in turn is dependent on temperature. The specific conductivity, κ_{PEM} of a Nafion® PEM can be given by the following expression,

$$\kappa_{PEM} = (0.46\lambda_w - 0.25) \exp \left[-1190 \left(\frac{1}{T} - \frac{1}{298} \right) \right] \quad (1.40)$$

where λ_w = water content and T is temperature in K.

In this thesis a liquid electrolyte is used not only as the fuel or oxidant medium but also as a means for ionic conduction to replace the need for a membrane. As such its conductivity which is dependent on temperature, concentration, inerts and void fraction is an important consideration. The complete dissociation of a binary electrolyte can be shown as follows,



For dilute solutions with a concentration less than 1 mol/dm³, the specific conductivity of the solution, κ_s , can be expressed as follows,

$$\kappa_s = F^2 \sum_j z_j^2 u_j^2 C_j \quad (1.42)$$

where z_j is the charge of species j , u_j is the ionic mobility of species j in m²mol/Js and C_j is the concentration of species j in mol/m³.

When concentrated solutions are used ion-ion interactions can have a large effect on solution conductivity. This dependence of conductivity, κ , on concentration is described by the Casteel-Amis equation,

$$\kappa = \kappa'_{max} \left(\frac{C}{C'_{max}} \right)^x \exp \left[y(C - C'_{max})^2 - \frac{x}{C'_{max}} (C - C'_{max}) \right] \quad (1.43)$$

$$\kappa'_{max} = \kappa_{max1} + \kappa_{max2}T \quad (1.44)$$

$$C'_{max} = C_{max1} + C_{max2}T \quad (1.45)$$

where C is wt%, C_{max1} and C_{max2} are tabulated wt% constants, κ_{max1} and κ_{max2} are tabulated conductivity constants in mS/cm, and x and y are tabulated constants. Some strategies for reducing ohmic losses include:

1. Increasing the temperature to improve conductivity.
2. Using supporting electrolytes to improve the conductivity of the solution.

The presence of inert voids also has an effect on the conductivity of solutions. These voids may include gas bubbles and dispersed solids. The conductivity of the solution can be estimated using either the Maxwell equation for void fraction, $\varepsilon < 0.6$,

$$\kappa/\kappa_o = 1 - \varepsilon/1 + \frac{\varepsilon}{2} \quad (1.46)$$

or from the Meredith-Tobias equation for void fraction, $\varepsilon > 0.6$,

$$\kappa/\kappa_o = 8(1 - \varepsilon)(2 - \varepsilon)/(4 + \varepsilon)(4 - \varepsilon) \quad (1.47)$$

where κ_o is the specific conductivity and κ is the conductivity in the absence and presence of voids, respectively, in S/m.

1.8.3 Mass-transport Overpotential

Fuel cell reactions take place on the surface of the catalyst at the electrode. When current densities get sufficiently high the reactant is not able to diffuse to the catalyst surface fast enough to sustain the reactant consumption rate. Therefore, a concentration gradient between the bulk solution concentration, C_{bulk} , and the concentration at the electrode surface, C_{surface} , develops. This limits the current density that can be achieved by the fuel cell. The concentration overpotential, η_{conc} , can be expressed by the following relationships,

$$\eta_{\text{conc}} = \frac{RT}{nF} \sum_j \ln \left(1 - \frac{i}{i_{l,j}} \right) \quad (1.48)$$

$$i_{l,j} = \frac{nF}{s_j} k_{m,j} C_{\text{bulk},j} \quad (1.49)$$

where $i_{l,j}$ is the limiting current of species j in A/cm^2 , s_j is the stoichiometric coefficient of species j , $k_{m,j}$ is the mass transfer coefficient in cm/s and $C_{\text{bulk},j}$ is the bulk concentration of species j in mol/cm^3 .

1.9 Low Temperature Fuel Cells

1.9.1 The Polymer Electrolyte Membrane Fuel Cell

Polymer electrolyte membrane fuel cells (PEMFCs) are electrochemical energy conversion devices that operate with a hydrogen fuel and oxygen/air as the oxidant. A schematic along with the relevant half-cell reactions and overall cell reaction are shown in Figure 1.4. At the heart of a PEMFC is the membrane electrode assembly (MEA). The MEA consists of a polymer electrolyte membrane (PEM) sandwiched between the hydrogen oxidation anode and the oxygen reduction cathode. The anode contains some catalyst capable of promoting hydrogen dissociation to produce protons which are transported by the PEM to the cathode. The electrons liberated during this reaction are forced by the membrane and charge differential to travel in an external circuit to the cathode. At the cathode a catalyst is used to adsorb oxygen which then combines with the protons and electron that have been transported through the PEM and the external circuit, respectively, to produce water.

PEMFC technology, which was originally designed for use on space based missions, has received renewed interest with hopes of being utilized in a wide range of applications including grid-level stationary and back-up power and light-weight and heavy-duty transportation [9]. In addition to offering higher efficiencies compared to heat engines the technology offers advantages of being non-polluting [8]. With recent advances in the PEMFC it is on the verge of full commercialization but it has faced both performance and economic related challenges that have prevented it from tipping over into wide-spread use.

The oxygen reduction reaction (ORR) in the PEMFC is a kinetically slow process that is responsible for the major efficiency losses in a PEMFC even when precious metal

catalysts are used [10]. In addition, Pt nanoparticles can agglomerate and disengage due to the degradation of the catalyst supports in a PEMFC environment [11, 12]. This compromises the stability and durability of the catalysts which significantly reduces the lifetime of the PEMFC. Also the presence of a thin film triple phase boundary (TPB) leads to incomplete utilization of the catalyst layer and constrains electrode design [8]. Furthermore, the cost of Pt means that the total catalyst content in the MEA can account for more than 50% of the stack cost [9]. Recent advancements in PEMFC technology have successfully reduced the Pt-content from 2 mg/cm² to 0.4 mg/cm² without compromising fuel cell performance. However, during the same time Pt cost has increased five-fold ensuring even such low Pt-loadings do not make PEMFCs economically viable for higher power applications. For this reason it is required that Pt-content be around 0.1 mg/cm² so that the system cost sensitivity to Pt cost is negligible [13].

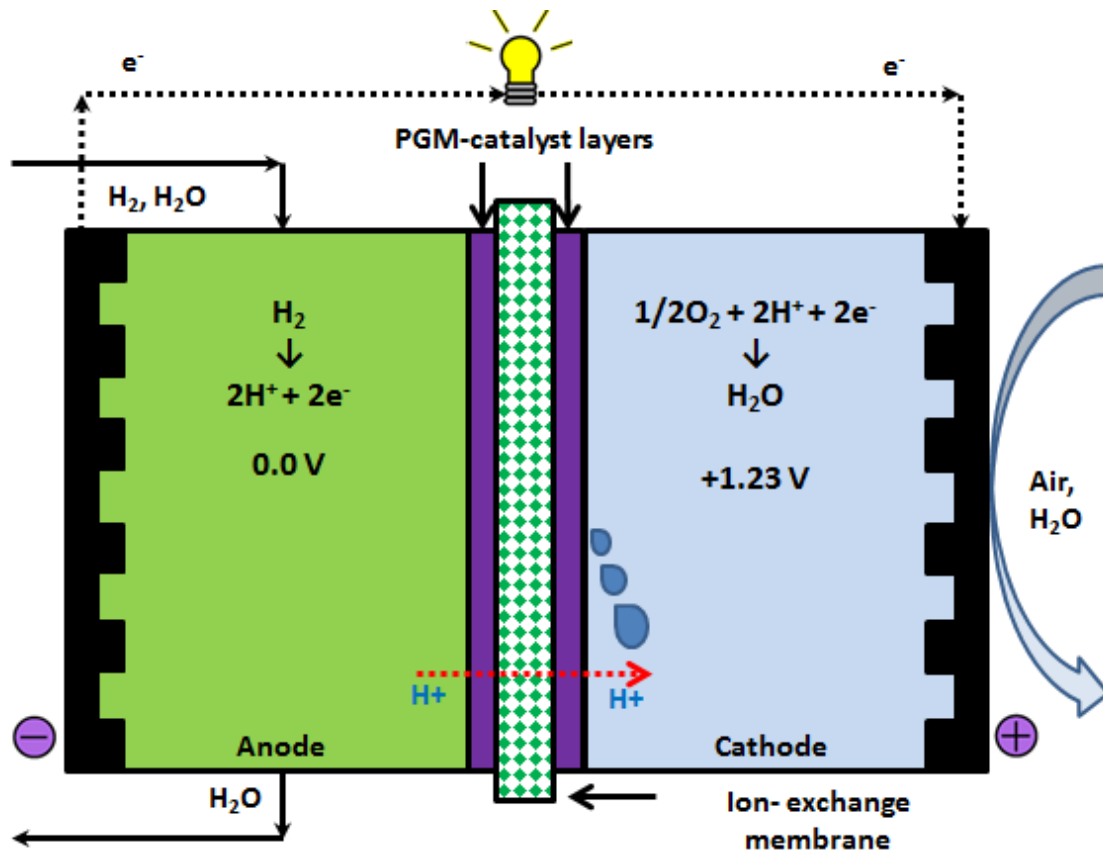


Figure 1.4: A schematic of the PEMFC along with the relevant electrochemical reaction.

In addition to the ORR the PEM itself also poses some challenges. Expensive Nafion® membranes are used as the PEM due to their good conductivity when fully hydrated [14]. However, water management during fuel cell operation of these membranes is challenging. On the one hand at low load operation the PEM may dehydrate and lose conductivity as not enough water is generated in the reaction. On the other hand during higher load operation when more water than that required to hydrate the PEM is generated at the cathode the condensing water can flood the cathode catalyst sites resulting in fuel cell failure. Ensuring proper hydration of these membranes requires the use of external balance-of-plant components for water management [8]. Here, the hydrogen and/or oxygen streams are externally humidified to provide water to the PEM. Meanwhile intricate electrode and flow field designs are used to ensure product water removal at higher load fuel cell operation [8, 15]. Furthermore, during fuel cell operation excessive amounts of heat are generated that cannot be removed by the gaseous fuel and oxidant [8, 16]. External cooling equipment is thus required for proper heat management of the system. These issues of Pt-catalyst cost and durability, membrane conductivity and reliability and additional balance of plant components for heat and water management conspire to make the PEMFC system less attractive for commercialization.

1.9.2 The Direct Methanol Fuel Cell

The direct methanol fuel cell (DMFC) is an electrochemical energy conversion device, which uses the polymer electrolyte membrane fuel cell (PEMFC) architecture but is simpler than a system using fuel processing equipment (e.g., reformer) due to the direct oxidation of an aqueous fuel. In addition DMFCs do not require additional balance-of-plant components for heat and water management as the aqueous methanol fuel can successfully provide both to the system.

The DMFC operates by oxidation of methanol at the anode and oxygen reduction at the cathode. A schematic of the DMFC with the relevant electrochemical reactions and the overall reaction are shown in Figure 1.5.

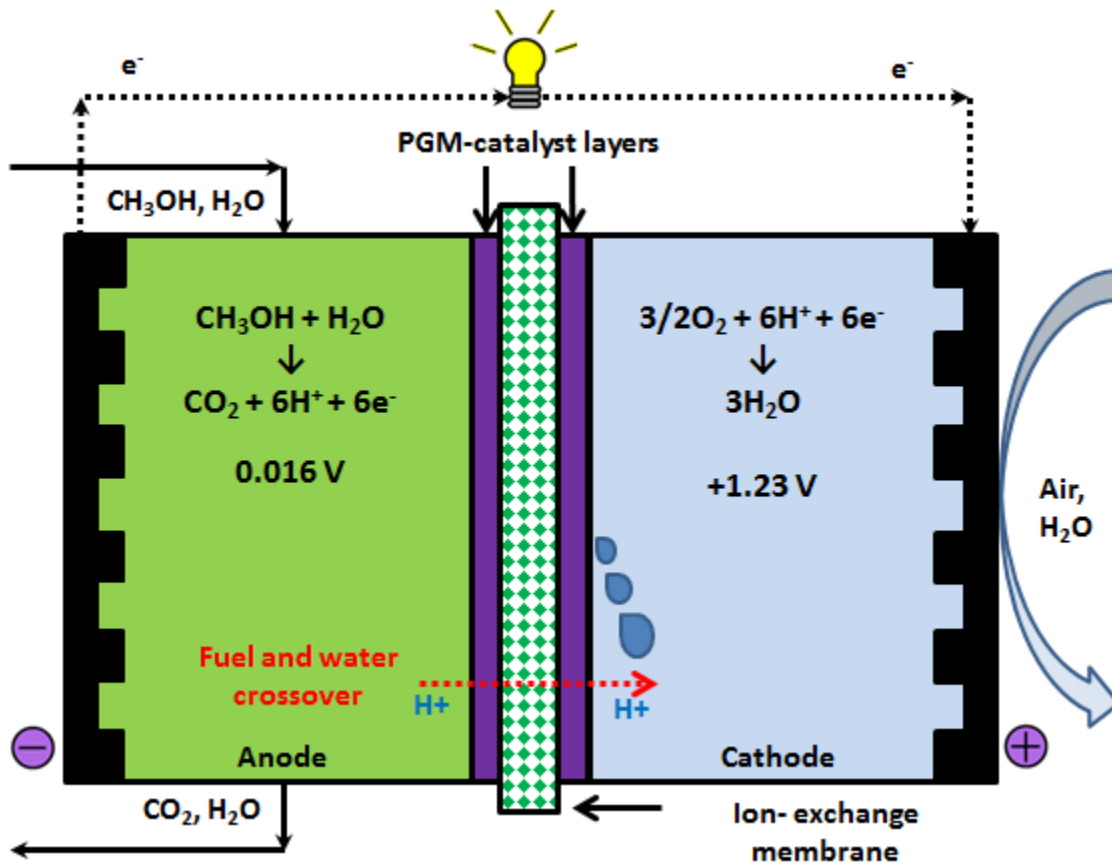


Figure 1.5: Schematic of a DMFC with the relevant electrochemical reactions.

DMFCs offer several advantages over other fuel cells for micro or portable applications but have been targeted for other needs as well [17-19]. Direct methanol oxidation in this system removes the need for a reformer that may be required for additional fuel processing in a PEMFC making the system lighter and more portable [20]. Methanol is usually supplied in an aqueous solution creating an aqueous environment for the electrochemical reactions to occur in. This can further simplify the system by removing the need for an auxiliary humidifier that is required to prevent membrane dehydration. Furthermore, methanol also provides a high volumetric energy/charge density (4.62 kWh/L/3.95 kAh/L at 25°C) [21] making it a more suitable fuel for micro or portable applications where energy and power density are more important than efficiency. However, due to poor kinetics of the reactions at both the anode [21, 22] and the cathode [23, 24] precious group metal (PGM) catalysts (e.g., Pt) have to be employed at both electrodes, significantly increasing the cost of the system.

Currently Nafion® membranes are used in DMFCs due to their good proton conductivity, mechanical durability and chemical resistance. However, these are known to be permeable to liquid fuels resulting in fuel crossover leading to significant losses in performance [25]. Fuel crossover can lead to cathode depolarization by either fuel oxidation at the cathode creating a mixed potential due to the presence of Pt catalyst or by the consumption of oxygen from the direct methanol oxidation resulting in a Nernstian potential loss and increased kinetic overpotentials [26].

As crossover and methanol concentration are closely related, the above mentioned limitation with fuel crossover limits the fuel to low concentrations of methanol (1-3 M) at the anode thus limiting the maximum attainable current. Protons generated during methanol

oxidation permeate to the cathode but each proton will usually drag a number of water molecules due to the presence of excess water in the fuel by the electro-osmotic drag exacerbating cathode flooding [27]. Several approaches can be taken to address methanol crossover, including development of new membranes [28], modification of membranes [29], introduction of fuel additives [30], optimization of operating conditions [31], design of novel electrodes [32] and the employment of methanol-tolerant cathode catalysts [33]. Further problems associated with two-phase flow at the anode and the presence of the triple phase boundary constraint at the cathode becomes a hindrance regarding the design of the system.

1.9.3 The Membrane Electrode Assembly

At the heart of both the DMFC and PEMFC is the membrane electrode assembly (MEA). It consists of the polymer electrolyte membrane (PEM) sandwiched by the fuel oxidation anode and the air reduction cathode which may be either compressed or hot-pressed together. The electrodes are usually made from Teflon® coated carbon cloth, paper or felt gas diffusion layers (GDL) with a catalyst layer applied to the side closest to the membrane. The catalyst is applied by creating an ink composed of noble metal particles (e.g., Pt, Ru, Au, etc.) either unsupported or supported on carbon and an ionomer binder (e.g., Nafion®) dissolved in some solvent. This catalyst ink is then sprayed, painted or printed on to the GDL. It is also common to find the anode and cathode catalysts applied directly to opposite sides of the membrane to form a catalyst coated membrane (CCM). Here, the catalyst ink is deposited onto two Teflon® sheets sandwiching a membrane which is then hot-pressed to transfer the catalyst onto the membrane. These two methods apply a thin film catalyst layer to reduce ohmic losses and ensure ionic contact between the PEM and catalyst sites [8].

1.9.4 The Electrodes

Electrodes for the fuel cell are essentially the catalyst sites where the electrochemical reactions take place. However, other components are required to ensure proper operation of the electrodes. Usually the electrodes are applied onto a GDL or electrode backing layer on the GDL which serves several important functions in both the PEMFC and DMFC. The GDL must:

- Provide access for the reactants from the flow channels to the catalyst layer
- Provide access for products to be removed from the catalyst layer
- Provide an electrical connection between the catalyst sites and bipolar plates so electrons may be able to travel in an external circuit to do work
- Act as a heat conductor to conduct heat generated in the reaction to the bipolar plates where it is removed by the coolant. The bipolar plates usually have two separate sets of channels on either side; the side closest to the GDL has reactants flowing while the coolant flows in separate flow channels on the outside of the bipolar plates.
- Provide mechanical support to the MEA so it does not sag into the flow channels

The following properties are therefore required in a GDL to serve these functions:

- The GDL must be porous to ensure reactant access as well as product removal. Furthermore, pore size is important as the catalyst nano-particles must be supported by the GDL. Often a micro-porous layer (MPL) or an electrode backing layer is applied to the GDL to aid product water removal.
- The GDL must have good electrical and thermal conductivity.
- The GDL should also be rigid enough to support the MEA but with sufficient flexibility to ensure good electrical contact with the bipolar plates.

Due to these requirements for the GDL carbon fiber based materials are best suited for use as the GDL. The catalyst required for the respective reaction is usually applied to the GDL by means of creating a catalyst ink of the required composition. The catalyst ink consists of the catalyst particles in a solution of water, some solvent (e.g., iso-propanol) and some binding agent (e.g., Nafion® ionomer). The catalyst ink is then applied to the GDL by painting, spraying, printing or scraping. The MPL may be added to the GDL in a similar manner. This catalyst layer, the MPL (if present) and GDL together comprise the electrode. The air reduction cathode is common to both the PEMFC and DMFC while the reactions at the anode are hydrogen oxidation and methanol oxidation, respectively. Each of these electrodes has its own challenges with regards to electrode design. When the MEA consists of a CCM the GDL does not need to be bound to the catalyst layer but must be compressed together and in contact with the catalyst layer.

1.9.4.1 The Oxygen Reduction Cathode

The most commonly used catalyst for the oxygen reduction reaction (ORR) is carbon supported Pt or Pt black without a support. The type of Pt catalyst used is an important factor. Usually 10-40 by wt% Pt supported on C is best suited for the ORR [34]. Catalyst loadings of the Pt in the catalyst layer should be around 0.2-0.4 mg/cm² to ensure good fuel cell performance. Though the amount of catalyst used can be increased further it is unnecessary as it is only the active catalyst surface area that is important. Increasing the mass of catalyst does not necessarily increase the active surface area. Electrochemical reduction of oxygen requires three types of species to be present; oxygen gas, protons and electrons. As such the reaction can only occur when all three of these species meet at a common catalyst site. Therefore, this active catalyst site necessarily has to be connected electrically to an

external circuit and ionically to the ionomer or electrolyte that transports the protons to the cathode. Furthermore, this catalyst site must be adjacent to a pore that allows oxygen transport to it. This intersecting point is known as a triple phase site (TPS) [35]. Usually, the number of TPS is limited by the ionic connection between the membrane and the catalyst. This leads to most of the TPS existing only in a thin film adjacent to the membrane and catalyst not immediately next to the membrane is not utilized. Hot-pressing the cathode to the membrane and/or adding ionomer to the catalyst layer are approaches that can be used to improve the utilization of the catalyst layer. During hot-pressing the cathode is compressed with the catalyst layer facing the membrane at 135°C [36]. At this temperature Nafion ionomer which was added to the catalyst ink when it was applied to the GDL becomes fluid-like and bonds to the Nafion membrane. This provides improved proton conductivity by creating an ionomer extension away from the membrane into the catalyst layer. Usually an ionomer composition of 20-30% in the catalyst ink is best for this purpose.

The GDL that is used for the air cathode is extremely important. This layer must serve two equally important purposes; allow gas diffusion to the catalyst sites and aid in product water removal from the catalyst sites. Without proper access for oxygen to the catalyst sites the cathode will become mass transport limited leading to fuel cell performance failure. Similarly, water management at the cathode is required to ensure product water from the reactions does not build up and flood the catalyst sites depriving them of oxygen. A common approach is to give the GDL a hydrophobic nature by applying a Teflon coating to improve the removal of water. This forces the water into the membrane which has the added benefit of hydrating the membrane ensuring losses in membrane conductivity are not encountered. In addition Teflon containing micro-porous carbon sublayer may be added

between the catalyst layer and the GDL to increase the hydraulic pressure and force water towards the membrane [37]. When a methanol fuel is used forcing water to the anode is even more important as methanol oxidation consumes water as a reactant. Furthermore, water removal from the cathode in DMFCs is exacerbated by water from the anode being dragged to the cathode by protons due to electro-osmotic forces [38]. Alternatively, innovative flow channel designs may be used to ensure oxygen reaches the catalyst sites and water is removed from the catalyst sites.

1.9.4.2 The Hydrogen Oxidation Anode

The hydrogen oxidation reaction (HOR) also requires the use of PGM catalysts though the amount of catalyst required compared to the ORR is significantly lower. The catalyst used for the HOR is most commonly carbon supported Pt (e.g., 20 wt% Pt on C) or unsupported Pt black which may be applied to the GDL or to the membrane. Similar to the ORR the HOR is also subject to the TPS requirement as catalyst in contact with hydrogen must be connected to an electron transport mechanism and a proton transport mechanism. As with the air cathode it is advisable to have an extension of the ionomer into the catalyst layer to increase the number of TPS available and active catalyst surface area. The GDL used for the hydrogen anode though is not subject to as stringent demands as the air cathode for product water removal as no water is formed at the anode. However, it is important to humidify the hydrogen fuel stream and allow some water to reach the catalyst layer as ionomer in the catalyst layer and the membrane must be sufficiently hydrated.

1.9.4.3 Methanol Oxidation Anode

Similar to the HOR and ORR, methanol oxidation also requires PGM catalyst. Though Pt may be used for this purpose its electrochemical activity degrades over time. The reaction mechanism for methanol oxidation proceeds through the formation of carbon monoxide [39] which strongly adsorbs onto the surface of Pt reducing the number of active catalyst sites [40] i.e., carbon monoxide poisoning. Carbon monoxide may be removed from the Pt surface by reaction with chemisorbed OH to form CO₂ and H⁺ [41]. Therefore, catalysts used for the methanol oxidation anode normally use a Pt metal alloy that promotes OH chemisorption, such as Ru [42]. The Pt/Ru alloy catalyst is applied to the GDL in a similar manner to the ORR and HOR using a Nafion or Teflon ionomer.

An important function of the anode design is the removal of CO₂ from the catalyst layer and gas diffusion layer. This may be achieved by adjusting the hydrophobicity of the GDL with the use of Nafion® ionomer or PTFE [36]. Although this is a viable approach, a careful balance must be achieved as methanol and reactant water transport to the catalyst sites is favoured by a hydrophilic anode.

1.9.5 The Membrane

Fuel cell membranes need to exhibit high proton conductivity, prevent reactant mixing and be highly durable and chemically stable with the reactions. The most commonly used membrane in PEMFCs and DMFCs is the Nafion membrane. Nafion is a copolymer of polytetrafluoroethylene (PTFE) and a perfluorosulfonate monomer. The Nafion membrane is discussed in more detail later. Different thicknesses of Nafion 1100 equivalent weight (E.W) membranes are commonly used in fuel cells. Most commonly Nafion 112 (thickness 2 mils) and Nafion 117 (thickness 7 mils) are used in the PEMFC and DMFC, respectively.

1.10 Redox Flow Batteries

Redox flow cells or redox flow batteries (RFCs/RFBs) are relatively new electrochemical energy storage devices capable of providing grid-level power quickly and efficiently to consumers. They are similar to both fuel cells and batteries in their operation but differ in key aspects. Conventional batteries store energy within the electrode structure whereas fuel cells store the energy in gaseous or liquid fuels and oxidants that are stored externally to the cell. Flow cells are similar to conventional batteries in that they have a fixed charge and cannot operate continuously without recharge but unlike batteries and similar to fuel cells they store energy in recirculating electrolytes external to the electrode. This allows RFBs to have their energy storage and power generation capabilities independent of each other unlike conventional batteries [43]. The power is determined by the size of the stack (number of cells and active electrode area) while the energy storage capacity is a function of the volume and concentration of the electrolyte. This gives the consumer added flexibility as energy storage can easily be increased by adding more electrolytes while the power can be increased by changing the size of the stack.

Currently flooded lead-acid or valve regulated lead-acid batteries are most commonly used for large scale energy storage. These batteries have a long life-span and can operate in extreme conditions. However, their maintenance cost and heavy weight make them undesirable. Redox flow cells offer advantages over incumbent lead-acid batteries with regards to modular design, transportability and flexible operation. Modular design allows RFBs to have a lower cost, flexibility of design and ease of customization with regards to power demand by simply adding or removing modules. In addition, the modules can be serviced individually without complete power shutdown. RFBs also have advantages with

regards to charge/discharge cycles as they can be discharged completely unlike lead-acid batteries without damaging the cells.

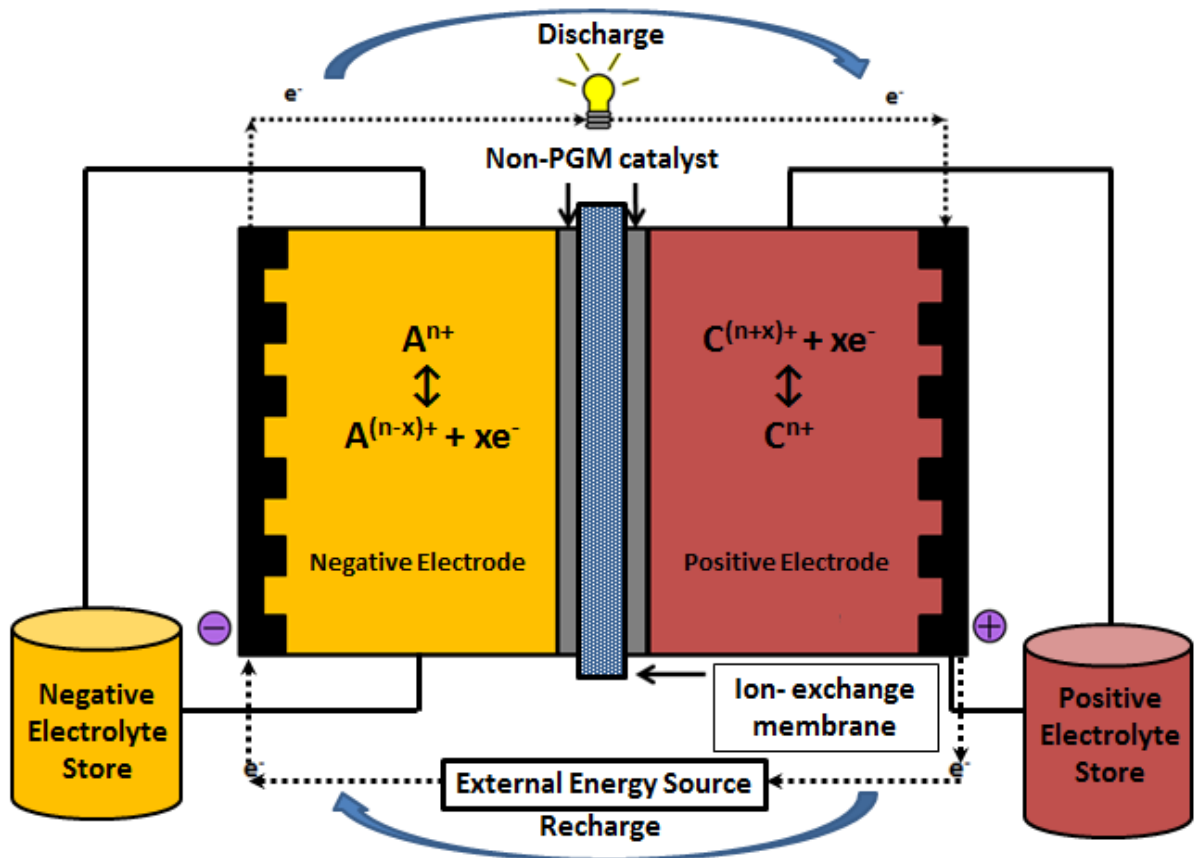


Figure 1.6: Schematic and operation of a generic redox flow battery.

RFBs use two dissolved electro-active redox species electrolytes that undergo oxidation or reduction to store or deliver energy. The redox electrolytes are stored externally in tanks and recirculated to a flow cell where the reactions take place. Figure 1.6 shows a general schematic of a redox flow cell. The flow cell itself has architecture similar to that of a PEMFC where an ion-exchange membrane is sandwiched by bipolar electrodes. The electrode themselves are capable of promoting both the oxidation and reduction reactions depending on whether the cell is under discharge or being charged by an external power

source (e.g., hydro-power, solar, etc.) and are connected to their respective electrolyte reservoir. Similar to fuel cells the flow battery can be scaled up to provide the required electrical power by increasing the area of the electrodes, adding more electrodes to the stack and/or connecting the electrodes in parallel or series.

In addition to design benefits RFBs offer several other benefits over other battery storage technologies. First, the electrode reactions are usually very simple reversible reactions often involving a single electron transfer and ion exchange. Secondly, most redox electrolytes that are chosen have high exchange current densities on non-PGM based catalysts meaning significant material cost savings. In addition, very good kinetics of these redox electrolytes allow for low temperature operation. The redox electrolyte has high shelf life and cycle life and unlike lead-acid or other electrochemical battery storage technologies they do not suffer from self-discharge over time. Moreover, the advantage of no self-discharge for RFBs allows them to achieve close to theoretical energy efficiencies which are not possible with other batteries.

1.10.1 Electrolyte Requirements for Use in the Redox Flow Battery

The anode and cathode redox couples for a RFB must satisfy certain criteria [44]:

- As the electrolytes are charged and discharged the electrolytes go through both oxidation and reduction. The electrolytes must exhibit good electrochemical activity during both the oxidation and reduction reactions.
- The redox couples used must have a high solubility in both the oxidized and reduced states to prevent precipitation during charge/discharge cycles.
- The redox couples must be electrochemically stable with the solvent, membranes and electrodes.
- The anode and cathode redox couples must be sufficiently far apart in terms of standard potentials in order to allow a useful voltage to be drawn from them

In addition it is advisable to avoid systems that may use complexing agents which increase system complexity. Furthermore, redox reactions that do not undergo a large pH change during reactions are favored as they are likely to be more stable and durable. Only a small number of redox couples exist that satisfy these requirements and are suitable for use in a RFB. Table 1.3 lists some of the more common redox couples that may be used in a RFB.

Another important consideration when choosing redox couples is hydrogen or oxygen evolution during the charge (regeneration) cycle. This may be avoided by choosing anode redox species with a potential close to or greater than the standard hydrogen potential (i.e., > 0.00 V vs. SHE) and cathode redox species with a potential close to or less than the oxygen reduction potential (i.e., < 1.23 V vs. SHE). The choosing of redox couples is a complex task

and several levels of testing should be performed to ensure suitability of use. A good example of a platform to follow for choosing an appropriate redox couple can be found by Giner et. al in the literature [45].

Table 1.3: Suggestions for redox couples that may be used in a RFB system.

Redox Couple	Half-cell Potential	Electrolyte	Suitable as
$\text{Ce}^{3+}/\text{Ce}^{4+}$	1.44	0.5 M H_2SO_4	Oxidant
$\text{Br}^-/\text{Br}_3^-$	1.05	0.5 M H_2SO_4	Oxidant
$\text{VO}^{2+}/\text{VO}_2^+$	1.00	0.5 M H_2SO_4	Oxidant
$\text{Fe}^{2+}/\text{Fe}^{3+}$	0.67	0.5 M H_2SO_4	Oxidant
$\text{Sn}^{3+}/\text{Sn}^{4+}$	0.15	0.5 M H_2SO_4	Fuel
$\text{V}^{2+}/\text{V}^{3+}$	-0.26	0.5 M H_2SO_4	Fuel
$\text{Ti}^{3+}/\text{Ti}^{4+}$	-0.37	0.5 M H_2SO_4	Fuel
$\text{Cr}^{2+}/\text{Cr}^{3+}$	-0.42	0.5 M H_2SO_4	Fuel

1.10.2 Redox Flow Battery Electrodes

The properties that are desired for the electrodes of a RFB are similar to that of a fuel cell. Though the material required for the electrodes depends on the desired reactions and the redox couples the following properties are desired:

- Highly selective towards the desired reactions
- High surface area with good electrochemical activity
- Highly electrically conductive
- Preferably non-PGM catalyst
- Chemically stable with the system being developed

1.10.3 Redox Flow Battery Membrane

The membranes in a RFB serve the same purposes as in a fuel cell; providing ionic conductivity and electrical insulation while preventing reactant intermixing. Cation exchange membranes (CEM) or anion exchange membranes (AEM) may be used in RFBs. The choice of a CEM or AEM depends on the choice of charge carrier that travels between the electrodes to provide electroneutrality. Though CEMs allow for the use of highly mobile protons to be employed as the charge carrier they are not selective to protons [46, 47]. This can lead to crossover of the metal redox cation species to the opposite electrode. The use of AEMs significantly reduces metal redox cation crossover as the membrane is selective to anions. However, less mobile ions than the proton must now be used to carry charge (e.g., Cl^- , SO_4^{2-}) [48, 49]. Membrane contamination by the redox electrolyte is most likely to occur when the membrane has the same polarity as the redox couple. One example of this is when a cation exchange membrane (e.g., Nafion® PEM) is used with the $\text{Fe}^{2+}/\text{Fe}^{3+}$ to conduct protons in an iron chromium RFB. Here, sulfonic sites (SO_3^-) are ideally reserved for proton conduction. However, these sites are not selective and can become contaminated by either of the Fe^{2+} or Fe^{3+} ions which can significantly affect their proton conductivity. This can lead to lowered conductivity of the membrane leading to an increase in ohmic losses. For this reason the choice of a membrane and its maintenance during operation is an important consideration with regards to RFB design.

1.10.4 The Iron Chromium Redox Flow Battery

Several RFBs have been developed though few have been successful commercially. These include the all vanadium redox battery (VRB) [50], the vanadium bromine battery (VBB) [51, 52] and the zinc bromine flow cell [53] amongst others. However, in 1974 the first successful redox flow battery was developed in the form of the iron chromium redox flow battery [44]. Figure 1.7 shows a schematic of the Fe/Cr RFB with the relevant electrochemical reactions and standard reduction potentials. This system has been investigated by a number of research groups including those at NASA [54] and the University of Alicante in Spain [55, 56].

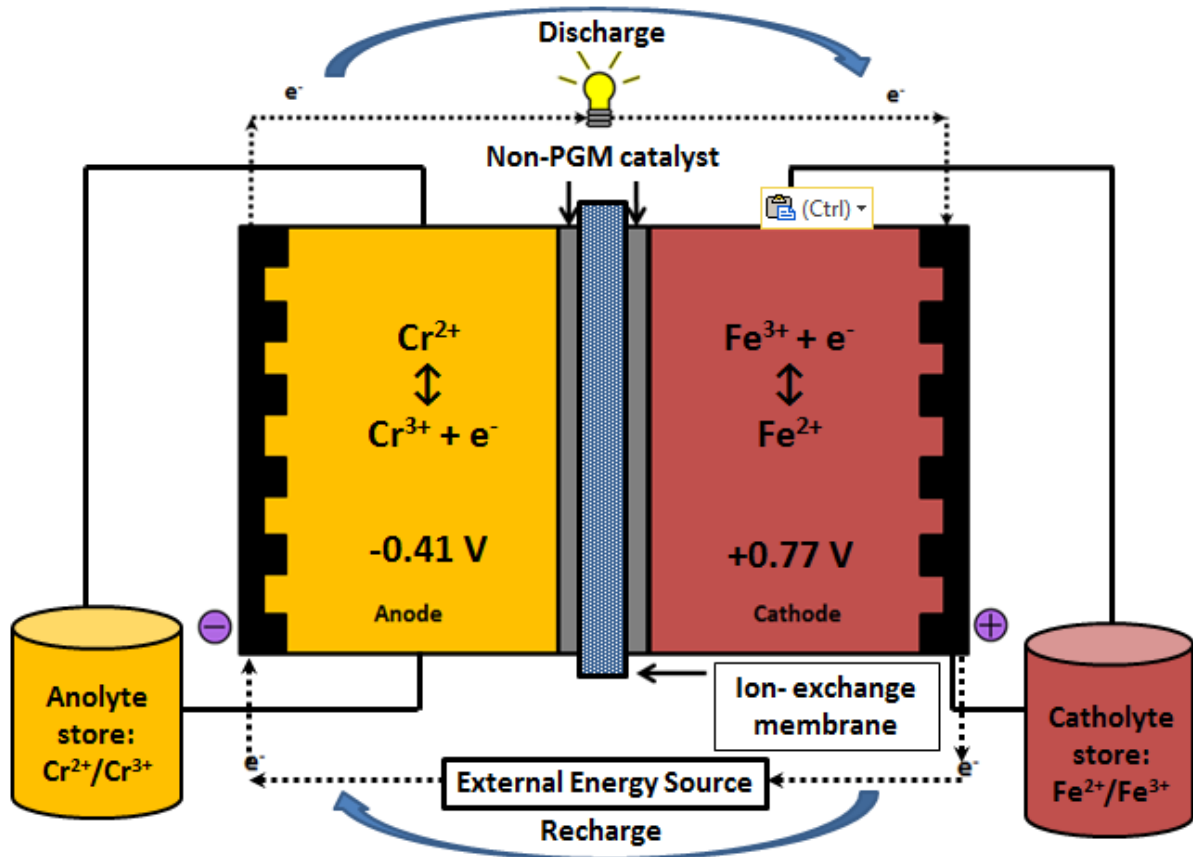
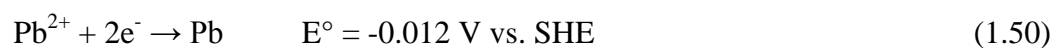


Figure 1.7: Schematic and relevant electrochemical reactions in a Fe/Cr Redox Flow Battery.

Both the reactants exist in a hydrochloric acid solution with usually chromium chloride salt and iron chloride salt used for the anolyte and catholyte, respectively. This system has been studied both with a proton charge carrier where a CEM is used and a chloride ion where an AEM is used. The membrane is required to reduce crossover of the chromium or iron ions during charge or discharge. For the iron electrolyte carbon fiber based materials without PGM catalyst can be used due to the good electrochemical activity of the $\text{Fe}^{3+}/\text{Fe}^{2+}$ redox couple on carbon. The $\text{Cr}^{3+}/\text{Cr}^{2+}$ redox couple demonstrates relatively poorer electrochemical activity on carbon. Therefore the carbon electrode used for the chromium electrolyte has gold or lead deposited on it [43].

The use of the $\text{Cr}^{3+}/\text{Cr}^{2+}$ redox couple has certain issues associated with it as well. The standard half-cell potential of $\text{Cr}^{3+}/\text{Cr}^{2+}$ (-0.41 V vs SHE) is lower than the standard half-cell potential of hydrogen (0.00 V vs SHE). Due to the presence of gold on the electrode hydrogen evolution can occur even at relatively low kinetic overpotentials. This secondary reaction competition leads to lowered energy efficiency of the system by reducing the current efficiency. Furthermore, this secondary reaction leads to the state of charge (SOC) of the chromium electrolyte changing during the charge and discharge cycles which limits the electrical energy storage capabilities of this RFB.

A novel approach for reducing the effects of the undesired hydrogen generation reaction involves the addition of PbCl_2 to the chromium electrolyte. During the charge cycle, where the Cr electrode is negatively shifted, the lead added to the electrolyte is deposited onto the carbon electrode in the form of the following reaction:



This deposition of Pb essentially covers the gold sites which would promote the hydrogen evolution reaction [45]. As high kinetic overpotentials are required to generate hydrogen on lead but relatively lower kinetic overpotentials are required for Cr reduction on Pb this approach significantly reduces the amount of hydrogen generated without significantly affecting the charge cycle. On the other hand during the discharge cycle the Cr electrode becomes positive leading to Pb oxidation back to the Pb^{2+} state and dissolution into the electrolyte. This stripping of Pb from the electrode surface exposes the gold sites allowing for the Cr oxidation reaction to proceed with lower overpotentials.

Although this preventative approach significantly reduces competition of the two reactions, some hydrogen is still generated. As such consecutive charge/discharge cycles over time reduce the SOC of the Cr electrolyte. The mismatch of SOC between the anolyte and catholyte effectively limits the energy storage capacity of the flow battery which becomes limited by the lower SOC electrolyte. This requires rebalancing of the cell to restore the RFB to its original state. An approach for this is to use a rebalancing cell where the hydrogen generated in the secondary reaction is used to reduce the ferric ion concentration in an external cell (electrochemical reactions shown in equations (1.51)-(1.53)) to a level where the SOC of the Fe electrolyte matches that of the Cr electrolyte. This approach essentially lowers the SOC of the Fe electrolyte to match that of the Cr electrolyte.



This approach relies on complete capture of the hydrogen during the charge cycle but this is not always possible and some hydrogen from an external source may be required. Success of this approach for a RFB system ultimately depends on the control algorithms for continuous monitoring of the SOC and ensuring proper RFB operation.

Another issue with the Fe/Cr RFB is related to power output and the SOC of the electrolytes. As the electrolytes become discharged their SOC is lowered. This results in RFB stack voltage losses leading to losses in power output. This issue is solved with the use of ‘trim cells’ in a RFB stack which are extra cells that are only utilized to compensate for voltage drops associated with electrolyte concentration. Initially, when the SOC is nearly 100% the trim cells remain unused. However, as the SOC drops these trim cells are allowed to have reactant flow through them which allows for the total power output of the RFB to be maintained.

The Fe/Cr RFB allowed for several advances to be made in flow battery technologies with the invention of the rebalancing cells and trim cells. These advances have allowed the Fe/Cr RFB as well as other RFBs to be utilized commercially. More information on RFBs may be found in the literature [57, 58].

1.11 The Hybrid Redox Fuel Cell

As discussed earlier in the PEMFC and DMFC sections, the ORR is responsible for a large portion of the losses in these fuel cells. An approach to address some of the issues associated with the ORR in both the PEMFC and DMFC is to replace the air cathode containing Pt with a metal-ion redox couple over a carbon cathode containing no PGM catalyst. This system is a hybrid of the redox flow battery and the PEMFC/DMFC and is referred to as the direct fuel redox fuel cell (DFRFC).

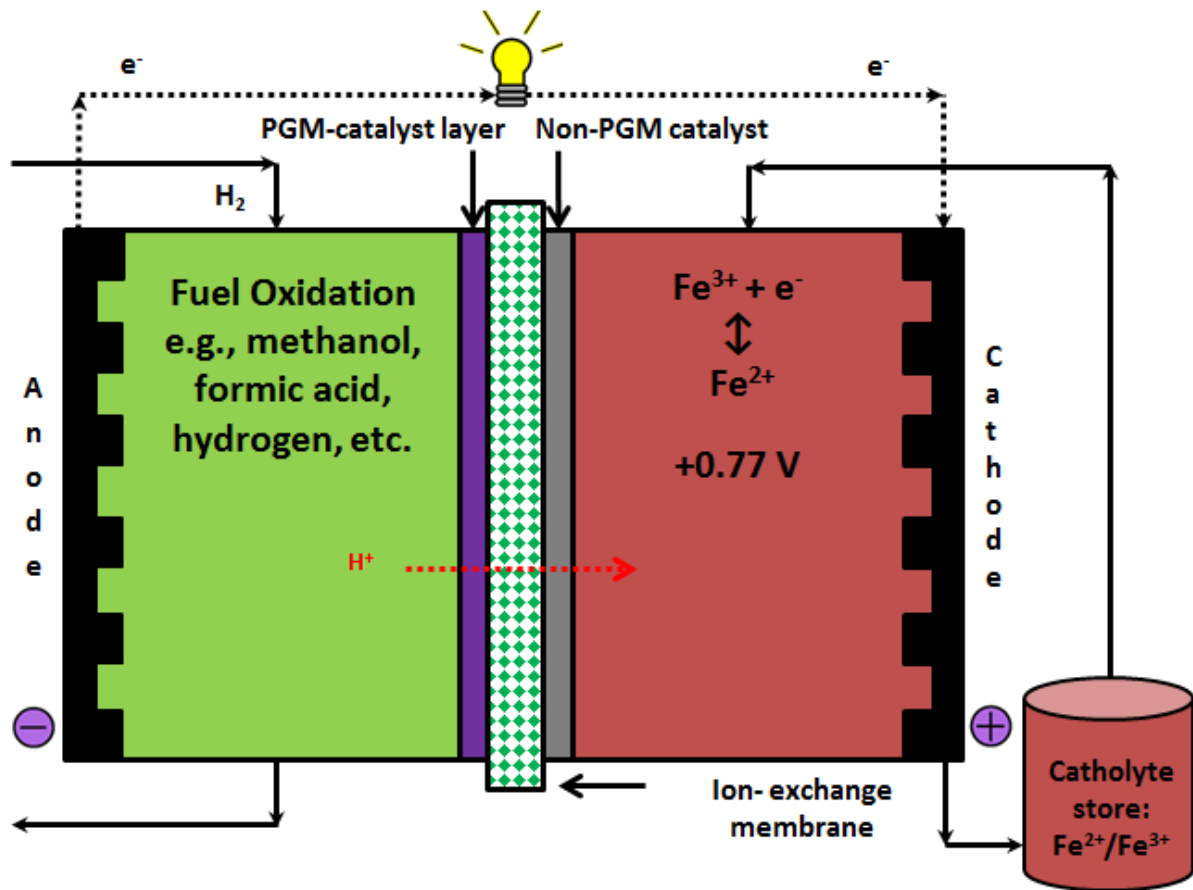


Figure 1.8. A schematic of the DFRFC using the $\text{Fe}^{3+}/\text{Fe}^{2+}$ redox couple and methanol fuel with the relevant electrochemical reactions.

The DFRFC operates in much the same way as a conventional fuel cell except that instead of the Pt containing air cathode, a carbon (non-PGM) cathode with a metal ion redox species is now employed. Several metal-ion redox couples have been proposed including Fe(III)/Fe(II), Cr(III)/Cr(II), Br₂/Br⁻, Vn(V)/Vn(IV) and Ce(IV)/Ce(III) amongst others. The redox couple must meet several criteria for this purpose including reasonable solubility in the electrolyte, good electrochemical activity and a sufficiently high redox potential to provide a useful cell voltage [44].

The system studied in this thesis work uses a Fe(III)/Fe(II) redox couple which was successfully demonstrated in a hydrogen redox fuel cell by Fatih, Wilkinson et al. [59, 60]. This system was later investigated and developed further with a methanol fuel by Ilicic, Wilkinson et al. using FeNH₄(SO₄)₂ as the precursor salt [61].

This DFRFC operates with fuel oxidation (e.g., methanol, hydrogen, formic acid, etc.) at the anode and ferric reduction at the cathode. A schematic of the DFRFC using methanol fuel with the relevant electrochemical reactions and the overall cell reaction is shown in Figure 1.8.

The DFRFC addresses several of the issues associated with the air cathode. Due to the ferric ion having an exchange current density on carbon ($\sim 10^{-2}$ A/cm²) [62] several orders of magnitude higher than that of oxygen ($\sim 10^{-10}$ A/cm²) on Pt [63], kinetic overpotentials associated with the ferric reduction reaction become very low. This allows for the elimination of all PGM catalyst at the cathode and a carbon cathode can be used just as effectively [59]. With regards to the DMFC this has the added advantage that methanol is not active on carbon which means that high fuel concentrations (up to 24 M methanol) can be utilized without any issues regarding cathode depolarization due to both methanol oxidation

at the cathode or due to direct oxidation of methanol as no oxygen is now present at the cathode [61]. Furthermore, the inherent nature of this system being an all-liquid process allows enhanced design flexibility at the cathode due to the absence of the triple phase boundary constraint. For the PEMFC this means a 3-D cathode may now be employed and for the DMFC both a 3-D anode and a 3-D cathode may be used for the DMFC. With regards to the PEMFC the use of a liquid redox catholyte has other advantages associated with heat and water management requirements in PEMFC systems. The iron liquid catholyte is usually sufficient to remove heat generated in the system. In addition, a non-humidified hydrogen fuel may be utilized as the PEM used in a DFRFC can be sufficiently hydrated by the water present in the iron catholyte [59, 60].

However, the DFRFC has some challenges including redox couple regeneration, mismatched charge density of the anolyte and catholyte, membrane contamination by the redox couple and crossover of the redox couple. Regeneration of the redox couple oxidant can be achieved by chemical [64], electrochemical [65] or biological [66] means which can potentially affect both the system's efficiency and simplicity. More recently, a novel in-situ power generating regeneration process was developed by Ilicic, Wilkinson et. al where the fuel anode is switched to become the air cathode during regeneration [67].

When methanol fuel is used as the anolyte the catholyte volumetric charge densities dictate the volume required for a desired energy output as each methanol molecule has six times the number of electrons as a ferric ion. Initial work by Ilicic, Wilkinson et al. [61] with the DMRFC used a catholyte ($\text{FeNH}_4(\text{SO}_4)_2$) with a concentration of Fe^{3+} around 1 M leading to mismatched charge densities resulting in incomplete utilization of methanol and reduced power densities. However, significant improvements in the catholyte charge density

have been made after using $\text{Fe}(\text{ClO}_4)_3$ as the precursor salt where the concentration of Fe^{3+} achieved was around 2.5 M [68]. The increased solubility of the ferric ions resulted in an improvement in the peak power density and maximum current density achieved in fuel cell tests when compared to the 1 M $\text{FeNH}_4(\text{SO}_4)_2$ catholyte.

When a metal redox ion is used that has the same polarity as the PEM contamination of the membrane as with RFB invariably occurs. The mechanism for this is discussed in more detail later. This contamination by metal redox ions leads to losses in fuel cell performance by decreasing the conductivity of the membrane. Moreover, most PEMs are permeable to liquid electrolytes leading to crossover related issues. Therefore, the issue of redox electrolyte crossover through the PEM can possibly lead to anode depolarization and losses in system efficiency.

2 Thesis Research Context

This research project is part of a larger research portfolio aimed at solving some of the major challenges that have prevented fuel cells from becoming widely deployed. These were discussed earlier and included the following:

- Issues with the air cathode with regards to poor kinetics, the use of PGM-catalysts at the cathode and cathode flooding due to the production of water
- Challenges associated with the use of polymer electrolyte membranes (e.g., Nafion) which include crossover of liquid fuels, membrane water management and membrane durability and reliability over fuel cell lifetime

With efforts aimed at solving these challenges the following research projects were undertaken by other researchers in the Wilkinson group:

- The development of an iron redox cathode for a PEMFC and a DMFC which resulted in the development of the direct fuel redox fuel cell (DFRFC) as discussed in the previous chapter – Franz Moraw, David Wilkinson et. al [59, 60], and Alan Ilicic, David Wilkinson et. al [61, 67]
- The development of a novel passive membraneless DMFC which eliminated the membrane in a passive system with promise for application in a number of different fully scalable active systems – Alfred Lam, David Wilkinson [69]

3 Objectives

The main goal of this thesis was to develop a membraneless electrode assembly for an active, scalable fuel cell based on a redox cathode, i.e., a DFRFC. The objectives were as follows:

1. Develop a membraneless electrode assembly design for an active fuel cell system based on the controlled reactant gradient concept developed for the passive DMFC for an active fuel cell system
2. Use the developed membraneless electrode assembly design to eliminate the membrane in the DFRFC to help address membrane issues (e.g., contamination, loss of proton conductivity, etc.) and to reduce cell cost
3. Demonstrate the flexibility of the membraneless design approach to different platforms, electrolytes, fuels and oxidants
4. Demonstrate a low cost hydrogen fuel cell based on a membraneless design with very low precious metal content

4 Background to Thesis Research Approach

At the heart of the operation of the fuel cell is the membrane electrode assembly. Here, an ion exchange membrane is sandwiched between the catalyst based anode and cathode. The ion-exchange membrane serves the following functions at the core of the fuel cell:

1. Providing ionic conductivity between the anode and cathode: the membrane must be able to conduct protons from the anode to the cathode
2. Preventing mixing of the reactants: the membrane must act as a convection and diffusion barrier between the fuel and oxidant to prevent efficiency losses related to reactant loss, direct reaction and/or mixed potentials
3. Providing electrical insulation between the anode and cathode: the membrane must not be electrically conductive and must prevent electrode contact so as to prevent short-circuiting and force the electrons into an external circuit where they may be harnessed for work

Since its discovery in the 1960s at DuPont®, Nafion® polymers have been the most commonly used for the creation of ion exchange membranes. Nafion® membranes are well suited for use in fuel cells due to their excellent proton conductivity (when fully hydrated), ability to absorb large amounts of water, good chemical resistance and mechanical strength. Nafion® is a synthetic polymer that exhibits ionic properties due to its unique composition. It is formed from a polytetrafluoroethylene (PTFE) backbone, as shown in Figure 4.1 that has been modified to allow for proton conduction. The PTFE chain is subjected to a sulphonation reaction where a sulfonic acid ending side chain is added to the polymer giving the structure of Nafion®, as shown in Figure 4.2.

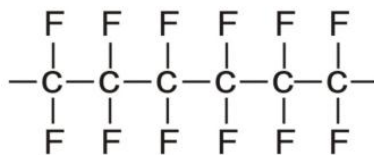


Figure 4.1: Polytetrafluoroethylene chain that forms the Nafion backbone.

Over the years, Nafion® has become a widely studied material due to its interesting properties. PTFE is a highly hydrophobic polymer while the sulfonic acid sites on the polymer are highly hydrophilic regions. This gives Nafion® a highly hydrophobic structure with hydrophilic pores that are able to conduct protons and transport water.

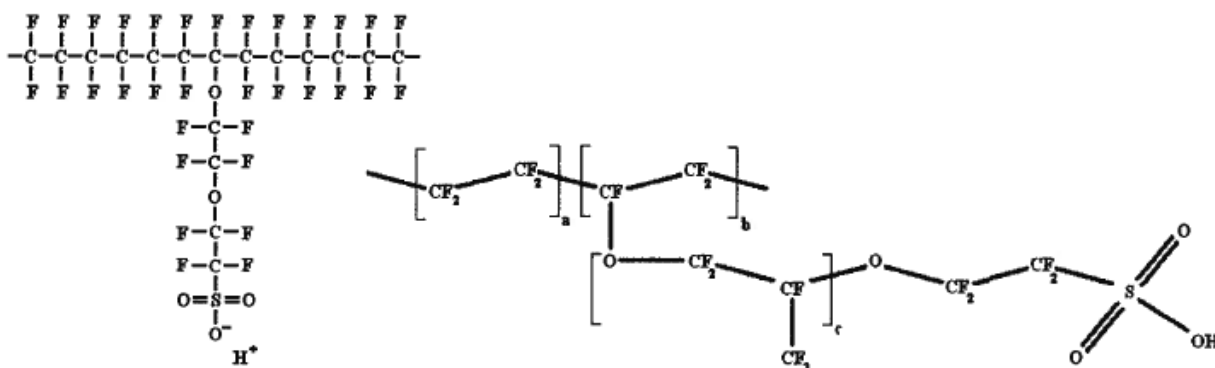


Figure 4.2: Structure of Nafion showing the sulfonated side chain that allows proton conduction to be possible.

Proton conduction through the hydrophilic pores in the Nafion® generally occurs by the Grotthus mechanism where the sulphonic acid groups attract the protons allowing for H^+ movement across the membrane. Protons produced by an electrochemical reaction in the fuel cell will hop across the sulphonic acid sites in the membrane while the electrons travel via an external circuit to ensure charge neutrality is maintained.

Although Nafion® membranes may be used in the Direct Fuel Redox Fuel Cell (DFRFC) where the oxygen cathode is replaced with a redox species cathode, exposure to the redox species cations can result in significant fuel cell performance losses. As discussed sulphonic sites present on the PTFE backbone in the membrane allow for proton conduction by allowing a counter charge that attracts the positive protons. However, this mechanism is not selective to protons but can allow conduction of other cations. When the Nafion® membrane is exposed to a positive redox cation species (e.g., Fe^{3+} , Fe^{2+}), these cations will occupy some of the sulphonic sites that would ideally be reserved for protons. This results in membrane contamination and loss in proton conductivity of up to 80% [59]. This significantly limits the performance of the fuel cell due to increased ohmic overpotentials. In our previous work this mechanism was shown to significantly lower fuel cell performance losses as evidenced by extremely linear polarization curves with high negative slopes [68]. In this thesis a major goal is to investigate a membraneless fuel cell configuration where the functions of the membrane are replicated by novel design considerations. This approach should significantly reduce the membrane-related issues and result in significant cost reduction.

Previous approaches to membraneless fuel cells have included laminar flow fuel cells and mixed reactant fuel cells. Laminar flow fuel cells operate by taking advantage of flow conditions and cell geometry while operating under laminar flow to prevent intermixing. Mixed reactant fuel cells on the other hand operate on the basis of highly selective anode and cathode catalysts.

Laminar flow fuel cells, also known as micro-fluidic fuel cells, operate by supplying the oxidant and fuel in a co-laminar flow configuration without a physical barrier to separate

the anode and cathode. Here, properties unique to micro-fluidic fluid-fluid interfaces are utilized to delay convectonal mixing of the fuel and oxidant. When two fluids with similar viscosity and density are brought together in a single channel a fluid-fluid interface develops. Species transport across this interface then takes place due to diffusion, convection, migration (electro-gradient) and chemical reaction. Micro-fluidic fuel cells flow both liquid fuel and oxidant lamarily as shown in Figure 4.3, usually at Reynolds numbers of less than 100, in a single channel between the anode and cathode. Ionic conductivity can be provided through species transport via the fluid-fluid interface while keeping the electrodes physically separate to ensure electrical insulation. However, as the oxidant and fuel streams flow further down the channel mixing of the electrolytes begins to occur which can result in fuel cell performance losses related to crossover effects. These effects may be mitigated by increasing the distance between the electrodes. But increasing the distance between the electrodes increases ionic resistance thus leading to increased ohmic losses in the fuel cell. Therefore, design management of the channel with respect to balancing ohmic losses and crossover inefficiencies is important in this fuel cell design. Kjeang et. al., in “Microfluidic fuel cell: A review” provide a good summary of micro-fluidic fuel cell technology [70].

Most laminar flow fuel cells have tended to use a Y-shaped channel to bring together the oxidant and fuel though many other flow configurations including F-shaped, T-shaped and radial porous electrode configurations have been demonstrated in literature. Laminar flow fuel cells offer several advantages over conventional PEM-based fuel cells in that they do not require water management and are not prone to efficiency losses related to crossover. Their biggest advantages though are economic as they can be inexpensively manufactured through well-established micro-machining and micro-fabrication techniques, and have

significant cost savings due to the elimination of the membrane. However, micro-fluidic fuel cells suffer from low volumetric and gravimetric energy densities due to single pass use of liquid electrolytes. Implementation of a recirculation system would be difficult due to space constraints. Their most prominent limitation though is due to their inherent micro-fluidic design and inflexible liquid-liquid platform. Furthermore, scale up of this technology is not possible as laminar flow can no longer be maintained in larger channels as the Reynolds number is a function of the characteristic length. The Reynolds number is defined as follows:

$$Re = \rho v L / \mu \quad (4.1)$$

where Re is the dimensionless Reynolds number, ρ is the fluid density in kg/m^3 , v is the fluid velocity m/s, L is the characteristic length in m, and μ is the kinematic viscosity in kg/ms . Due to this laminar flow-based fuel cells are limited in scale and can only operate on a liquid fuel-liquid oxidant platform.

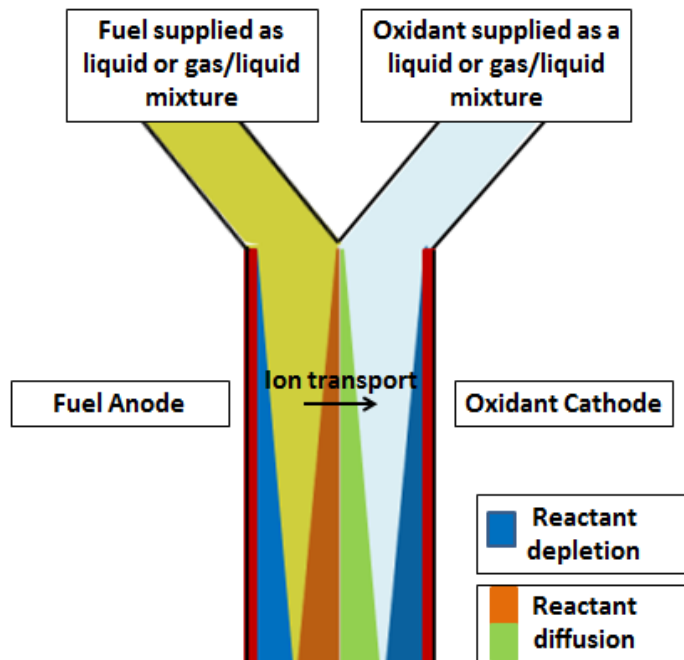


Figure 4.3: Schematic showing the basic operation of laminar flow based fuel cells. Also shown are the areas of depletion and mixing of reactants.

Mixed reactant fuel cells on the other hand rely on the selectivity of the anode and cathode catalysts to separate the oxidation and reduction reactions. A conceptual schematic of a mixed reactant fuel cell may be found in Figure 4.4. The anode should be active and selective towards fuel oxidation while the cathode should be active and selective towards oxidant reduction. As the catalysts on both electrodes are highly selective, the fuel and oxidant may be supplied together in a completely mixed stream under single-phase or two-phase flow conditions depending on the system. Ionic conductivity between the electrodes is supplied by convection, diffusion, migration and chemical reaction while electrical insulation between the electrodes can be maintained by physically keeping them separate. Mixed reactant fuel cells offer several advantages over conventional systems as they allow for more compact designs due to reduced manifolding, sealing, and storage requirements. Reduced components also have a secondary advantage in that they generally have lower production and material costs for the system. However, mixed reactant fuel cells often suffer from relatively lower activity of the selective catalysts and dilution of both the oxidant and fuel streams leading to lowered Nernst potentials. This can lead to lower fuel cell performance though their compact nature allows them to generally have higher system gravimetric or volumetric power and energy densities over conventional fuel cells. Mixed reactant fuel cells are still in early stage development but they are not expected to face the same scalability challenges as laminar flow fuel cells. Shukla et. al [71] and Priestnall et. al [72] provide two very good reviews on mixed reactant fuel cell technology.

In this thesis a major goal is to demonstrate a novel concept to achieve a fully scalable active membraneless fuel cell configuration that offers significant advantages with respect to

operational flexibility (liquid/liquid, gas/liquid systems) and scalability over other membraneless fuel cell designs without compromising fuel cell performance.

In the direct fuel redox fuel cell, the air cathode is substituted with a liquid redox species based cathode. This as discussed earlier in the thesis has several advantages including no thin-film triple phase boundary constraint, no precious group metal (PGM) catalyst requirements as well as reduced balance of plant components. The lack of a thin-film triple phase boundary constraint is the most crucial benefit of this system with respect to achieving a membraneless fuel cell configuration.

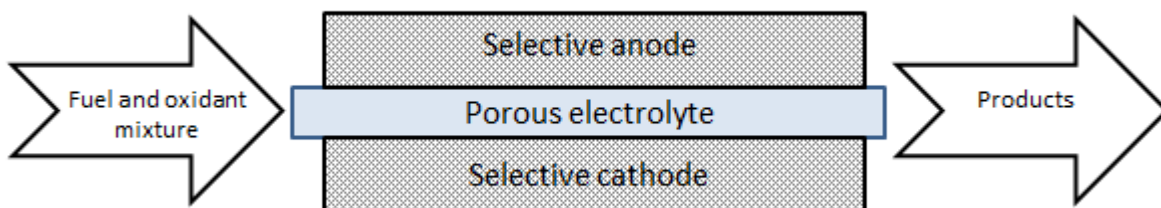


Figure 4.4: Schematic showing the basic operation of mixed reactant fuel cells.

In the direct fuel redox fuel cell, the air cathode is substituted with a liquid redox species based cathode. This as discussed earlier in the thesis has several advantages including no thin-film triple phase boundary constraint, no precious group metal (PGM) catalyst requirements as well as reduced balance of plant components. The lack of a thin-film triple phase boundary constraint is the most crucial benefit of this system with respect to achieving a membraneless fuel cell configuration.

According to the triple phase boundary constraint, shown in Figure 4.5, a reaction will only occur where all three components; reactant, electrically connected catalyst and ionically conductive electrolyte are present. In conventional PEM-based systems where the reactant

(oxygen, hydrogen or both) is a gas this reaction zone is effectively limited to a thin film right next to the membrane leading to poor utilization of the catalyst layer if it is too thick. However, when liquid fuel (e.g., methanol) or liquid oxidant (e.g., aqueous $\text{Fe}^{3+}/\text{Fe}^{2+}$) are used the reaction zone can be extended by virtue of the liquid electrolyte which provides ionic conductivity to the entire thickness of the electrode. While the reaction zone of a gaseous reactant would be across the x-y plane of the electrode at the surface right next to the membrane, as shown in Figure 4.5 and 4.6, the reaction zone of a liquid reactant will be three dimensional and include the thickness (z-direction), of the electrode as well. This lack of a thin-film triple phase boundary constraint and the presence of a 3-D electrode are at the cornerstones of this new membraneless fuel cell approach.

As the liquid reactant diffuses across the thickness, τ , as shown in Figure 4.6, of the electrode it will be consumed due to the electrochemical reaction. Consequently, a concentration gradient of the reacting species will develop across the depth of the electrode while the concentration across the plane, x-y of the electrode parallel to the membrane will be relatively constant. Thus, by controlling the thickness, hydrophobicity and porosity of the electrode one may be able to control the concentration gradient and ensure more complete utilization of the reactant. With sufficient reaction of the reactant to significantly lower its concentration depolarization and mixed potential performance losses related to crossover effects may be reduced or eliminated. If this can be achieved then use of the membrane with respect to prevention of mixing of reactants becomes redundant. With the use of a simple, off-the-shelf spacer electrical insulation between the electrodes can be provided by physically keeping the electrodes separate. Finally, ionic conductivity between the electrodes

is provided by the products from the reaction, water and supporting electrolyte (e.g., acid) added to the incoming reactant stream(s).

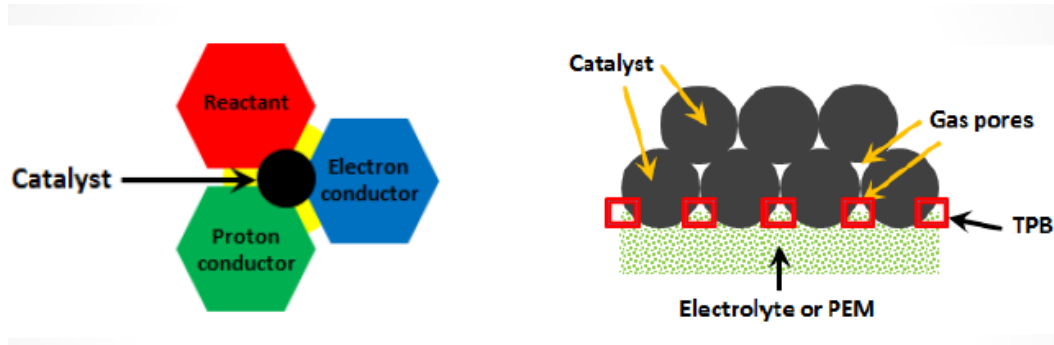


Figure 4.5: Illustration of the thin-film triple phase boundary (TPB) showing poor utilization of catalyst due to a limited reaction zone.

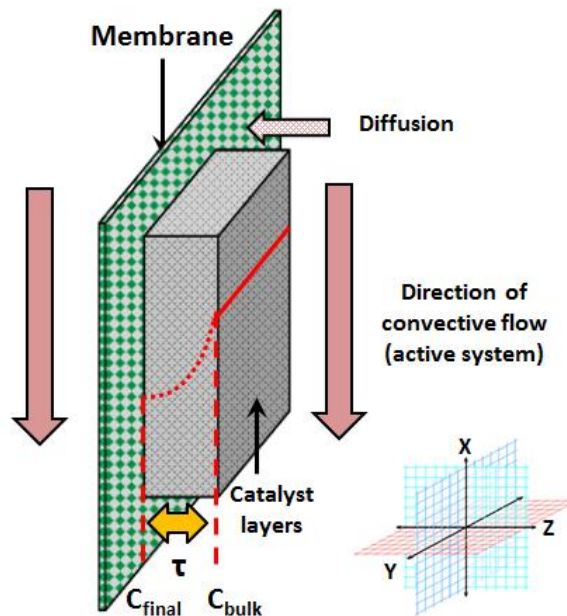


Figure 4.6: Illustration of a concentration gradient developing across the thickness of a 3-D electrode when liquid reactants are used.

The ion-exchange membrane can therefore be replaced with an open-spacer and supporting electrolyte with the use of a 3-D electrode as shown in Figure 4.7. Replacing the expensive ion-exchange membrane (which is often subject to contamination and thus

lowered conductivity) with highly ionically conductive electrolytes and inexpensive spacers should reduce fuel cell performance losses related to ohmic overpotentials. However, this is only true when the electrode is optimized for complete (or very close to) consumption of the reactant. If the concentration of the reactant as shown in Figure 4.7 at the point closest to the gap (C_{final}) is not sufficiently low then crossover effects as previously discussed will continue to pose a problem. On the other hand, if the reactant is completely consumed much before the gap any unutilized electrode will contribute to increased ohmic resistance and thus increased fuel cell performance losses. The approach now becomes an optimization problem with respect to electrode design (hydrophobicity, porosity, thickness, etc.) where crossover and ohmic resistance losses must be balanced. In addition, the careful control of operating conditions, pressure across the gap and flow channel design will also play an important role in elimination of the membrane.

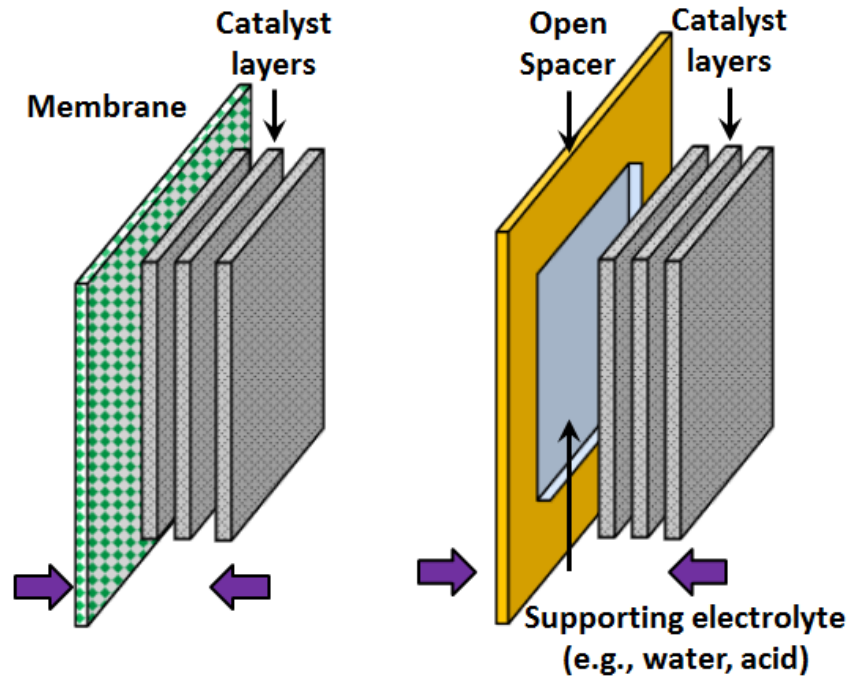


Figure 4.7: Illustration showing the proposed replacement of the membrane with a 3-D electrode structure, supporting electrolyte and an open-spacer. 3-D electrode created by stacking of multiple catalyst layers.

5 Experimental Approach and Methods

In this work advanced 3-D cathode structures were used and engineered to act not only as the cathode but also as a convection and diffusion barrier to reduce the concentration of the redox electrolyte across the thickness of the cathode. The hydrogen redox fuel cell was evaluated for the following parameters:

- i. **Cathode architecture and structure:** Use of different hydrophobic and hydrophilic GDLs, MPLs and diffusion barriers can significantly impact fuel cell performance. A combination of knowledge gained from preliminary work and literature information was used to limit the number of permutations of potential combinations for fuel cell testing. In addition thickness ($\text{mg}/\text{cm}^2 \text{ C}$) of the cathode was expected to have a significant impact on fuel cell performance by changing the reaction zone. If all other parameters are constant the thickness of the reaction zone determines both crossover rates and electrode assembly resistance. Different thicknesses of the cathode were investigated by stacking different number of layers from the electrode.
- ii. **Flow rate:** Fuel and oxidant flow rates affect fuel cell performance by improving transport of the reactant species to, and removal of the products from the catalyst sites. In addition, for membraneless fuel cell architecture it is important to manage the pressure differential across the gap between the anode and cathode in order to reduce crossover of the redox species. Fuel cell performance was evaluated over different oxidant flow rates.
- iii. **Temperature:** Temperature is likely to improve the kinetics of the system and conductivity of the electrolytes which should improve fuel cell performance by lowering both activation and ohmic losses.

- iv. **Anode Pt-catalyst loading:** Fuel cell performance was investigated to determine the effect of the catalyst loading on fuel cell performance. The use of the liquid acid electrolyte can potentially provide more effective ionic conductivity throughout the anode catalyst. This should effectively increase the number of TPS present for the HOR which should allow for the reduction in anode catalyst loadings.
- v. **Fuel cell humidification:** In absence of the membrane hydration of the system should not significantly affect fuel cell performance. However, its effect was still investigated.

The parameters discussed above were investigated to determine their effect on fuel cell performance on the membraneless DHRFC performance by determining characteristic polarization curves. A demonstration of the flexibility of the controlled reactant gradient membraneless fuel cell approach was performed with a preliminary study of the membraneless DMRFC. In addition, durability testing to demonstrate the stability of the membraneless DHRFC system was performed at 100 mA/cm² and 400 mA/cm² and at 100 mA/cm² for the membraneless DMRFC.

5.1 Fuel Cell Gaskets Fabrication

Fuel cell gaskets are required for proper sealing of the fuel cell as well as to ensure proper electrical contact between the electrodes and the flow field plates. If the gasket is too thick electrical contact between the electrode and the flow plates will be poor while if the gasket is too thin poor sealing may result in reactant leaks. Similarly, compression of the gasket and electrodes under pressure is also an important consideration to ensure proper electrical contact without irreversibly damaging the electrodes. Finally, it is important to ensure material compatibility between the electrodes and the reactants.

The gaskets for the fuel cell were prepared by using molds machined especially for our fuel cell. JRTV silicon was mixed with a curing agent in a ratio of 10:1 in a pre-weighed vessel. The vessel was placed inside a chamber and evacuated to around 30 mmHg. The mixture was removed from the chamber and poured into the molds with a syringe and any excess silicone removed. The mold was then cured at 80°C for at least one hour and the seals removed.

5.2 Electrode and Electrode Assembly Fabrication and Treatment

The use of a 3-D electrode is fundamental in our approach towards the realization of a membraneless fuel cell. As discussed earlier the hydrophobicity, thickness and porosity of the 3-D electrode has a significant effect on the performance of the fuel cell. Consequently, some level of optimization of these parameters is important. Although, full optimization of the electrodes is beyond the scope of the objectives of this thesis it was still important to be able to control these parameters to a sufficient degree to demonstrate comparable performance of the membraneless architecture with conventional membrane electrode assemblies (MEA).

Electrode fabrication consisted of the following steps:

- Choosing a gas diffusion/electrode backing layer (e.g., Toray TGP-H-090 Carbon paper)
- Choosing a catalyst for the electrode (e.g., X% Pt/Ru on Vulcan XC-72, Pt/Ru black for anode catalyst, Vulcan XC-72 for cathode catalyst, etc.)

- Choosing a composition of ionomer and catalyst for the electrode (e.g., 30% Nafion and 70% Pt/Ru black, 20% PTFE and 80% Vulcan XC-72, etc.)
- Preparation of the specified compositions of catalyst ink – calculations and preparation instructions in detail can be found in Appendix A
- Spraying of the catalyst ink on to the gas diffusion layer until a desired loading is achieved ($X \text{ mg/cm}^2$) – detailed spraying instructions can be found in Appendix A

Further instructions for adding a carbon sublayer to the electrode can also be found in Appendix A. The ink was applied to the GDL using an isopropanol cleaned Accuspray spray gun (15 psi pressure). Any ink not being use while spraying was continuously stirred using a magnetic stir bar to ensure a homogeneous mixture. The gas diffusion layer to be sprayed on was weighed and placed on a hot-plate at a temperature of 90°C . This allowed the water and isopropanol during spraying to evaporate leaving the melted ionomer and catalyst on the surface of the GDL only. As the melted ionomer cooled it bound the catalyst powder to the surface of the GDL. The GDL was weighed periodically during spraying until the desired catalyst loading was reached (change in mass related to area sprayed). Once the desired loading had been reached the electrode was dried and using custom built cutting tools the required area of the electrode for the fuel cell was cut from the larger sprayed electrode as required.

A 0.67 mm silicone rubber gasket material with adhesive on one side was used for the membraneless electrode assembly. The following steps were performed to create the membraneless electrode assembly:

1. The JRTV silicone gaskets (not to be confused with the 0.67 mm silicone rubber sheet) were placed in their mold in the anode and cathode flow field plates.

2. Cut a polyimide (Kapton®) square the size of the flow field plates. Using a 1.8 cm x 1.8 cm dye a square was cut in the middle of this film to make a frame.
3. The anode was placed on the anode flow channels. The cut Kapton® frame was unpeeled and stuck to the anode with the 1.8 cm x 1.8 cm square centred on the anode evenly and only touching the edges of the 2 cm x 2 cm anode. The rest of the Kapton sheet was then to the anode plate.
4. The desired architecture of the 3-D cathode was stacked onto the cathode flow channels. A silicone rubber gasket was cut the same size as the flow field plates. The 1.8 cm x 1.8 cm dye was used to cut a square in the middle of this sheet.
5. The 1.8 cm x 1.8 cm square frame silicon rubber gasket was stuck on the stacked cathode and cathode flow plate. It was ensured that only the edges of the 2 cm x 2 cm cathode are in contact with the silicone rubber sheet.

For baseline conventional membrane electrode assembly (MEA) testing Nafion® membranes were used. The Nafion membrane was treated by heating at 80°C for 2 hours in 3 wt% H₂O₂. The membrane was then thoroughly rinsed with deionized water and boiled in 15 wt% H₂SO₄ for 2 hours. Finally, the membrane was rinsed three times, for 30 minutes each time in deionized water and stored in deionized water for later use.

5.3 Electrolyte Preparation

All electrolytes were prepared using deionized water with the chemicals used as received from the suppliers. The chemicals used and their suppliers are listed below:

- Ferric Perchlorate Hydrated Non-yellow – GFS Chemicals
- Ferrous Perchlorate – Sigma Aldrich
- Ferric Ammonium Sulfate Dodecahydrate – Fisher Scientific

- Ferrous Sulfate Heptahydrate – Fisher Scientific
- Methanol Electronic Grade – Fisher Scientific
- Perchloric Acid 70% - Fisher Scientific
- Sulfuric Acid 99.9% - Fisher Scientific

All iron catholyte solutions unless otherwise stated were made to a Fe^{3+} to Fe^{2+} ratio of 9:1 to simulate conditions in real redox flow systems.

5.4 Fuel Cell Testing System

The fuel cell testing system was designed to allow the characterization of alternative fuel cell components and cell operating conditions. The system allowed for the following parameters to be investigated:

- Fuel cell design and operating conditions: flow fields, gaskets, gap between electrodes, temperature, flow rate, cell compression pressure, etc.
- Catalysts and electrodes: carbon fiber paper, carbon felts, Nafion ionomer, Teflon loading, etc.

A schematic of the 4 cm² fuel cell used for testing is shown in Figure 5.1 while detailed engineering diagrams of some of the fuel cell components may be found in Appendix B. Although the use of a pocket volume on the cathode side would allow for better utilization of the 3-D cathode area only serpentine channels were used to allow for better control of flow in the system. However, serpentine flow channels of different dimensions were used for both the anode and cathode.

The fuel cell was operated in a horizontal orientation with the cathode plates on the bottom. The liquid acid electrolyte solution was supplied to the fuel cell by filling the raised volume above the cathode which is enclosed by the silicone rubber gasket using a pipette. The anode side components were placed on the cathode in the correct orientation, i.e., facing the cathode. The fuel cell was assembled and compressed with a pressurized air bladder to the required pressure. A Solartron 1480 Multistat was electrically connected to the fuel cell current collectors to allow for different voltage and current measurements to be performed. The overall fuel cell system allowed for control of reactor temperature, oxidant and fuel temperature, and reactant flow rates. A schematic of both the methanol and hydrogen redox fuel cell systems is shown in Figures 5.2 and 5.3, respectively. The different system components used for fuel cell testing for the hydrogen and methanol fuel cell testing are summarized as follows:

- Peristaltic pump for controlling oxidant flow
- Peristaltic pump for controlling methanol fuel flow for direct methanol redox fuel cell
- A calibrated gas flow meter for control of hydrogen flow rates available from McMaster Carr
- A Haake water bath for heating of both the oxidant and methanol fuel streams for the direct methanol redox fuel cell
- Heating tubes from Claybourne for heating and maintaining the temperature of the electrolytes
- Heating strips from Omega attached to the back of current collectors for controlled heating of the fuel cell

- A custom built temperature control box for controlling the temperature of all heating equipment (heating strips, tube, heaters, etc.)
- A modified gas humidifier to heat the hydrogen stream without humidification for the direct hydrogen redox fuel cell
- A gas humidifier to humidify and heat the hydrogen stream for the direct hydrogen redox fuel cell
- Teflon tubing and Teflon Swagelok components for methanol fuel and oxidant flow
- Stainless steel tubing and stainless steel Swagelok components for hydrogen fuel flow

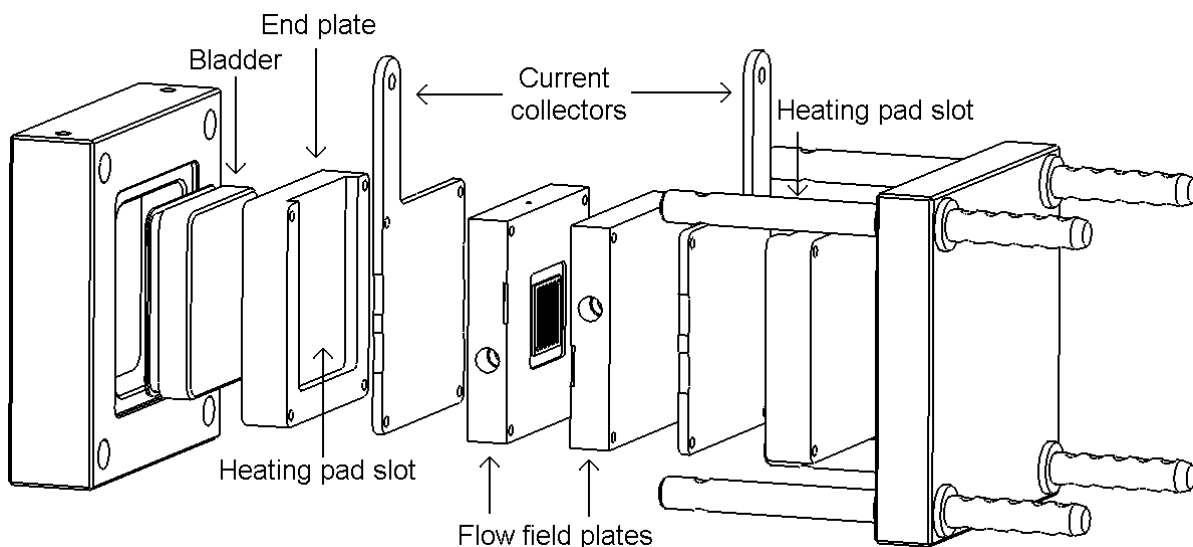


Figure 5.1: Schematic of the 4 cm² fuel cell used for testing showing all components.

All polarization curves were generated with both the fuel and redox catholyte flowed in a single pass flow system to allow for better control of experimental conditions and to simulate a regenerated solution. Once the temperature of the fuel cell with flowing electrolytes stabilized the polarization curve was generated with galvanostatic experiments. During galvanostatic operation individual current points were analyzed until voltage

oscillations were within 5 mV for the membraneless DHRFC and 10 mV for the membraneless DMRFC (usually less than 5 minutes). All durability tests were performed by recirculating 0.5 L of the catholyte while the hydrogen or methanol fuel was flowed in a single pass configuration.

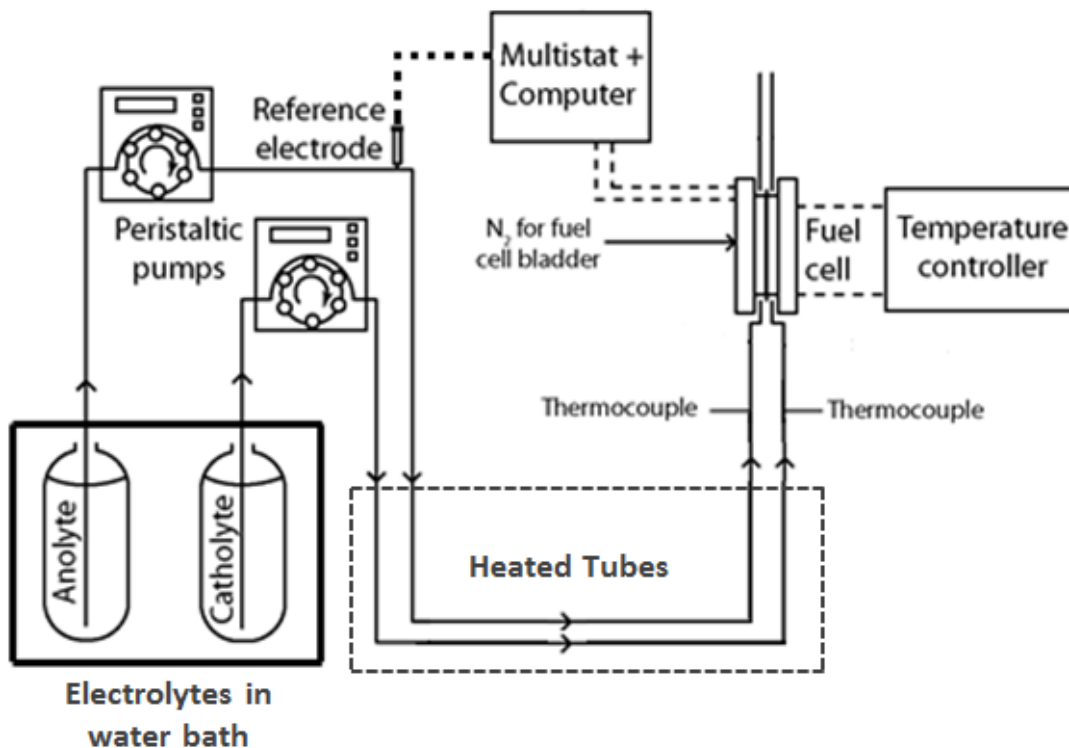


Figure 5.2: Schematic of the direct methanol redox fuel cell testing system showing all components used for temperature, flow and pressure control.

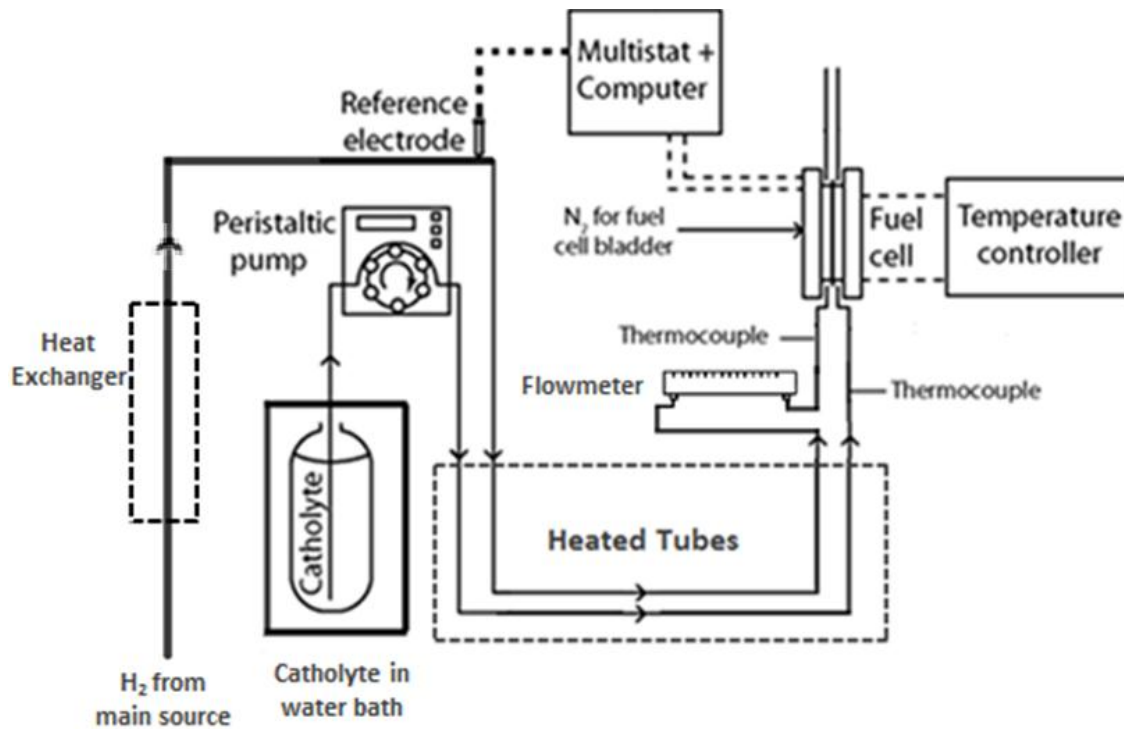


Figure 5.3: Schematic of the direct hydrogen redox fuel cell testing system showing all components used for temperature, flow and pressure control.

6 Results and Discussions

6.1 Development of a Membraneless Electrode

Assembly for an Active Fuel Cell System

Replacing the air cathode of a conventional polymer electrolyte membrane fuel cell (PEMFC) with an iron redox species cathode of a redox flow battery has several advantages. The exchange current density of the $\text{Fe}^{3+}/\text{Fe}^{2+}$ couple ($\sim 10^{-2}$ A/cm²) on carbon [62] is several orders of magnitude higher than that of the oxygen reduction reaction (ORR) ($\sim 10^{-10}$ A/cm²) on Pt [63]. Furthermore, the mass transport of iron to catalyst sites is significantly better due to the solubility of certain iron salts (greater than 1 M for ferric perchlorate, ferric ammonium sulfate, etc.) is several orders of magnitude greater than the solubility of oxygen in water, 10^{-4} M [73]. Due to these two factors the rate of the cathode reaction is significantly faster even on non-PGM catalysts than that of the ORR on PGM-catalysts.

The use of a liquid redox species cathode also has the added advantage of an extended triple phase boundary which allows for the elimination of the membrane and issues associated with it by the use of a 3-D cathode and an open spacer (see “Thesis Research Approach” for detailed explanation). For this membraneless electrode assembly architecture to successfully provide the functions of the membrane; provide ionic conductivity and electrical insulation while preventing reactant mixing, the design of the following components must be carefully controlled:

- **Porosity, hydrophobicity and thickness of the cathode:** These aspects of the cathode are important to control convective flow of the oxidant in the flow channels and ensure diffusion only mass transport into the 3-D cathode. Failing to control

convective flow will lead to excessive amounts of oxidant reactant flooding the cathode where consumption of the oxidant is not sufficient to prevent/mitigate crossover.

- **Porosity and hydrophobicity of the anode:** Ensuring the acidic liquid electrolyte that replaces the membrane remains in the gap between the anode and cathode is important to maintain ionic contact between the electrodes. High rates of evaporation of the electrolyte into the hydrogen fuel stream will cause fuel cell operation failure due to a lack of ionic conductivity between the electrodes. Loss of the electrolyte into the fuel stream can be reduced by controlling the hydrophobicity and porosity of the anode.
- **Anode and cathode flow field channels:** In the absence of a membrane the design of the flow field channels can be used to create a favorable pressure differential across the gap between the anode and the cathode. A couple of extreme examples can be considered: for a specified cathode flow channel size a solid block with no channels on the anode side will have no pressure driven crossover while an anode side open to the atmosphere will have significantly higher rates of crossover.
- **Open spacer thickness:** This aspect refers to the thickness of the gap between the anode and cathode. A larger distance between the anode and cathode will decrease crossover effects by creating larger resistance to diffusion. However, a larger gap between the anode and cathode also increases ionic resistance between the electrodes resulting in increased ohmic losses.

6.1.1 Cell Architecture and Components

Taking the above factors into account an electrode assembly design as shown in Figure 6.1 was developed. The components of the membraneless architecture and their respective functions in this architecture are as follows:

1. **Anode and cathode flow channels (components 1 and 7, Figure 6.1):** Smaller cross-sectional area of the flow channels compared to the cross-sectional area of the landing widths at the anode helps reduce crossover by reducing the amount of area open for pressure driven flow from the cathode to the anode. Cathode flow channels of 0.84 mm (width) x 1 mm (depth) with landing widths of 0.84 mm and anode channels of 0.20 mm (width) and 0.15 mm (depth) with landing widths of 0.42 mm were used. Therefore, the area of the flow channels for the cathode and anode is approximately 185 mm² and 132 mm², respectively. While the total area of the landings for the cathode and anode is approximately 295 mm² and 352 mm², respectively. This significantly reduces crossover of the redox catholyte as discussed earlier. Complete dimensions of the anode and cathode flow channels and plates can be found in Appendix B.
2. **Anode design (component 2, Figure 6.1):** The anode was created by a spray deposition method. Though the Pt-content in the catalyst layer was varied the structure of the anode was uniform throughout the testing. The anode structure consisted of Teflon containing carbon sub-layer sprayed onto a highly hydrophobic gas diffusion layer as per the instructions provided in Appendix A. A Nafion® ionomer containing Pt-catalyst layer of a specified loading was then added on to the hydrophobic micro-porous carbon sub-layer. The hydrophobic carbon micro-porous layer and gas diffusion layer are required to keep the acid electrolyte in the gap and prevent it from escaping with the fuel stream

in the anode flow channels. Though some electrolyte will still evaporate and leave in the fuel stream the rate of evaporation is low enough for the electrolyte to be replaced from the cathode stream. Furthermore, preventing rapid loss of electrolyte prevents the vacated space from being flooded with the catholyte which exacerbates crossover issues. The anode used had a 1 mg/cm² carbon sublayer (80% Vulcan XC-72, 20% PTFE) and a catalyst layer with a specified loading of 20% Pt/C (0.2/0.1/0.05 mg/cm² Pt, 30% Nafion® in catalyst layer) sprayed onto a 20% wet-proofed (WP) BASF TGP-H-090 GDL.

3. **Cathode design:** The cathode was created by stacking discrete segments to allow for easy control of hydrophobicity, porosity and thickness. In general the cathode was created with three segments with their functions as follows:
 - i. **Hydrophobic gas diffusion layer (component 6, Figure 6.1):** this layer was required to reduce convective flow of the iron redox electrolyte into the 3-D cathode and ensure mainly diffusion based transport through the 3-D cathode. This allows better control of the reaction zone and concentration gradient, the control of which is imperative for elimination of the membrane. A SIGRACET 25 DA or 25 BC GDL from SGL carbon was used for this layer. Dynamic contact angles of water with a water droplet size of 0.5 µl on a SIGRACET 25 DA GDL is shown in Figure 6.2. Contact angles are a method of measuring the hydrophobicity of a surface. A contact angle less than 90° is associated with a hydrophilic surface while a contact angle in the range of 90-150° is associated with a hydrophobic surface. Any contact angles greater than 150° are associated with super-hydrophobic surfaces. It can be seen in Figure 6.2 that the 25 DA GDL is a super-hydrophobic surface with a

contact angle of 166° . This helps control convection while the porosity of this GDL allows effective reactant diffusion to the rest of the cathode.

- ii. **Hydrophilic gas diffusion layer (component 5, Figure 6.1):** Ensuring reactant consumption once the iron redox electrolyte has permeated past the hydrophobic layer is the second step in the design to mitigate oxidant crossover effects. However, it is also important that the liquid electrolyte in the gap has good ionic contact within the 3-D cathode to reduce ohmic resistance related to ion transport. To this extent a hydrophilic gas diffusion layer acts as a low transport-resistant but high surface area reaction zone which balances ionic transport and reactant consumption. A pre-treated BASF TGP-H-120 or TGP-H-060 with no WP CFP GDL was used for this layer. Pre-treatment with boiling in 1 M HNO_3 (30 minutes) improves makes the pores more hydrophilic. The thickness of the electrode was managed by stacking different number of these layers.
 - iii. **Hydrophilic micro-porous layer (component 4, Figure 6.1):** This layer is the final barrier before any unreacted redox electrolyte enters the gap. A thin low porosity layer hinders diffusion of the reactant and improves reactant utilization without increasing resistance to ionic transport. Unless otherwise stated a 1 mg/cm^2 C (90% Vulcan XC-72, 10% Nafion®) micro-porous layer sprayed onto a TGP-H-090 with no WP GDL was used here.
4. **Open spacer:** A silicon rubber open spacer was used to physically keep the electrodes from coming in contact with each other. The material of the spacer is not important as long as it is chemically compatible but its thickness is. Another factor that had to be considered for the spacer thickness was electrode bowing during flow due to uneven pressure distribution on

the entire area of the electrode which can potentially create an electrical short-circuit in the fuel cell. The 0.67 mm open spacer used in this work was thick enough to avoid any issues with electrode bowing.

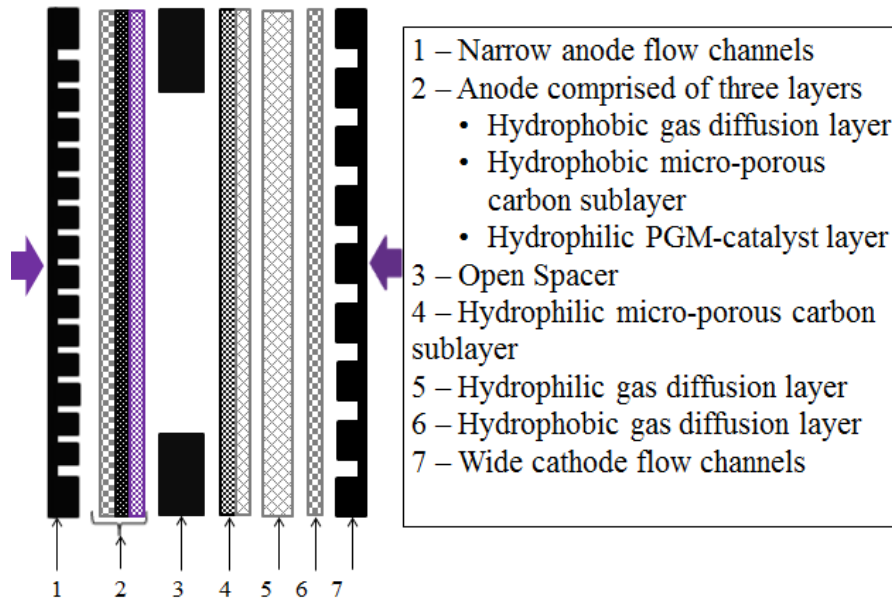


Figure 6.1: Conceptual schematic of the membraneless electrode assembly utilizing the 3-D cathode, conventional anode and open-spacer in the DHRFC.

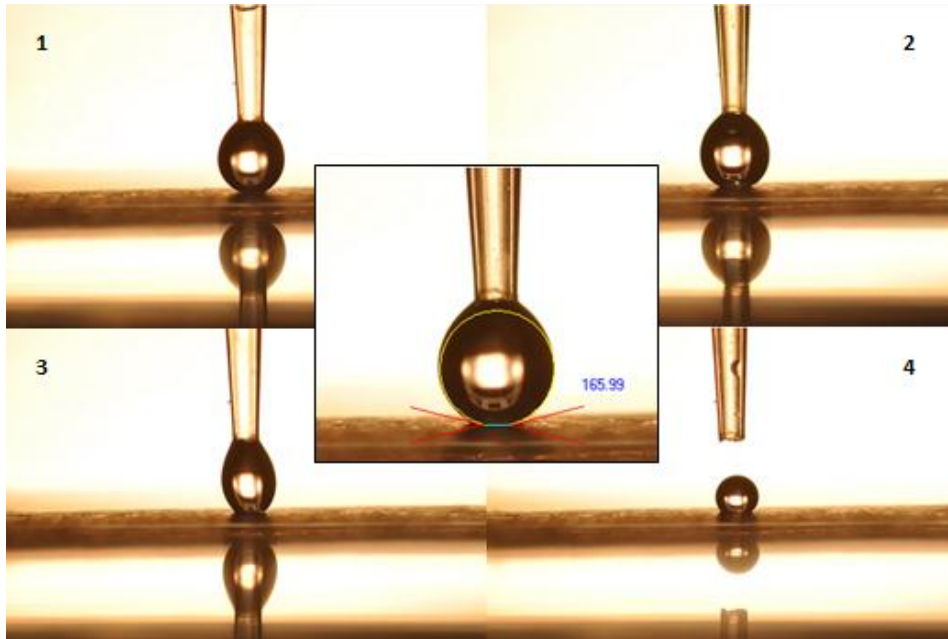


Figure 6.2: Dynamic contact angle measurements of a Sigracet 25 DA GDL showing contact angle of 166°. Insets 1-4: Water droplet being brought close to surface and then being removed.

6.2 The Membraneless Direct Hydrogen Redox Fuel Cell

The direct hydrogen redox fuel cell was operated using the membraneless electrode assembly developed in the previous section. Fuel cell performance of this membraneless electrode assembly was investigated for different parameters including iron redox catholyte flow rate, fuel cell temperature, 3-D cathode thickness and anode Pt-catalyst loading. In addition, this membraneless electrode assembly was compared with the conventional Nafion® 112 membrane electrode under the same operating conditions.

6.2.1 Effect of Iron Redox Catholyte Flow Rate

Figure 6.3a shows the effect of redox electrolyte flow rate on fuel cell performance while all other factors were kept constant. Shown in Figure 6.3b is a close-up of the kinetic region ($< 35 \text{ mA/cm}^2$) of the same polarization data. It was expected that increasing flow rate would affect fuel cell performance in two ways; i) lowering OCV due to higher crossover rates for the membraneless architecture and ii) improving 3-D cathode utilization by improving transport to the catalyst sites.

Measured OCV in the range of 0.805 – 0.835 V at the flow rates shown does not compare well with the theoretical Nernst equilibrium potential of 0.909 V at the same conditions ($P_{\text{H}_2} = 2 \text{ atm}$, $\text{pH} = 1$, $[\text{Fe}^{3+}] = 2 \text{ M}$, $[\text{Fe}^{2+}] = 0.22 \text{ M}$). The lowered OCV in comparison to the Nernst value is attributed to differences in actual activity and values used to calculate the theoretical Nernst potential. In addition crossover of the liquid redox catholyte also creates mixed potentials at the anode lowering the measured OCV. As seen in Figure 6.3b increasing flow rate from 3 ml/min to 4 ml/min and 6 ml/min decreased the OCV as crossover of the iron redox catholyte increased. Fuel cell performance in the kinetic region

(< 35 mA/cm²) was not affected by an increase in iron redox catholyte flow rate though an offset in cell voltage is observed in this region. This offset is attributed to increased crossover effects lowering cell voltage though relative losses in the kinetic region are similar. A clear activation region was not observed as evidenced in the linear polarization curves. This is likely due to the extremely good kinetics of this system; both the Fe³⁺/Fe²⁺ redox couple on carbon (10⁻² A/cm²) and the hydrogen oxidation reaction (HOR) on Pt (10⁻³ A/cm²) have relatively high exchange current densities. Due to this activation losses for this system are likely very low and the polarization curve is dominated by ohmic overpotentials.

Overall fuel cell resistances at OCV for this architecture were determined to be 0.10 Ω, 0.10 Ω, 0.10 Ω and 0.09 Ω for 2 ml/min, 3 ml/min, 4 ml/min and 6 ml/min of the iron redox catholyte flow rate, respectively. Though fuel cell resistance improves slightly with flow rate improvements in fuel cell performance in the ohmic region are more likely associated to improved concentration of redox species at the catalyst sites due to improved mass transport.

Fuel cell performance was significantly mass transport limited below a certain threshold flow rate of 4 ml/min due to fuel cell design limitations. These design issues lead to poor reactant distribution and incomplete utilization of the full 3-D cathode geometry. Increasing the flow rate past 4 ml/min utilizes more of the 3-D cathode geometry preventing the fuel cell becoming mass transport limited. At higher current densities mass transport improvements due to higher diffusion improve fuel cell performance by improving the concentration of the redox species over the whole geometry of the electrode. Table 6.1 summarizes the amount of reactant utilized at different flow rates at 400 mA/cm² and 800 mA/cm². Further optimization of the cathode is likely to improve fuel cell performance.

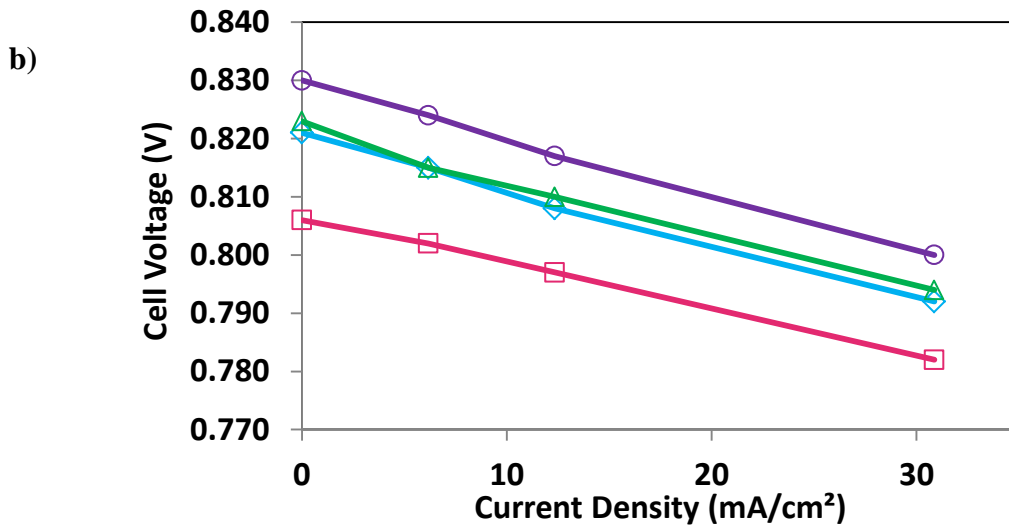
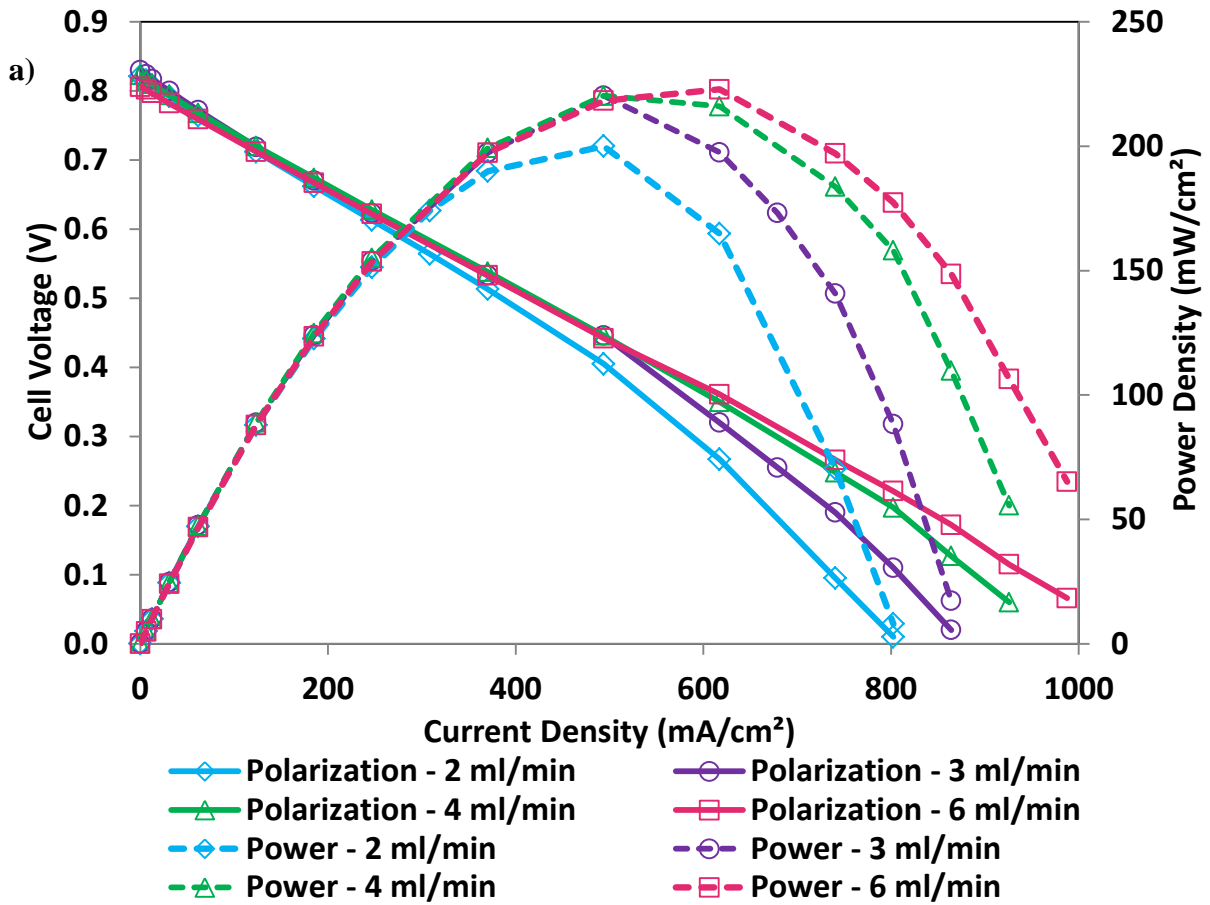


Figure 6.3: Effect of iron redox catholyte flow rates on fuel cell performance at 60°C. a) Polarization and power density curves. b) Close-up of activation region.

Bladder Pressure: 20 psi, Anode: 0.2 mg/cm² 20% Pt/C (30% Nafion®), 1 mg/cm² C sublayer (20% PTFE) on Toray TGP-H-090 20% WP, Cathode: Sigracet 25 DA GDL 20% WP, Toray TGP-H-120 no WP, 1 mg/cm² C MPL (15% Nafion®) on TGP-H-090 no WP, Catholyte: 2 M Fe(ClO₄)₃, 0.22 M Fe(ClO₄)₂, 0.2 M HClO₄. Fuel: 105 ml/min non-humidified hydrogen at 30 psi, Electrolyte in spacer: 0.5 M HClO₄.

Table 6.1: Amount of ferric ions consumed at different current densities at different flow rates.

Flow Rate (ml/min)	Molar Flow Rate (mol/s)	Fe ³⁺ Consumption At 400 mA/cm ² (%)	Fe ³⁺ Consumption At 800 mA/cm ² (%)
2	0.000067	20.1%	40.3%
4	0.000133	10.1%	20.1%
6	0.000200	6.7%	13.4%

A theoretical approximate calculation of limiting current, i_L , is be given by

$$i_L = k_m n F C_B \quad (6.1)$$

with an electron transfer value n of 1, Faraday's constant (96485 Coulombs/mole), a turbulent flow mass transfer coefficient, k_m , of 10^{-5} m/s (flow in the electrode surfaces close to the channels is turbulent) and a bulk redox concentration C_B of 2 M. For concentrations greater than 2 M, limiting current densities greater than 1900 mA/cm² are calculated; exceeding the maximum current density of 1000 mA/cm² achieved experimentally.

From this one can conclude that optimizing not only flow rate but also flow dynamics would be an important consideration in fuel cell design towards striking a balance between crossover rate, 3-D cathode utilization and ionic conductivity through the membraneless electrode assembly. In addition optimization of the electrodes, the electrolytes and fuel cell components to reduce fuel cell resistance are imperative.

6.2.2 Repeatability of Experiments

Figure 6.4 and 6.5 show the repeatability of experiments at the conditions shown. Figure 6.4 shows fuel cell performance reproducibility with the same membraneless electrode assembly but new components for each of the three runs. Figure 6.5 shows fuel cell test repeatability using the same membraneless electrode assembly performed with the fuel cell shutdown, cleaned and restarted after each test without changing the components. Almost identical performance was observed for repeatability tests with new components while some differences in fuel cell performance were observed with the same electrode. In addition fuel cell reproducibility at iron catholyte flow rates greater than 3 ml/min was better than at lower flow rates.

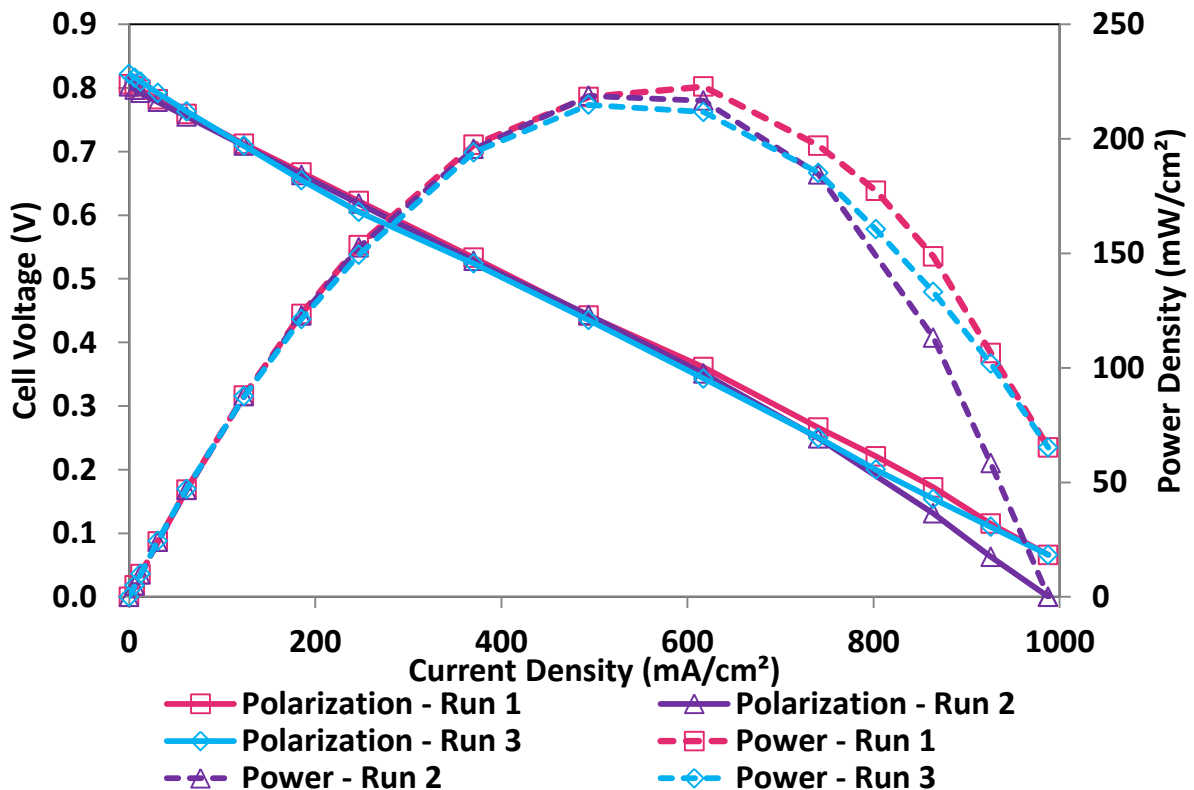


Figure 6.4: Fuel cell performance repeatability with new components for all three runs at 60°C.

Bladder Pressure: 20 psi, Anode: 0.2 mg/cm² 20% Pt/C (30% Nafion®), 1 mg/cm² C sublayer (20% PTFE) on Toray TGP-H-090 20% WP, Cathode: Sigracet 25 DA GDL, Toray TGP-H-120 no WP, 1 mg/cm² C MPL (15% Nafion®) on TGP-H-090 no WP, Catholyte: 6 ml/min 2 M Fe(ClO₄)₃, 0.22 M Fe(ClO₄)₂, 0.2 M HClO₄, Fuel: 105 ml/min non-humidified hydrogen at 30 psi, Electrolyte in spacer: 0.5 M HClO₄.

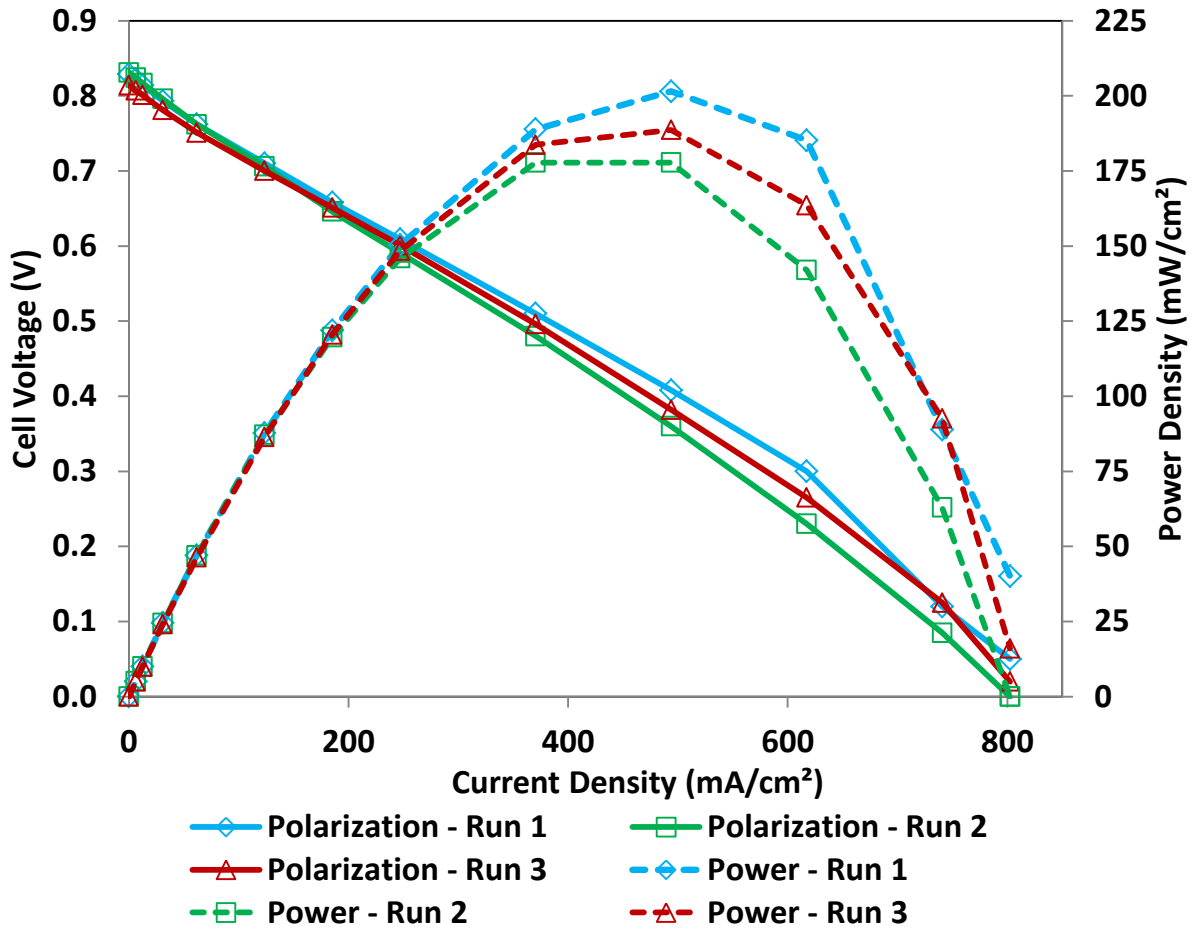


Figure 6.5: Fuel cell performance repeatability with the same membraneless electrode assembly at 60°C.

Bladder Pressure: 20 psi, Anode: 0.2 mg/cm² 20% Pt/C (30% Nafion®), 1 mg/cm² C sublayer (20% PTFE) on Toray TGP-H-090 20% WP, Cathode: Sigracet 25 DA GDL, Toray TGP-H-120 no WP, 1 mg/cm² C MPL (15% Nafion®) on TGP-H-090 no WP, Catholyte: 2 ml/min 2 M Fe(ClO₄)₃, 0.22 M Fe(ClO₄)₂, 0.2 M HClO₄, Fuel: 105 ml/min non-humidified hydrogen at 30 psi, Electrolyte in spacer: 0.5 M HClO₄.

6.2.3 Effect of Temperature

Figure 6.6a shows fuel cell performance at different temperatures with a catholyte flow rate of 2 ml/min and 30 psi hydrogen at 105 ml/min. Other experimental details may be found in the figure caption. Figure 6.6b is a close-up of the kinetic region of the same graph. Theoretical Nernst equilibrium potential as a function of temperature as shown in Figure 6.7 suggests that there should be an increase in equilibrium cell potential with an increase in temperature for this system. This is observed to a certain degree in Figure 6.6b but a more complete trend is likely masked due to crossover effects and experimental variability.

An improvement in fuel cell performance was observed with an increase in temperature. Some fuel cell performance improvement in the kinetic region ($< 35 \text{ mA/cm}^2$) was observed for the temperatures investigated. Due to the already very good kinetics of both the oxidation and reduction reactions activation overpotentials are relatively low with temperature not significantly improving the kinetics of the system.

On the other hand, significant improvements in fuel cell performance in the ohmic region were observed with an increase in temperature. Table 6.2 provides a summary of the fuel cell resistance at the temperatures investigated along with the calculated iR losses that would be expected. The conductivity of 2.5 M $\text{Fe}(\text{ClO}_4)_3$ is shown in Figure 6.8 at different temperatures. The improved conductivity of solution with an increase in temperature is likely the reason for reduced fuel cell resistance and thus improved performance in the ohmic region. Some benefits in the mass transport region were also observed at this flow rate with an increase in temperature. While the fuel cell appears to start becoming mass transport limited at around 550 mA/cm^2 at 45°C the mass transport region begins to appear after 700 mA/cm^2 at 75°C . It is unlikely that this improvement is related to increases in saturation

concentration with temperature as the solubility limit of the ferric perchlorate salt is 2.47 M at 25°C which is significantly higher than the 2.22 M total iron (2 M Fe(ClO₄)₃, 0.22 M Fe(ClO₄)₂) concentration redox catholyte used. Instead this improved performance is likely due to improved ion diffusion at higher temperatures as predicted by the Stokes-Einstein equation for diffusion coefficients with respect to temperature,

$$\frac{D_{T_1}}{D_{T_2}} = \frac{T_2 \mu_{T_1}}{T_1 \mu_{T_2}} \quad (6.2)$$

where T₂, T₁ are the temperatures in °K, μ_{T1}, μ_{T1} are the viscosities in Pa.s at the respective temperature and D_{T1}, D_{T2} are the diffusion coefficients in cm²/s at their respective temperatures.

Table 6.2: Effect of temperature on resistance and associated ohmic losses at different current densities.

Temperature (°C)	Measured Resistance (Ω)	Ohmic Loss - 300 mA/cm ² (V)	Ohmic Loss - 600 mA/cm ² (V)
45	0.13	0.126	0.253
60	0.09	0.087	0.175
75	0.07	0.068	0.136

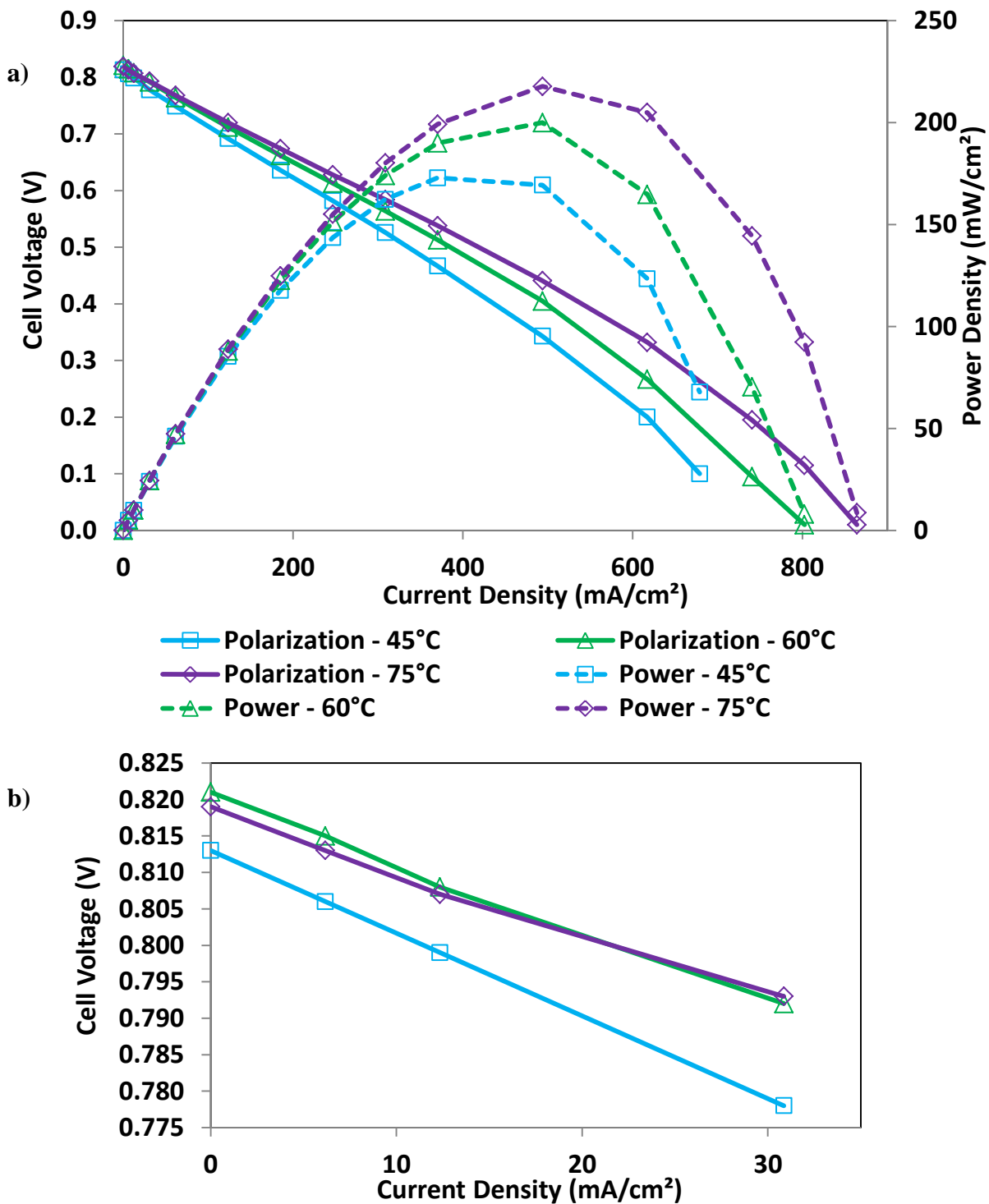


Figure 6.6: Effect of temperature on fuel cell performance. a) Polarization and power density curves. b) Close-up of activation region.

Bladder Pressure: 20 psi, Anode: $0.2 \text{ mg}/\text{cm}^2$ 20% Pt/C (30% Nafion®), $1 \text{ mg}/\text{cm}^2$ C sublayer (20% PTFE) on Toray TGP-H-090 20% WP, Cathode: Sigracet 25 DA GDL, Toray TGP-H-120 no WP, $1 \text{ mg}/\text{cm}^2$ C MPL (15% Nafion®) on TGP-H-090 no WP, Catholyte: 2 ml/min 2 M $\text{Fe}(\text{ClO}_4)_3$, 0.22 M $\text{Fe}(\text{ClO}_4)_2$, 0.2 M HClO_4 , Fuel: 105 ml/min non-humidified hydrogen at line pressure of 30 psi, Electrolyte in spacer: 0.5 M HClO_4 .

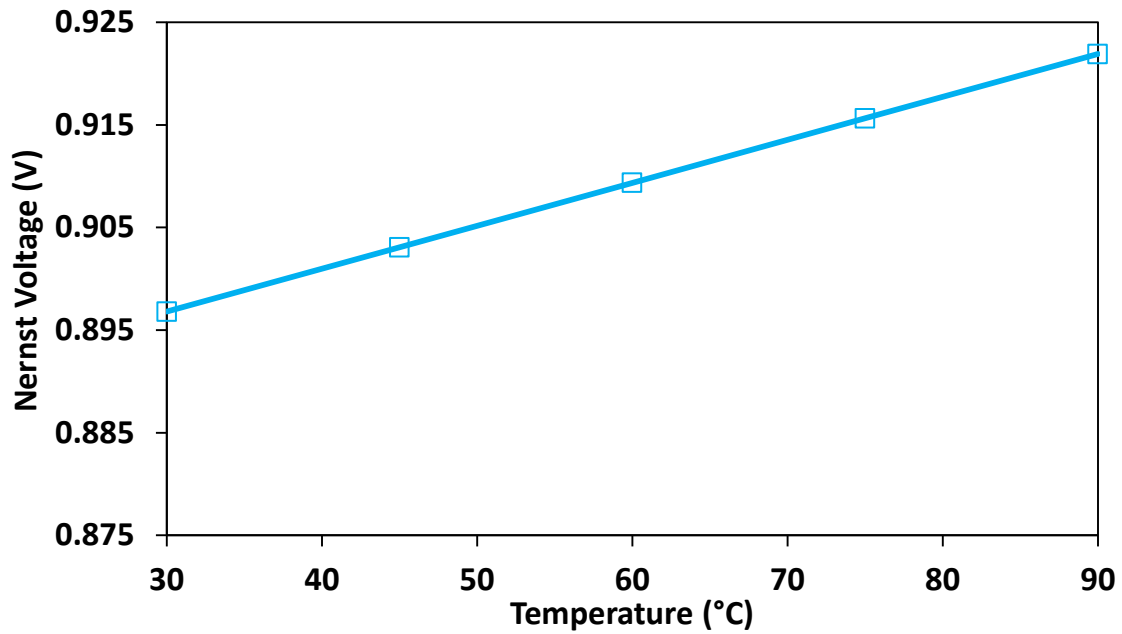


Figure 6.7: Effect of temperature on theoretical Nernst potential. $[\text{Fe}^{3+}] = 2 \text{ M}$, $[\text{Fe}^{2+}] = 0.22 \text{ M}$, $\text{pH} = 1$, $P_{\text{Hydrogen}} = 2 \text{ atm}$.

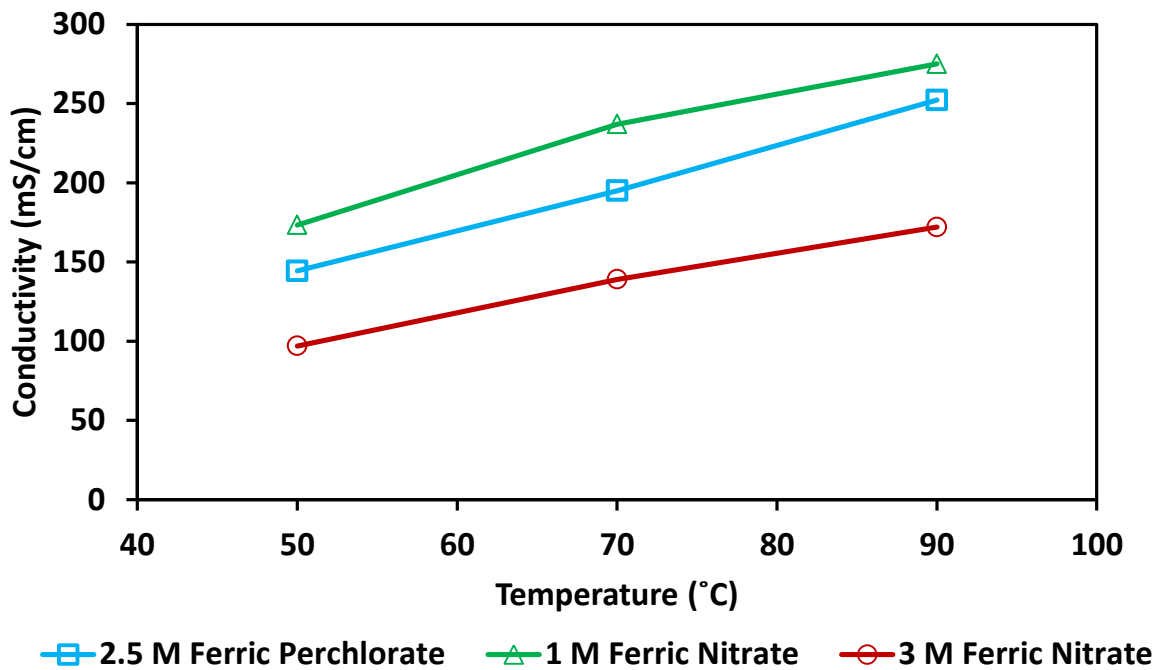


Figure 6.8: Effect of temperature on conductivity of different iron salts.

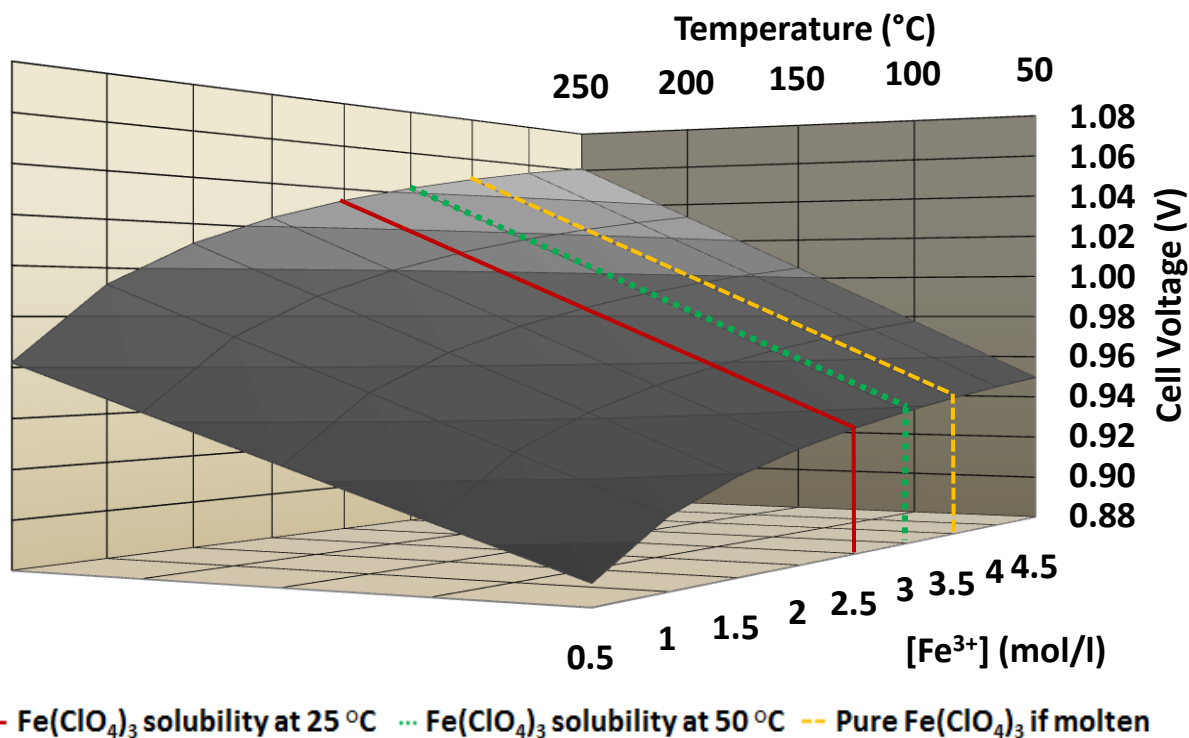


Figure 6.9: Effect of temperature and concentration of Fe^{3+} ions on theoretical cell Nernst potential with $[\text{Fe}^{2+}] = 0.1 \text{ M}$, $\text{pH} = 1$, $P_{\text{Hydrogen}} = 2 \text{ atm}$.

Most conventional PEM-based fuel cells are limited in their operating range to below 135°C (with usual operation temperature around 80°C) due to the use of Nafion® based membranes, which at elevated temperatures tend to become dehydrated resulting in losses in conductivity. In addition, increased membrane degradation at higher temperatures is also a concern. However, the membraneless electrode assembly eliminates temperature related challenges associated with the use of Nafion® membranes in these fuel cells. This elimination of the membrane should allow for fuel cell operation at significantly higher temperatures with some adjustments to the membraneless electrode assembly to accommodate elevated temperatures. Specifically the liquid acid electrolyte should be replaced with a high boiling point acid (e.g., 98% phosphoric acid) and the open-spacer

material stability at elevated temperatures should be considered. There are a number of advantages for fuel cell operation at elevated temperatures for this system including improvements in the theoretical Nernst potential as seen in Figure 6.9. This should allow for significant improvements in fuel cell performance by taking advantage of a wider potential window. In addition, the increase in temperature should also increase the saturation concentration of the Fe^{3+} ions in the redox catholyte which would also increase the theoretical Nernst potential of the system as seen in Figure 6.9. Furthermore, the conductivity of the electrolyte also increases with temperature (see section 6.2.8, Figure 6.20, p 108) and thus resistance losses associated with both the iron catholyte and the acid electrolyte will be reduced. Elevated temperatures also provide benefits on the anode side of the fuel cell. Carbon dioxide and carbon monoxide poisoning of the Pt electro-catalyst is reduced with increasing temperatures. This allows for not only impure hydrogen to be utilized but also other fuels such as methanol or ethanol to be used.

6.2.4 Effect of 3-D Cathode Thickness

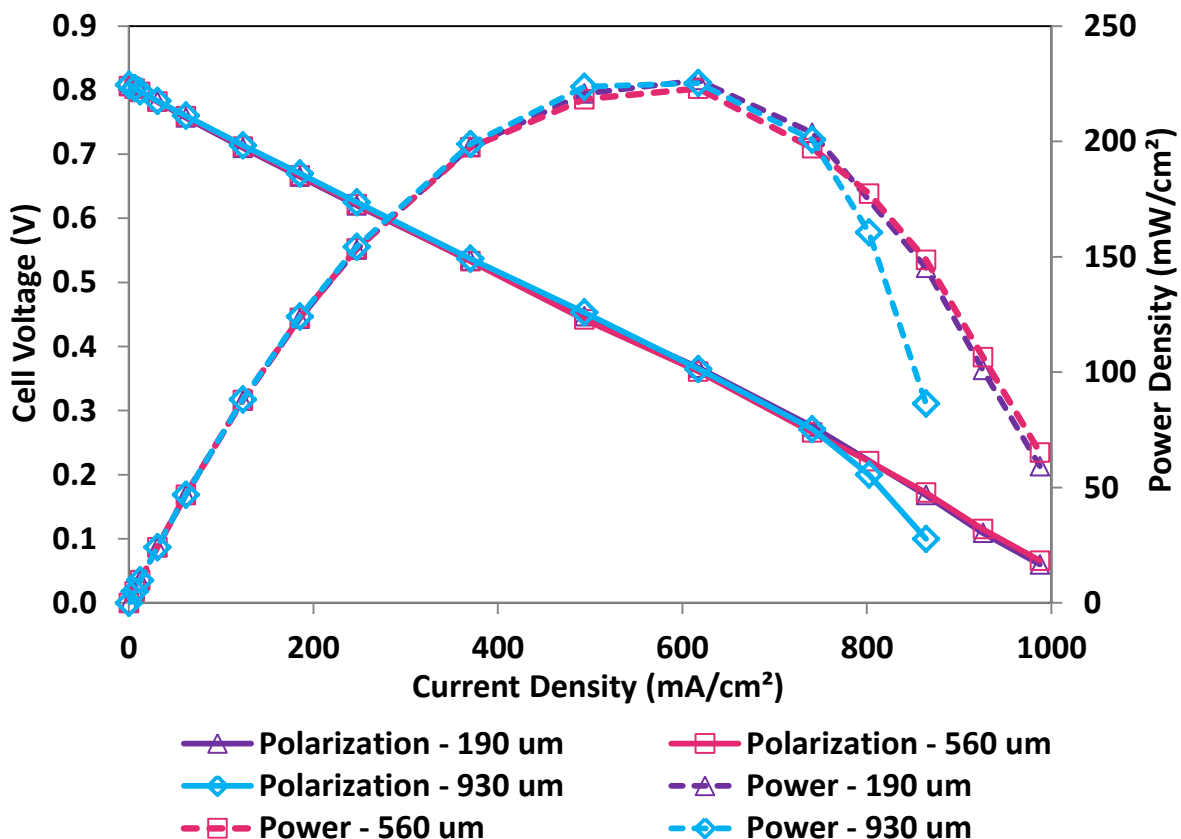


Figure 6.10: Effect of 3-D cathode thickness on fuel cell performance at 60°C.

Bladder Pressure: 20 psi, Anode: 0.2 mg/cm² 20% Pt/C (30% Nafion®), 1 mg/cm² C sublayer (20% PTFE) on Toray TGP-H-090 20% WP, Cathode: Sigracet 25 DA GDL, Toray TGP-H-120 no WP, 1 mg/cm² C MPL (15% Nafion®) on TGP-H-090 no WP, Catholyte: 6 ml/min, 2 M Fe(ClO₄)₃, 0.22 M Fe(ClO₄)₂, 0.2 M HClO₄, Fuel: 105 ml/min non-humidified hydrogen at line pressure of 30 psi, Electrolyte in spacer: 0.5 M HClO₄.

Figure 6.10 shows the effect of 3-D cathode thickness on fuel cell performance at a catholyte flow rate of 6 ml/min and 30 psi hydrogen at 105 ml/min. Here electrode thickness was manipulated by changing the number of layers from 0-2 of the non-WP BASF TGP-H-120 CFP sandwiched between the SIGRACET 25 DA GDL and 1 mg/cm² C MPL on non-WP TGP-H-090 GDL. Surprisingly fuel cell performance was not significantly affected by increasing the thickness of the 3-D cathode as identical fuel cell performance was observed for the 190 μm and 560 μm 3-D cathodes while the 930 μm 3-D cathode only lost

performance at current densities beyond those of peak power in the mass transport region. However, it is important to note here that losses in performance for the 930 μm 3-D cathode are not necessarily due to mass transport of the fuel or proton diffusion through the acidic liquid electrolyte in the gap. Were mass transport responsible for this loss in performance then a similar trend would be observed for the thinner 560 μm 3-D cathode and higher current densities achieved with both the 190 μm and 560 μm cathodes would not be possible. Furthermore, the fuel cell is being operated at stoichiometry of the catholyte in excess of 6 at 800 mA/cm^2 and so mass transport limitations at the cathode should not be an issue. Instead one may speculate that this loss in performance is related to 3-D cathode utilization and internal cell resistance.

Figure 6.11 offers a schematic to better explain this behaviour. Earlier we discussed in detail the development of a concentration gradient across the thickness of the 3-D cathode. This concentration gradient is a function of several factors including iron redox electrolyte concentration, reactant consumption rate (related to current by Faraday's law; $N = I/nF$) and the thickness of the electrode. When a thinner electrode is used it is likely that the entire thickness of the electrode would be utilized even if iron redox electrolyte crossover is not eliminated due to incomplete reactant utilization. However, as the thickness of the 3-D cathode is increased more complete reactant utilization would be observed until all of the reactant has been consumed. Taking this further to excessively thick 3-D cathodes one would expect that the redox electrolyte would have been consumed much before the 3-D cathode/liquid acidic electrolyte interface resulting in some of the 3-D cathode not being utilized. This unutilized thickness of the 3-D cathode contributes to ionic resistance in the fuel cell due to increased resistance to diffusion of the ions required to ensure charge

balance. As the load on the fuel cell is increased the thickness of the 3-D cathode required to ensure complete reactant consumption decreases resulting in more of the 3-D cathode being unutilized leading to increased ionic resistance with each subsequent increase in current being drawn. This increased ohmic overpotentials with subsequent increases in current leads to the appearance of a perceived mass transport region, i.e., not only is ‘ i ’ changing but also ‘ R ’, resulting in a non-linear iR loss. This is likely the reason for the loss in performance observed with the 930 μm 3-D cathode but not with the thinner 190 μm and 560 μm 3-D cathode which had identical fuel cell performance.

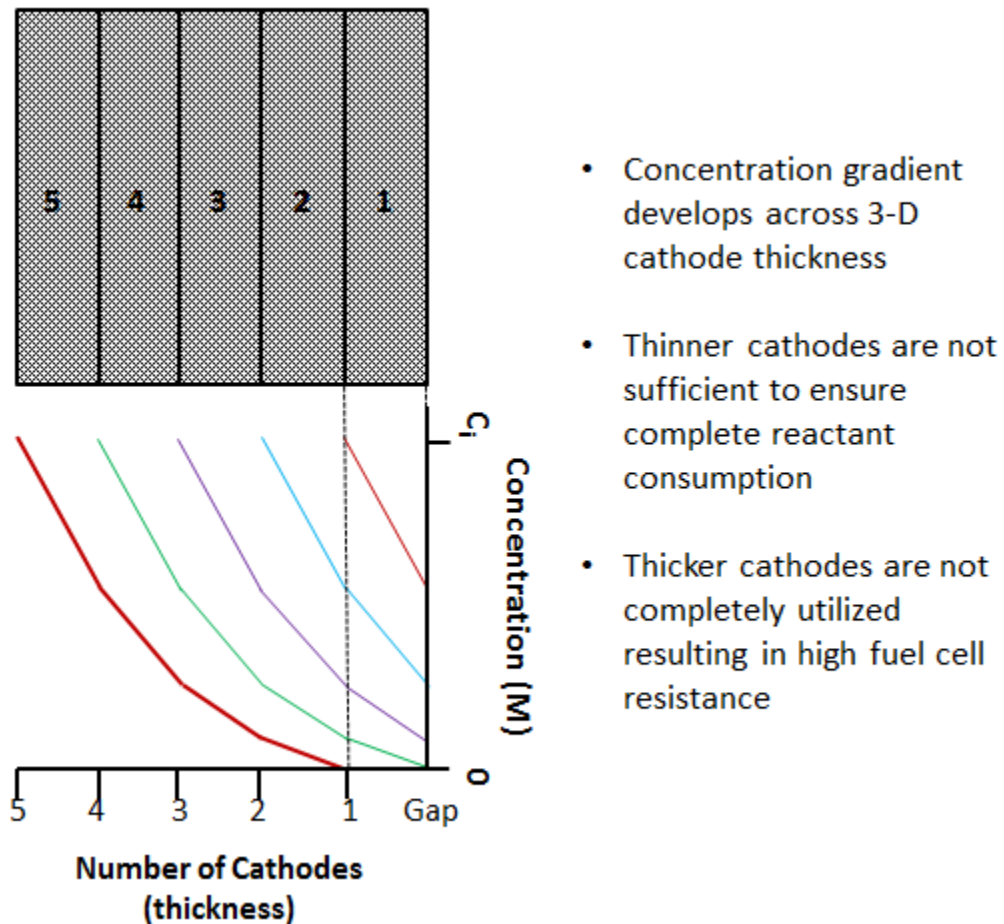


Figure 6.11: Schematic explanation of unutilized 3-D cathode contributing to fuel cell resistance with increasing current density.

6.2.5 Membraneless DHRFC vs. Conventional MEA DHRFC

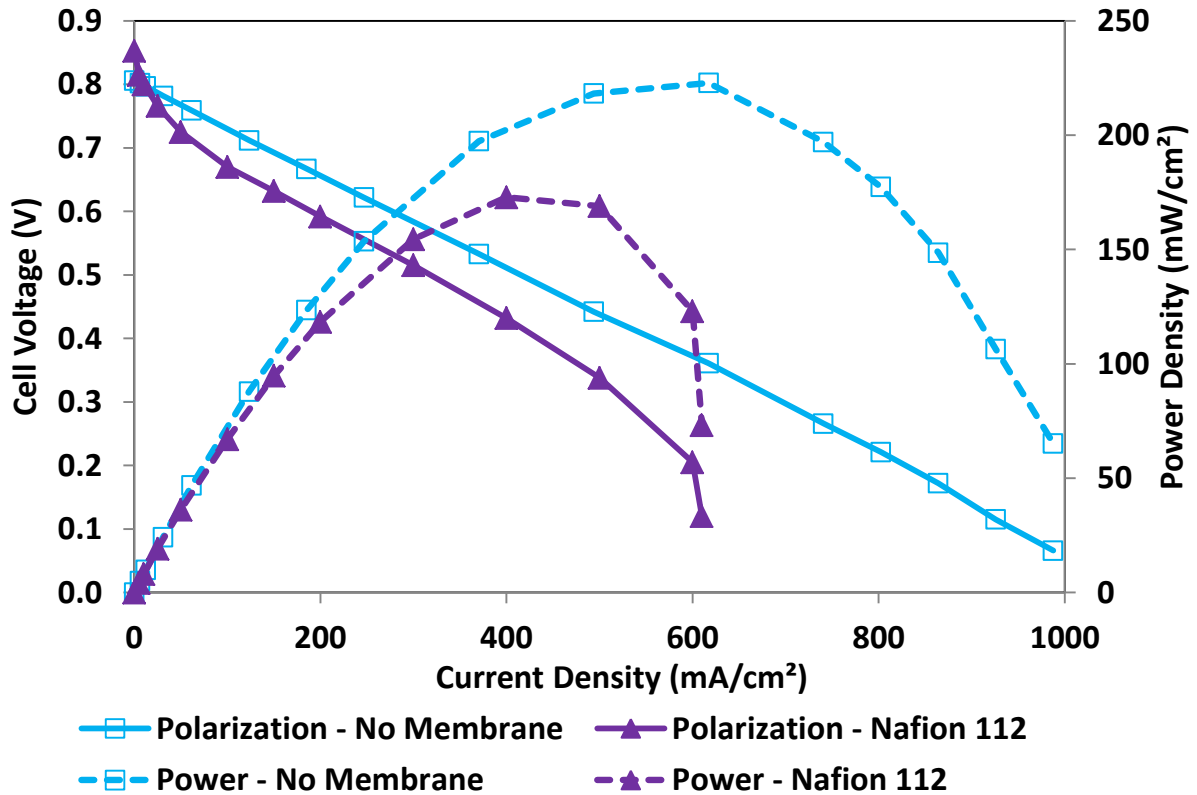


Figure 6.12: Comparison of fuel cell performance with the same electrode architectures with and without a Nafion 112 membrane at 60°C.

Bladder Pressure: 20 psi, Anode: 0.2 mg/cm² 20% Pt/C (30% Nafion®), 1 mg/cm² C sublayer (20% PTFE) on Toray TGP-H-090 20% WP, Cathode: Sigracet 25 DA GDL, Toray TGP-H-120 no WP, 1 mg/cm² C MPL (15% Nafion®) on TGP-H-090 no WP, Catholyte: 6 ml/min, 2 M Fe(ClO₄)₃, 0.22 M Fe(ClO₄)₂, 0.2 M HClO₄, Fuel: 105 ml/min non-humidified hydrogen at 30 psi, Electrolyte in spacer: 0.5 M HClO₄.

Shown in Figure 6.12 is a comparison of the DHRFC with a Nafion® 112 membrane and the membraneless electrode assembly. Fuel cell operation conditions may be found in the caption for Figure 6.12. It is apparent that the membraneless DHRFC had a lower OCV and an absence of a clear activation region (< 35 mA/cm²). The lowered OCV for the membrane-less DHRFC is due to catholyte crossover while differences in the activation region are more complex. For the Nafion® 112 DHRFC the hydrogen oxidation reaction (HOR) is limiting as would be expected by the HOR exchange current density on Pt, ~10⁻³

A/cm² [74], at least an order of magnitude lower than that of the ferric reduction reaction on carbon, $\sim 10^{-2}$ A/cm². However, the performance for the HOR is superior in the case for the membraneless DHRFC and it does not appear to be limiting. This is because the HOR in the membrane case is limited only to the triple phase sites (TPS) present in the thin film at the anode catalyst/Nafion® 112 interface that are sufficiently hydrated and the whole catalyst layer is not utilized. In the membraneless case there is better hydration of the anode catalyst layer due to contact with the liquid electrolyte. When a non-humidified fuel is used drying of the ionomer present in the catalyst layer particularly for the membrane case leads to an even lower amount of TPS leading to increased activation overpotentials. A low number of active TPS is one of the reasons that can lead to increased activation overpotentials.

One way to increase the number of TPS that are available is humidification of the gaseous fuel. Humidifying the hydrogen fuel stream improves hydration of the membrane and ionomer in the catalyst layer which in turn improves ionic contact into the catalyst layer. This allows for an extension of the reaction zone into the catalyst layer and increases the number of TPS that are available. This should improve performance of the Nafion® 112 DHRFC in the activation region. This can be seen in Figure 6.13 by comparing the humidified and non-humidified Nafion® 112 DHRFC in the activation region. Figure 6.13 shows the Nafion® 112 DHRFC performance in the activation region is limited by the HOR being limited to the anode/Nafion® 112 interface with the entire catalyst layer in the anode not being utilized resulting in the appearance of a clear activation region but with a clear improvement for the humidified hydrogen fuel.

Nafion® 112 DHRFC performance in the ohmic region is also improved by humidification. This is a result of improved hydration of the membrane which improves the

PEM's conductivity (see equation 1.39 on page 21). Furthermore, an increase in the number of TPS due to humidification also extends the mass transport region allowing for higher current densities to be achieved with the Nafion® 112 DHRFC.

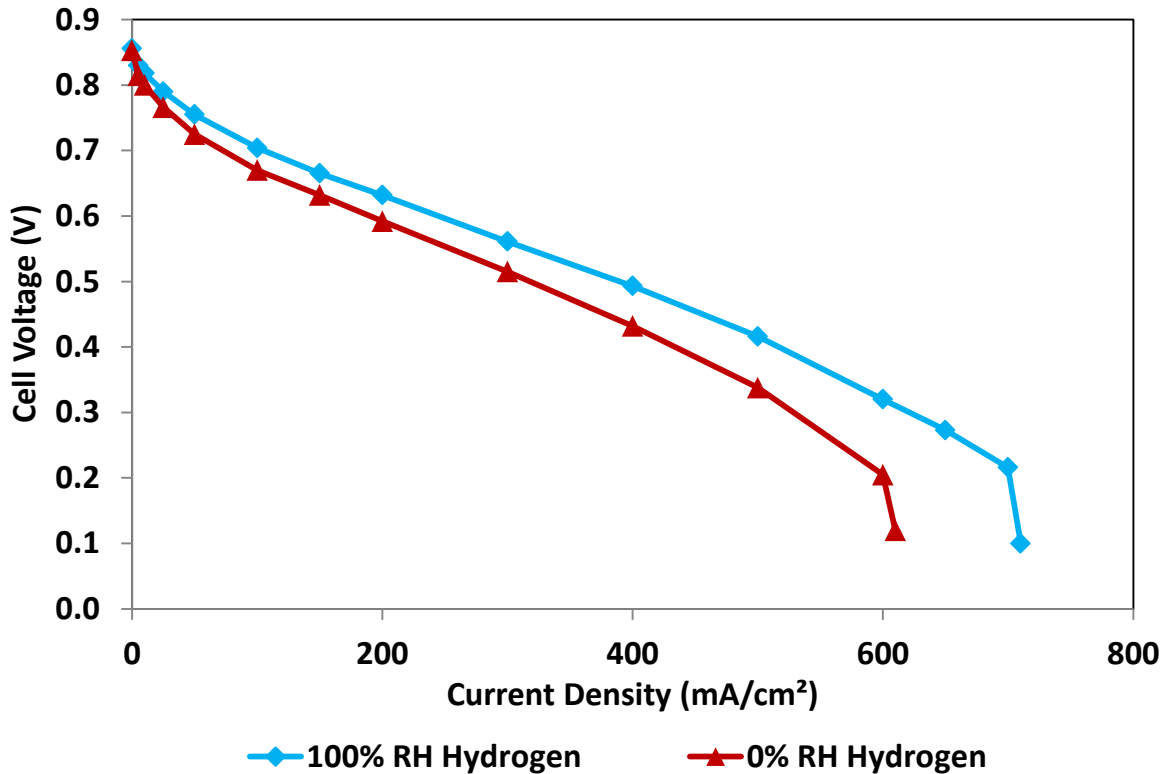
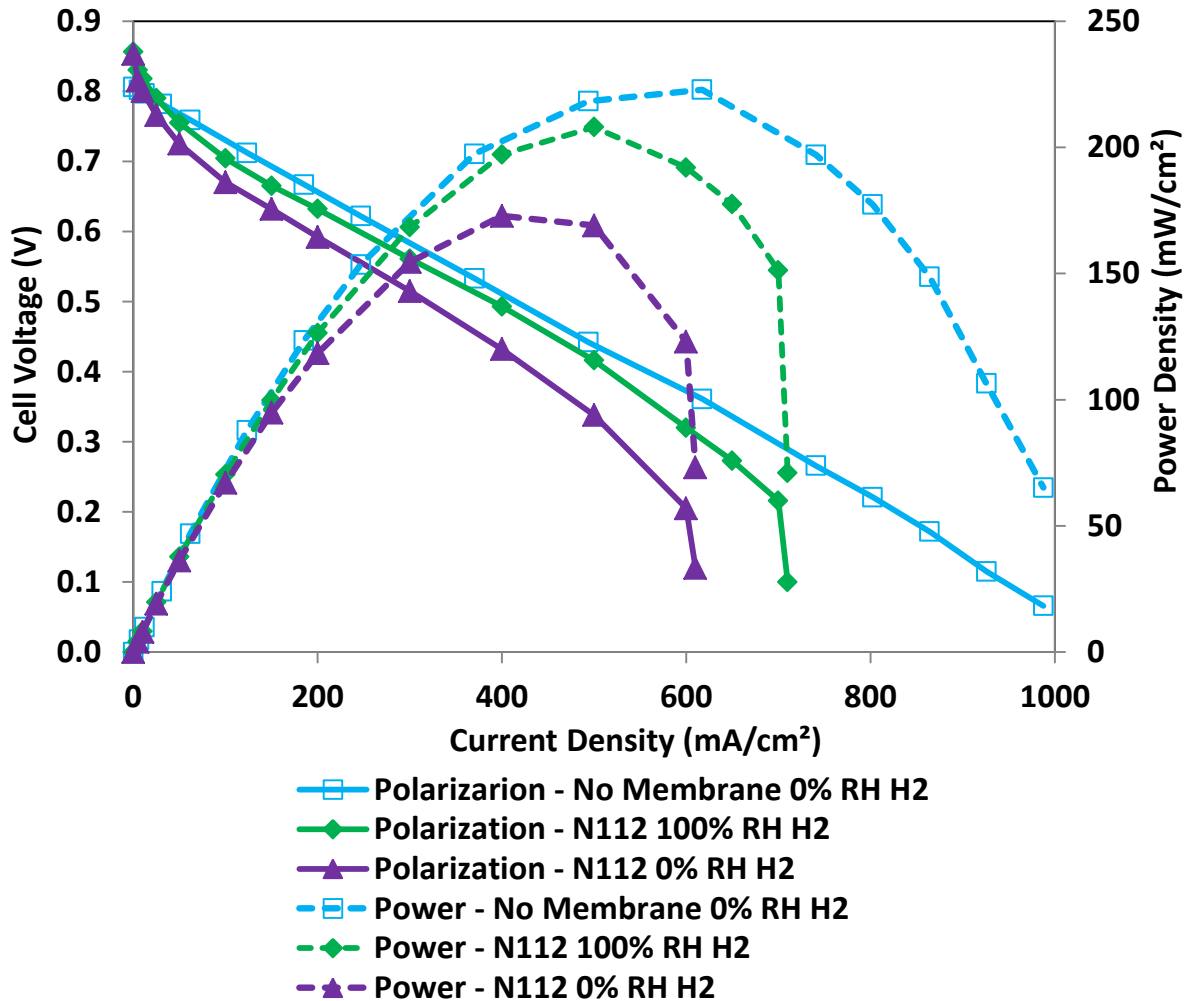


Figure 6.13: Polarization curves of the Nafion® 112 DHRFC with and without a humidified hydrogen fuel.

Temperature: 60°C, Bladder Pressure: 20 psi, Anode: 0.2 mg/cm² 20% Pt/C (30% Nafion®), 1 mg/cm² C sublayer (20% PTFE) on Toray TGP-H-090 20% WP, Cathode: Sigracet 25 DA GDL, Toray TGP-H-120 no WP, 1 mg/cm² C MPL (15% Nafion®) on TGP-H-090 no WP, Catholyte: 6 ml/min, 2 M Fe(ClO₄)₃, 0.22 M Fe(ClO₄)₂, 0.2 M HClO₄, Fuel: 105 ml/min non-humidified/humidified hydrogen at 30 psi.

Figure 6.14 shows a comparison of the non-humidified hydrogen membraneless DHRFC with humidified and non-humidified hydrogen fuel Nafion® 112 DHRFC. Relative losses in the activation region for the membraneless DHRFC are lower than the Nafion® 112 DHRFC even with a humidified fuel indicating that a significantly larger number of TPS are available at the anode in the membraneless case.



6.14: Comparison of polarization curves of the non-humidified fuel membraneless DHRFC with a humidified and non-humidified fuel Nafion® 112 DHRFC.

Temperature: 60°C, Bladder Pressure: 20 psi, Anode: 0.2 mg/cm² 20% Pt/C (30% Nafion®), 1 mg/cm² C sublayer (20% PTFE) on Toray TGP-H-090 20% WP, Cathode: Sigracet 25 DA GDL, Toray TGP-H-120 no WP, 1 mg/cm² C MPL (15% Nafion®) on TGP-H-090 no WP, Catholyte: 6 ml/min, 2 M Fe(ClO₄)₃, 0.22 M Fe(ClO₄)₂, 0.2 M HClO₄, Fuel: 105 ml/min non-humidified/humidified hydrogen at 30 psi, Electrolyte in spacer for membraneless case: 0.5 M HClO₄.

Fuel cell performance in the ohmic region for the membraneless DHRFC is slightly better to that of the Nafion® 112 DHRFC with non-humidified hydrogen as seen in the slopes of the polarization curves and the measured resistivity of the two electrode assemblies. The resistivity for the non-humidified Nafion® 112 electrode assemblies was measured to be ~100 Ωcm. The membraneless electrode assembly resistivity was measured

to be $\sim 4 \Omega\text{cm}$. This resulted in a relatively minor difference in performance in the ohmic region; the different gap thickness between the electrodes in the membraneless DHRFC (0.067 cm) and the Nafion® 112 DHRFC (0.00508 cm) lead to similar overall resistance. This is due to drying of the Nafion® 112 membrane with non-humidified fuel leading to increased ohmic losses. For the membraneless DHRFC with no hydrogen humidification the absence of the membrane means that its hydration is not a factor. In comparison with the Nafion® 112 DHRFC with humidified hydrogen the membraneless DHRFC with no hydrogen humidification has only marginally increased ohmic losses. Humidification of the fuel allows for better hydration of the Nafion® 112 membrane and thus improved performance; the measured resistivity of $\sim 50 \Omega\text{cm}$ with humidification leads (compared to $\sim 100 \Omega\text{cm}$ for no humidification) to a lower slope in the ohmic region for the Nafion® 112 DHRFC. The low resistivity of the membraneless architecture compared to Nafion® 112 should allow for improvements in overall fuel cell resistance to be achieved by a reduction in gap thickness. It is expected that optimization of the electrodes, electrolyte composition, component materials and design, and operating conditions will result in further improvement of the performance of the membrane-less DHRFC.

It is also evident that the membrane-less fuel cell is under ohmic control and does not become mass transport limited while the PEM-based architecture enters the mass transport regime at a much lower current density. This is once again likely due to the lower number of TPS present in the Nafion® 112 DHRFC leading to the HOR not being able to produce protons at a rate fast enough to meet the charge balance requirements at the cathode even though the fuel cell is being operated at hydrogen stoichiometry in excess of 5 at 600 mA/cm^2 . Humidification of the fuel increases the number of TPS sites present but the HOR

is still limiting even at stoichiometry in excess of 4 at 700 mA/cm². On the other hand, the improved wetting and thus utilization of the anode catalyst by the liquid acid electrolyte in the membraneless DHRFC ensures the HOR is not mass transport limited. In addition the high stoichiometry of the catholyte ($\lambda > 6$) at this fixed flow rate prevents the ferric reduction reaction from becoming mass transport limited. With neither the anode nor the cathode mass transport limited the fuel cell remains under ohmic control at these conditions.

Improved performance in the activation region (lower relative kinetic losses) and increased utilization of the catalyst allow for improved performance of the membraneless DHRFC compared to the Nafion® 112 DHRFC. The improved catalyst utilization by the liquid acid electrolyte should allow for further reduction of the already low PGM loadings for the anode.

6.2.6 Low Precious Metal Content Membraneless DHRFC

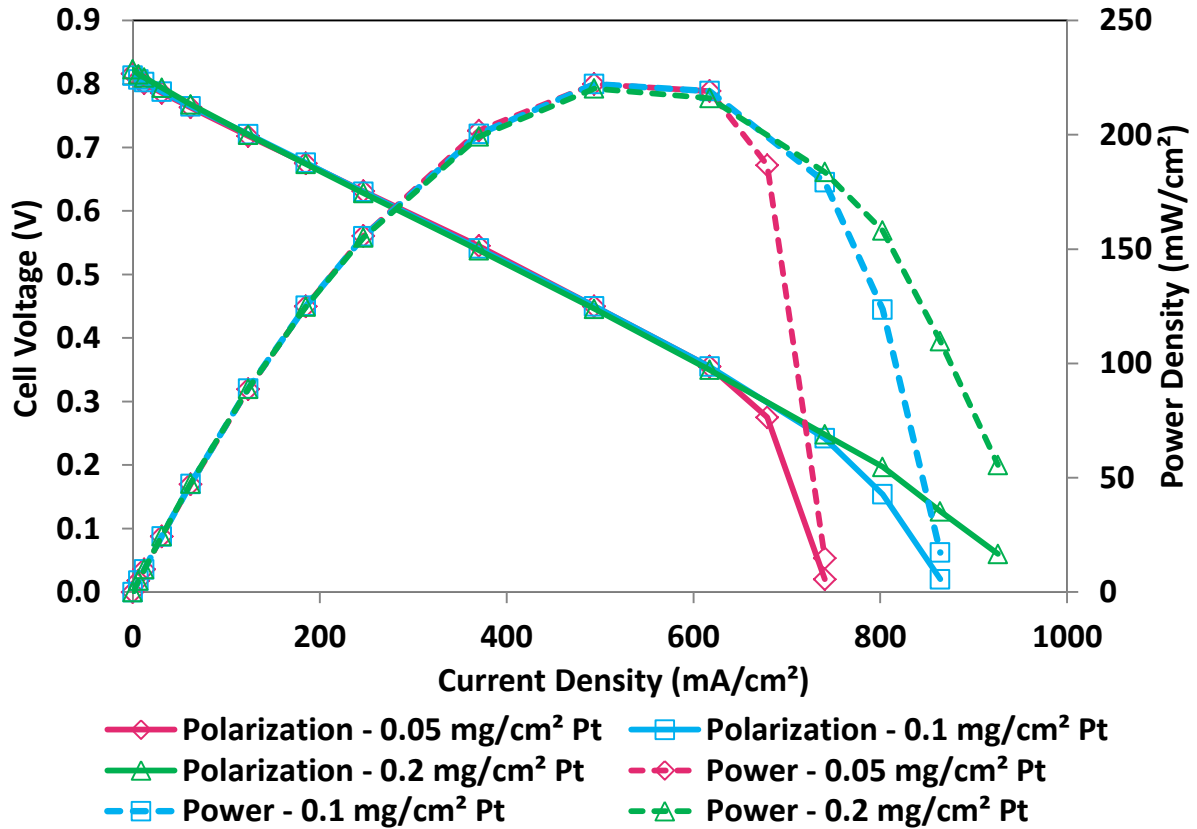


Figure 6.15: Effect of anode Pt catalyst content on fuel cell performance at 60°C.

Bladder Pressure: 20 psi, Anode: X mg/cm² 20% Pt/C (30% Nafion®), 1 mg/cm² C sublayer (20% PTFE) on Toray TGP-H-090 20% WP, Cathode: Sigracet 25 DA GDL, Toray TGP-H-120 no WP, 1 mg/cm² C MPL (15% Nafion®) on TGP-H-090 no WP, Catholyte: 4 ml/min, 2 M Fe(ClO₄)₃, 0.22 M Fe(ClO₄)₂, 0.2 M HClO₄, Fuel: 105 ml/min non-humidified hydrogen at line pressure of 30 psi, Electrolyte in spacer: 0.5 M HClO₄.

Figure 6.15 shows results for the operation of the membrane-less DHRFC at 60°C, 30 psi hydrogen with fuel and oxidant flow rates of 105 ml/min and 4 ml/min, respectively, with different anode Pt loadings while the cathode is PGM free as described earlier.

Fuel cell performance in the activation and ohmic regions was not affected by reducing the Pt loading of the anode from 0.2 mg/cm² to 0.05 mg/cm². This demonstrates the effectiveness of using the liquid acid electrolyte (0.5 M HClO₄ in this case) in utilizing the anode catalyst layer and providing sufficient access to the TPS. However, at higher current

densities an increased mass transport region appears for the lower Pt loading anodes. The increased mass transport overpotentials with lower anode loading is likely due to less active triple phase sites resulting in the hydrogen oxidation reaction (HOR) becoming more mass transport limited. At higher current densities the available TPS are not sufficient to supply the protons at a rate fast enough to ensure charge balance at the cathode to keep the fuel cell only under ohmic control. Although the liquid acid electrolyte significantly improves anode Pt-catalyst utilization by increasing the number of TPS present compared to the membrane case there is still catalyst that is not utilized. The use of non-humidified hydrogen is likely contributing to this issue. This hypothesis can be easily proven by humidifying the hydrogen fuel which should extend the mass transport region and improve the ohmic losses.

6.2.7 Effect of Humidification on Membraneless DHRFC

Figure 6.16 shows a comparison of the humidified and non-humidified hydrogen fuel membraneless DHRFC. Figure 6.16b shows the kinetic region ($< 35 \text{ mA/cm}^2$) of Figure 6.16a. It can be seen that a correlation between OCV and humidification of the hydrogen fuel is not readily apparent. The relatively minor differences in OCV can be regarded as statistically irrelevant and attributed to test reproducibility. However, relative losses in the kinetic region are smaller for the humidified hydrogen fuel. At a current density of 0-32 mA/cm^2 shown in Figure 6.16b, both cases of the non-humidified hydrogen membraneless DHRFC lose approximately 28-30 mV while losses for both of the humidified cases are approximately 23-25 mV. From this it may be concluded that humidification of the hydrogen fuel provides some improvement of activation by increasing the number of TPS present.

Humidification of the hydrogen fuel also improved fuel cell performance in the ohmic region which is apparent in the divergent humidified and non-humidified membraneless DHRFC polarization curves. Further evidence of the reduced ohmic losses is observed in the measured resistance of the humidified and non-humidified membraneless electrode assemblies which can be seen in Table 6.3 along with the ohmic loss associated with the difference in resistance between the two cases and the actual measured difference in voltage for different current densities. This improvement for the humidified hydrogen membraneless DHRFC is likely due to improved conductivity due to improved hydration of the ionomer in the anode catalyst layer.

Humidification of the hydrogen fuel increases the number of active anode TPS compared to the non-humidified hydrogen which should also extend the mass transport region. For the non-humidified hydrogen membraneless DHRFC the mass transport region

was reached earlier with each consecutive halving of the anode Pt-catalyst loadings. However, for the humidified hydrogen membraneless DHRFC the mass transport region was extended compared to the non-humidified hydrogen membraneless DHRFC and current densities in excess of 1000 mA/cm² were reached even with the 0.05 mg/cm² Pt anode. On the other hand current densities beyond 710 mA/cm² were not possible with a non-humidified hydrogen fuel with the 0.05 mg/cm² Pt anode. In addition, a significant difference in the mass transport regime between the humidified hydrogen 0.05 mg/cm² and 0.20 mg/cm² Pt anodes was not observed. This result indicates that 0.05 mg/cm² of Pt is enough to sustain the fuel cell performance achieved with the higher Pt anode loadings. Maximum power densities for the humidified hydrogen membraneless DHRFC and non-humidified hydrogen membraneless DHRFC of 250 mW/cm² and 220 mW/cm², respectively, were achieved with the 0.05 mg/cm² Pt anode.

Table 6.3: Effect of humidification on resistance and associated ohmic losses at different current densities.

	Non-humidified Hydrogen	Humidified Hydrogen
Resistance (Ω)	0.09	0.07
Ohmic loss at 250 mA/cm ² (mV)	72.9	56.7
Ohmic loss at 500 mA/cm ² (mV)	145.8	113.4

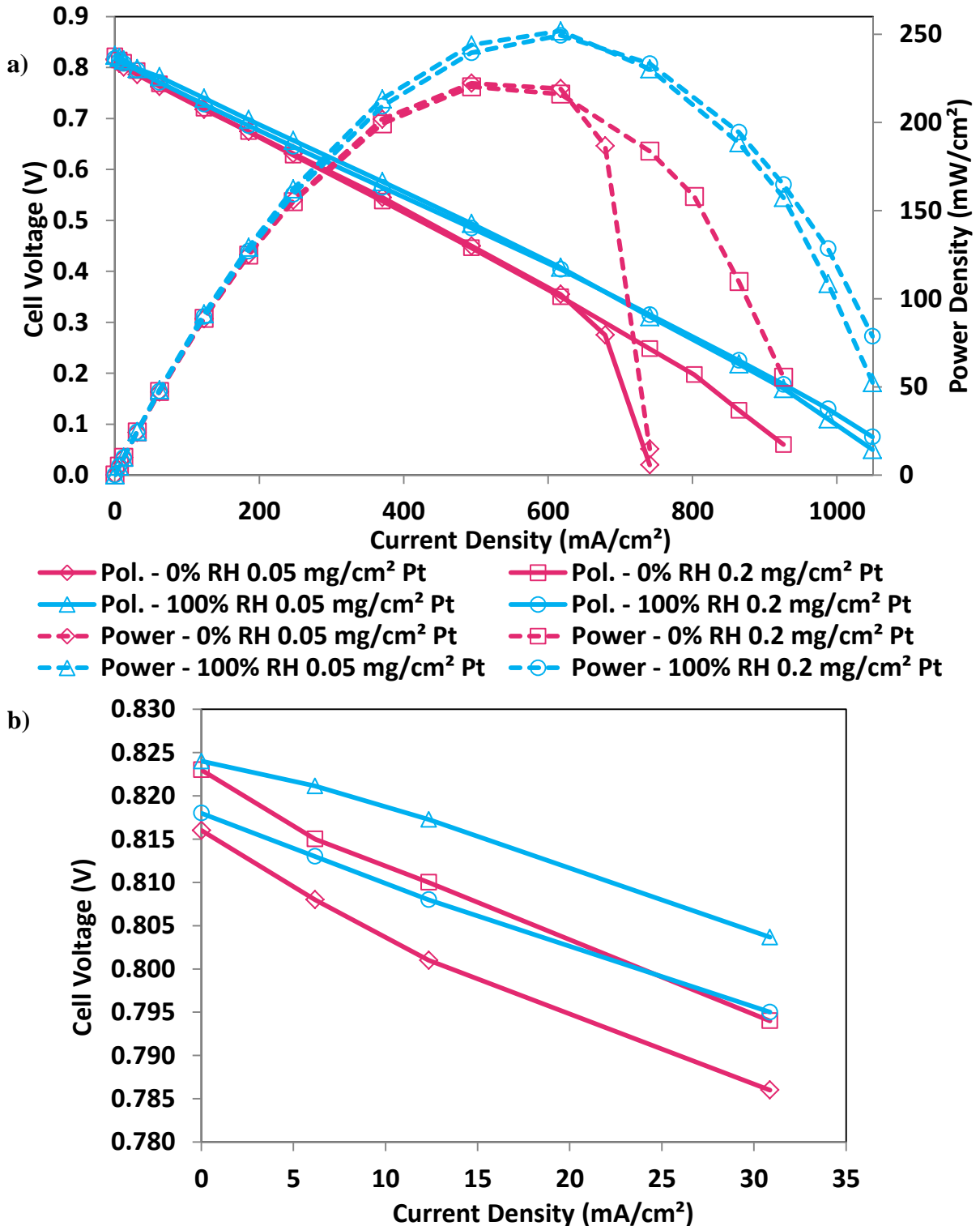


Figure 6.16: Effect of hydrogen fuel humidification on fuel cell performance for different anodes at 60°C. a) Polarization and power density curves. b) Close up of activation region.

Bladder Pressure: 20 psi, Anode: X mg/cm² 20% Pt/C (30% Nafion®), 1 mg/cm² C sublayer (20% PTFE) on Toray TGP-H-090 20% WP, Cathode: Sigracet 25 DA GDL, Toray TGP-H-120 no WP, 1 mg/cm² C MPL (15% Nafion®) on TGP-H-090 no WP, Catholyte: 4 ml/min, 2 M Fe(ClO₄)₃, 0.22 M Fe(ClO₄)₂, 0.2 M HClO₄, Fuel: 105 ml/min non-humidified/humidified hydrogen at 30 psi, Electrolyte in spacer: 0.5 M HClO₄.

6.2.8 Fuel Cell Resistance

Figure 6.17 shows the effect of compression bladder pressure used for sealing on cell resistance and cell voltage at 200 mA/cm² and 400 mA/cm². Cell resistance improves with an increase in compression pressure as contact between the electrodes and the flow field plates are improved. At around 20 psi cell resistance did not further decrease with an increase in pressure as contact resistance could no longer be lowered. In the pressure range tested fuel cell voltage was not significantly affected but a slight optimum occurs around a sealing pressure of 25 psi. However, at sealing pressures higher than 20 psi fuel cell reproducibility due to electrode bowing suffers. A fuel cell operational pressure of 20 psi was chosen for fuel cell testing based on these results.

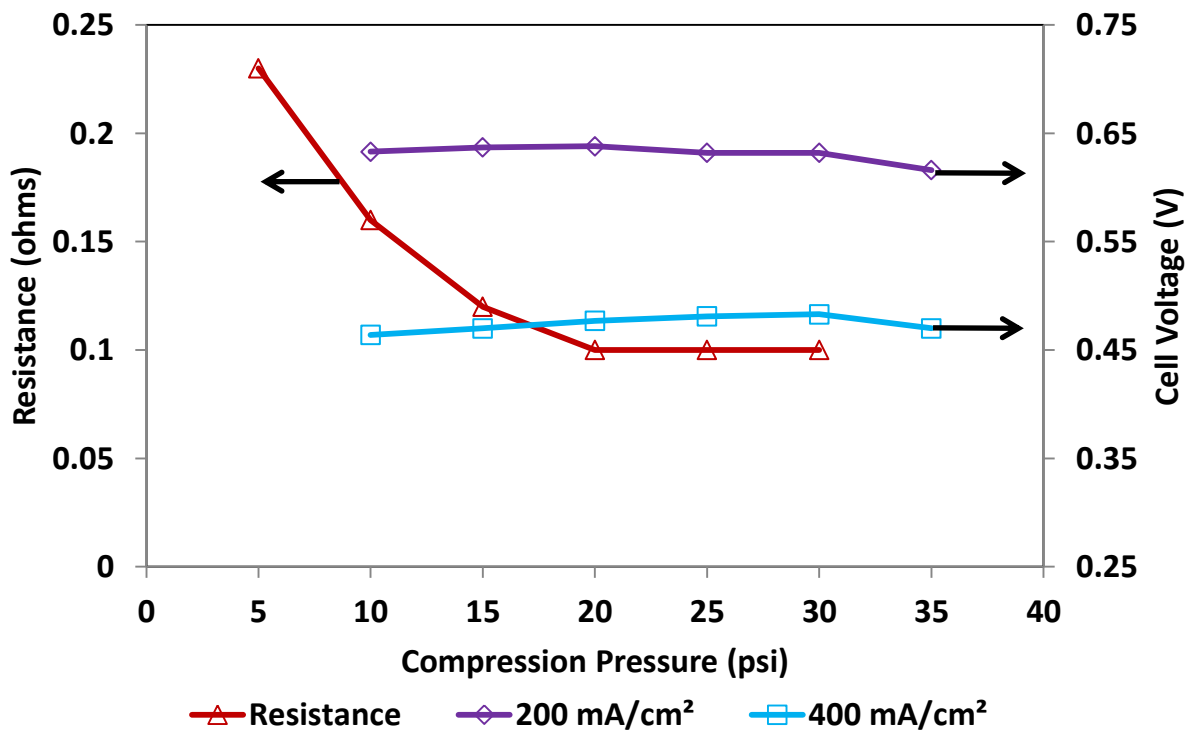


Figure 6.17: Membraneless DHRFC resistance and voltage as a function of bladder pressure using the membraneless electrode assembly with a 3.24 cm² square open-spacer with a catholyte and flow rate of 6 ml/min 2 M Fe(ClO₄)₃ and a fuel flow rate of 105 ml/min non-humidified hydrogen.

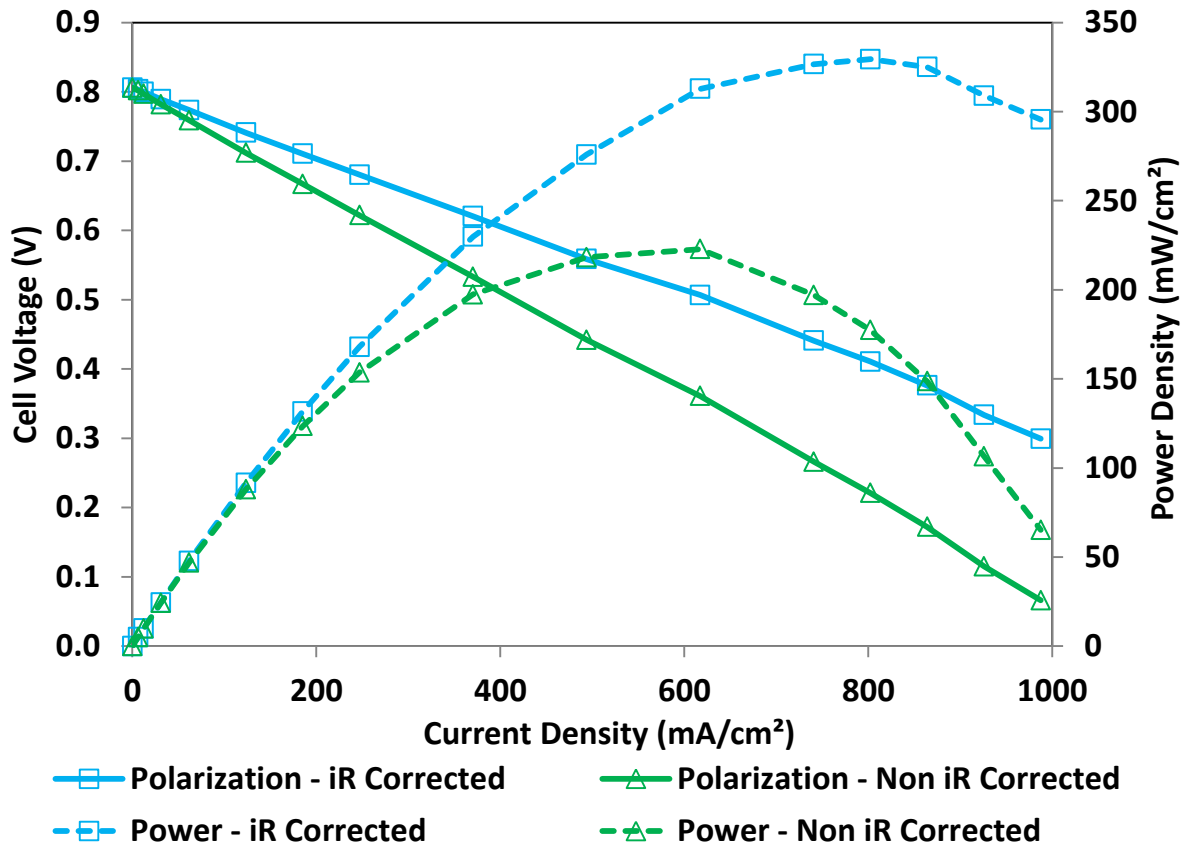


Figure 6.18: Comparison of iR-corrected and non-iR corrected fuel cell performance curves at 60°C.

Bladder Pressure: 20 psi, Anode: 0.2 mg/cm² 20% Pt/C (30% Nafion®), 1 mg/cm² C sublayer (20% PTFE) on Toray TGP-H-090 20% WP, Cathode: Sigracet 25 DA GDL, Toray TGP-H-120 no WP, 1 mg/cm² C MPL (15% Nafion®) on TGP-H-090 no WP, Catholyte: 6 ml/min, 2 M Fe(ClO₄)₃, 0.22 M Fe(ClO₄)₂, 0.2 M HClO₄, Fuel: 105 ml/min non-humidified hydrogen at 30 psi, Electrolyte in spacer: 0.5 M HClO₄.

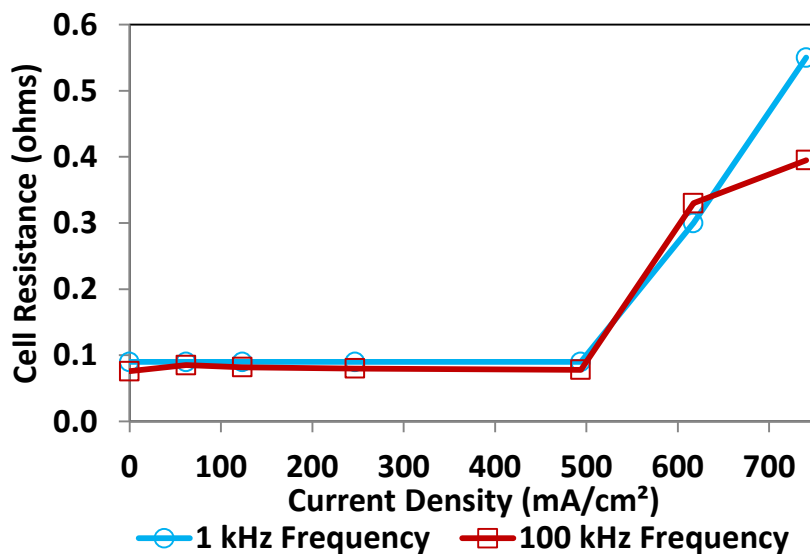


Figure 6.19: Membraneless DHRFC resistance as a function of LCR meter frequency with a catholyte and flow rate of 6 ml/min 2 M Fe(ClO₄)₃ and a fuel flow rate of 105 ml/min non-humidified hydrogen.

Figure 6.18 shows the effect of iR corrections on fuel cell performance for the conditions shown. Similar differences in iR corrected and non-iR corrected curves were observed for other conditions. Resistance corrected polarization curves for all fuel cell polarization curves shown in this thesis may be found in Appendix C. Overall fuel cell resistance was measured at OCV and 1 kHz using an LCR meter and determined to be $0.09 \pm 0.01 \Omega$ under the conditions shown in Figure 6.18. The LCR meter measures both the resistance and capacitance but when only one of these is required the correct A.C. frequency of the LCR meter must be used. For resistance measurements very high frequencies are recommended and vice versa for capacitance. At higher frequencies the resistance of the cell does not change much indicating that only cell resistance is being measured. Figure 6.19 shows that an LCR frequency greater or equal to 1 kHz is sufficient to measure the resistance of the cell under load as the observed difference in cell resistance at different current densities is minimal between 1 kHz and 100 kHz.

It is evident from the iR-corrected and non-iR-corrected polarization curves in Figure 6.18 that the fuel cell is under severe ohmic control and suffers from large ohmic overpotentials. In comparison to a conventional membrane electrode assembly (Gore CCM 0.4 mg/cm² 20% Pt/C on both side of Nafion® 115) under similar conditions in the same cell the fuel cell resistance for the DHRFC is similar to that of the GORE CCM (~0.06 Ω). On the other hand the resistance for the same GORE CCM in a different cell (5 cm²) was measured to be ~0.005 Ω which is at least an order of magnitude lower. As there is no membrane or triple phase boundary constraint and the liquid acidic electrolyte provides enhanced ionic conductivity throughout the electrode poor contact resistance between the electrolyte and the electrode is likely not a contributing factor to high fuel cell resistance. Measurement of the

contact resistance between in the cell was performed using the LCR meter at 1kHz. For this test the fuel cell was set-up as normal but with no electrolytes flowing and the electrical circuit between the electrodes completed with aluminium foil. The resistance of this circuit is then essentially just the contact between the current collectors and the flow field plates and the flow field plates and the electrodes. This contact resistance was measured to be 0.02 ohms which is extremely high in comparison to a different 5 cm² cell where the entire membrane electrode assembly resistance was measured to be 0.005 ohms. Based on the resistance, R of the cell, being proportional to resistivity and length and inversely proportional to area, one would expect the larger the cell area the smaller the resistance. This indicates that poor hardware design and contact resistance of the cell is a major contributor to the large ohmic overpotentials observed in the polarization curves. It is expected that improved hardware components and design should significantly lower cell resistance and thus improve fuel cell performance.

Improvements in fuel cell resistance are likely also possible with the use of higher conductivity electrolytes. According to the Casteel-Amiss equation (see Ohmic overpotentials section, p 22) for a given temperature the conductivity of the solution has an optimum based on the concentration of the solution. The Casteel-Amiss parameters for perchloric acid are not readily available but the conductivity of hydrochloric acid which has a similar acidity and nature to perchloric acid, as a function of wt.% is shown in Figure 6.20. It is observed that a maximum conductivity for the hydrochloric acid occurs at around 20 wt.% while 5 wt.% HCl has the lowest conductivity. In this work the HClO₄ liquid acid electrolyte used is ~5 wt.% and so likely not at maximum conductivity. It is expected that cell resistance

can be significantly lowered by operating at higher concentrations of the liquid acid electrolyte to optimize the conductivity of the electrolyte.

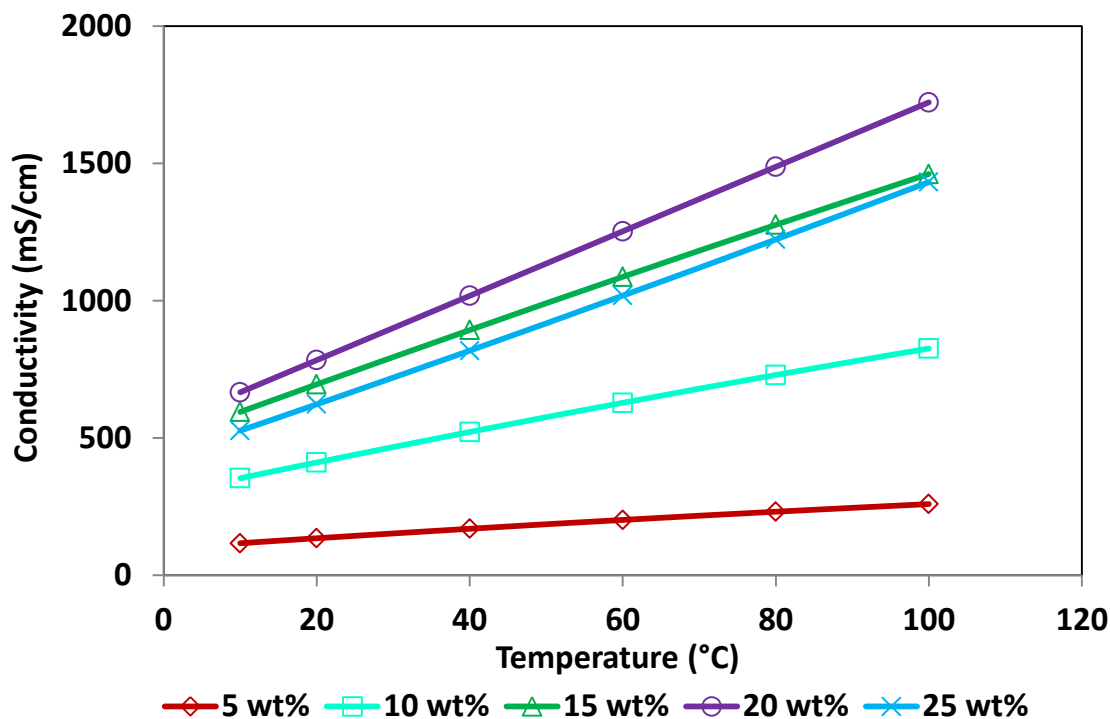


Figure 6.20: Calculated (Casteel-Amiss) conductivity of different concentrations of hydrochloric acid as a function of temperature.

Other contributions to fuel cell resistance may also include the presence of voids in the liquid acid electrolyte. These inert voids may be a result of the hydrogen gas crossing over into the liquid acid electrolyte. Both the Maxwell and Meredith-Tobias equation (see Ohmic Overpotentials section, p22) suggest that the presence of voids can reduce electrolyte conductivity. Figure 6.21 shows the effect of bubbling hydrogen (5 minutes) through the electrolyte on the measured conductivity of the 0.5 M HClO₄ solution. It was observed that bubbling hydrogen and thus providing some bubbles in the solution leads to losses in ionic conductivity of the electrolyte. It must be noted that while conductivity measurements were

performed the hydrogen was not bubbled. This would not only reduce conductivity of the solution but could also lead to reduced active area of the electrode for the reaction to occur by limiting ionic conductivity.

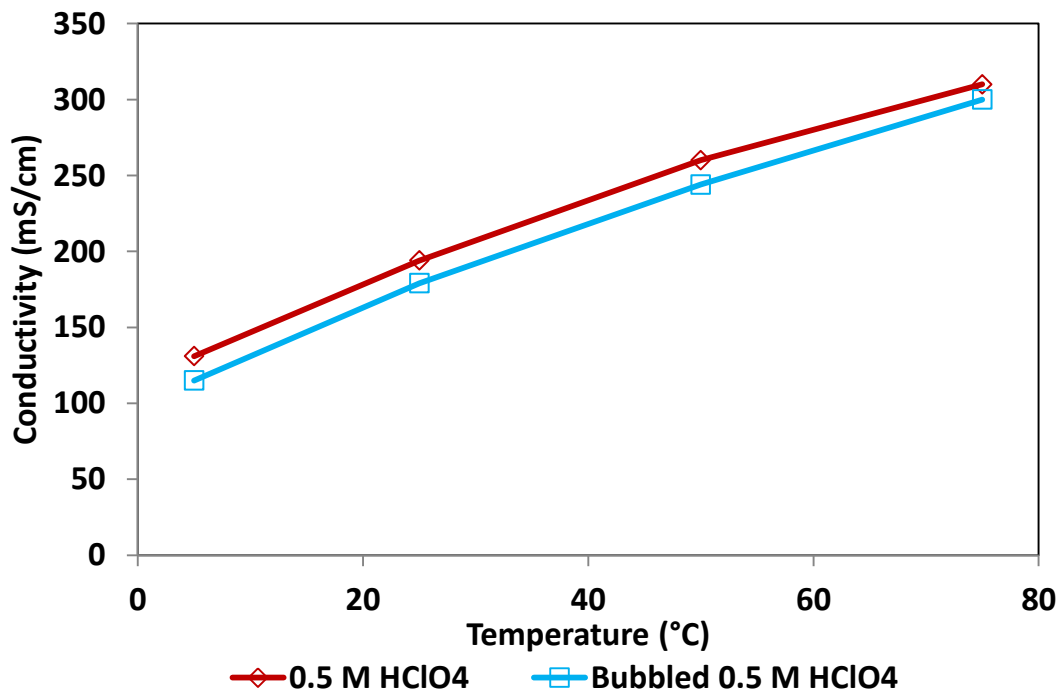


Figure 6.21: Conductivity of 0.5 M HClO₄ before bubbling with hydrogen and after bubbling with hydrogen as a function of temperature.

6.2.9 Apparent Exchange Current Density Calculations

The hydrogen anode can be treated as a reference electrode at low current densities as anode activation overpotentials are usually very low. This in combination with iR -corrections of the fuel cell polarization curves allows for calculations of the apparent exchange current density for the Fe^{3+} reduction reaction on carbon. Here, the low field approximation of the Butler-Volmer equation can be used for overpotentials less than ~ 25 mV. The Butler-Volmer equation is expanded using the Taylor-McLaurin series to express the exponential terms while the higher order terms are neglected to derive the low field approximation as follows,

$$i_o = \frac{iRT}{nF\eta_s} \quad (6.3)$$

where i_o is the exchange current density in mA/cm², i is the operating current density in mA/cm², R is the ideal gas constant in J/molK, n is the number of electrons transferred, F is Faraday's constant equal to 96485 Coulombs/mol and η_s is the overpotential in V and described by,

$$\eta_s = |(E - E_e)| \quad (6.4)$$

where E is the measured cell voltage in V and E_e is the equilibrium cell voltage in V.

Table 6.4 summarizes the calculated exchange current densities using the low field approximation for the ferric reduction reaction for different fuel cell operating conditions. The decrease in exchange current density with an increase in redox catholyte flow rate observed is likely due to crossover effects decreasing cell voltage and thus increasing the perceived overpotentials compared to the equilibrium cell voltage, i.e., error at higher flow rates is higher due to mixed potentials at the anode created by ferric crossover. A slight increase in exchange current density with temperature is also observed though this increase is

not close to the exponential increase that would be expected from equation 1.38 (Activation Overpotentials, p19). These measured values of the exchange current density are lower than those reported in the literature of approximately 10 mA/cm² for 2 M Fe(ClO₄)₃ at room temperature [62]. This is likely due to error associated with ferric ion crossover contributing to increased overpotentials and thus lower values of the exchange current.

Table 6.4: Summary of apparent exchange current densities for the ferric reduction reaction on carbon.

Catholyte Flow Rate (ml/min)	Temperature (°C)	Apparent Exchange Current Density, i_0 (mA/cm²)
2	60	4.4
4	60	4.3
6	60	4.2
Temperature (°C)	Catholyte Flow Rate (ml/min)	Apparent Exchange Current Density, i_0 (mA/cm²)
45	2	4.2
60	2	4.4
75	2	4.4

*Literature reported values: ~10 mA/cm² on C [62].

6.2.10 Comparison with Incumbent PEMFC Technology

The PEMFC and membraneless DHRFC represent two different fuel cell systems but with some similarities. However, it is nonetheless important to compare the preliminary membraneless DHRFC performance with the incumbent PEMFC technology for reflective reasons. PEMFC testing was performed with commercially available CCM (Gore®) with loadings of 0.4 mg/cm² Pt (20% Pt/C Vulcan XC 72, 30% Nafion®) on both sides of a Nafion® 115 membrane. The fuel cell was operated at an operating temperature of 60°C with hydrogen (100% RH) and air (100% RH) stoichiometry of 5 and 3, respectively. The high stoichiometry of hydrogen flow is similar to the fixed hydrogen flow rate for the membraneless DHRFC. A comparison of iR-corrected performance of the PEMFC with the membraneless DHRFC is shown in Figure 6.22. PEMFC testing was performed in a 5 cm² fuel cell.

Fuel cell voltage of the PEMFC is higher throughout the polarization curve as would be expected from the larger available potential window in a H₂/O₂ system (1.23 V) compared to the H₂/Fe³⁺ system (0.77 V). However, even at significantly lower total fuel cell catalyst loadings and non-humidified hydrogen relative losses in the activation region for the membraneless DHRFC are significantly lower compared to the PEMFC. This demonstrates the significantly improved kinetics of the membraneless DHRFC compared to the PEMFC. The PEMFC was capable of achieving significantly higher current densities (in excess of 1600 mA/cm²) due largely to the superior electrode design and better hardware. Little to no work has yet been performed on optimization of the electrolyte composition, 3-D cathode and anode for the unique challenges of the membraneless DHRFC. However, it is expected that work in this area will significantly improve fuel cell performance for the membraneless

DHRFC. Although the iR-corrected peak power density achieved of ~ 460 mW/cm² for the PEMFC in Figure 6.22 is superior to the iR-corrected non-optimized peak power density of ~ 330 mW/cm² for the membraneless DHRFC with humidified hydrogen, the results are encouraging given the cost reduction it achieves.

A comparison of different figures of merit demonstrates that the membraneless DHRFC has the ability to be extremely cost competitive with a commercial PEMFC system. In terms of $W_{\text{peak}}/\text{gPt}$ for the fuel cell system, the membraneless DHRFC (demonstrated up to 6300 $W_{\text{peak}}/\text{gPt}$) which easily outperforms the PEMFC (575 $W_{\text{peak}}/\text{gPt}$ for the 0.8 mg/cm² total Pt CCM used here; 2300 $W_{\text{peak}}/\text{gPt}$ for 0.2 mg/cm² total Pt CCM assuming the same performance). In addition, the membraneless DHRFC operates in the absence of a PEM and does not require the balance of plant components the PEMFC does for heat and water management. Though some work is required to achieve performance competitiveness on-par with the state-of-the-art PEMFC the membraneless DHRFC clearly has the potential to surpass the PEMFC in cost-competitiveness in both the stack and system categories.

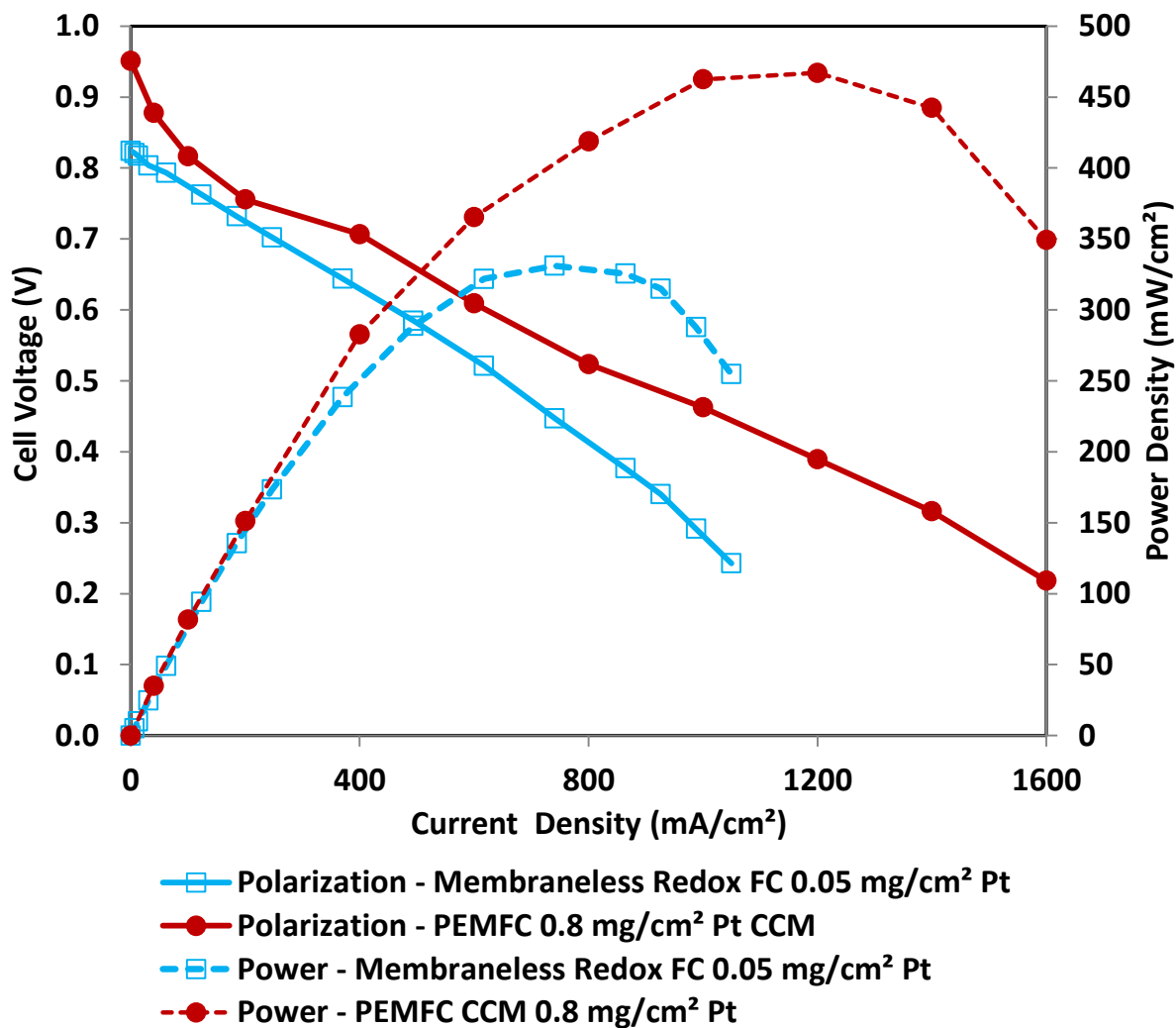


Figure 6.22: Comparison of iR-corrected DHRFC and PEMFC polarization and power density curves at 60°C.

DHRFC: Bladder Pressure: 20 psi, Anode: 0.05 mg/cm² 20% Pt/C (30% Nafion®), 1 mg/cm² C sublayer (20% PTFE) on Toray TGP-H-090 20% WP, Cathode: Sigracet 25 DA GDL 20% WP, Toray TGP-H-120 no WP, 1 mg/cm² C MPL (15% Nafion®) on TGP-H-090 no WP, Catholyte: 4 ml/min 2 M Fe(ClO₄)₃, 0.22 M Fe(ClO₄)₂, 0.2 M HClO₄, Fuel: 105 ml/min non-humidified hydrogen at line pressure of 30 psi, Electrolyte in spacer: 0.5 M HClO₄. PEMFC: MEA: Gore CCM 0.4 mg/cm² 20% Pt/C (30% Nafion®) on each side of a Nafion 115 membrane, Air 100% RH at λ = 4, Hydrogen 100% RH at λ = 5.

6.2.11 Durability Study for The Membraneless DHRFC

Initial polarization curves are useful for comparing effects of different factors on fuel cell performance and undoubtedly provide extensive amounts of information about fuel cell operation. However, they are inadequate in demonstrating a stable and durable system. Galvanostatic experiments were performed at 100 mA/cm² and 400 mA/cm² to demonstrate the stability and durability of the membraneless hydrogen redox fuel cell. Unlike the initial polarization curves where the system was operated under single pass the redox electrolyte was recirculated throughout the duration of the durability experiments to avoid wasting copious amounts of redox electrolyte. Figure 6.23 shows system durability at 60°C with 0.5 L of the 2 M Fe(ClO₄)₃, 0.22 M Fe(ClO₄)₂, 0.2 M HClO₄ catholyte recirculated at 4 ml/min and a non-humidified hydrogen flow rate of 105 ml/min. Other experimental details may be found in the figure caption.

The fuel cell was operated at 100 mA/cm² and 400 mA/cm² for 24 hours (86400 seconds) or until the system was shut-down by the multistat due to the cell voltage dropping below a safety limit of -0.6 V. The system demonstrated poor stability with high fluctuations in cell voltage over the duration of the experiment. These fluctuations are related to the high hydrogen flow rate. This was confirmed by purging the cathode with a high catholyte flow rate (> 10 ml/min). During this purging of the cathode a large amount of the bubbles were observed in the catholyte exit stream which should be only liquid. The high hydrogen flow rate results in the formation of hydrogen bubbles in the liquid acidic electrolyte which travel to the cathode. Once at the cathode due to the discrete layer stacking design these bubbles get trapped resulting in either lowered active area by reducing ionic contact between the electrodes or reducing cathode utilization. Once the bubble passes through the cathode and

leaves in the catholyte exit stream fuel cell performance recovers resulting in ‘spikes’ as seen in Figure 6.23. Secondly, over time as more bubbles develop the system approaches failure as the liquid acid electrolyte is flushed out from the gap between the electrodes by the hydrogen stream. Over time bubble build up and removal from the cathode allows fuel cell performance to recover. However, as some bubbles remain in the cathode the fuel cell only recovers partially as seen by the consecutive lower peak of the spikes. This also explains the shorter time between consecutive spikes. Over time a constant flux of bubble removal into the flow channels prevents recovery of fuel cell performance with time between performance recoveries becoming shorter. This was observed for both durability tests except fuel cell failure at 400 mA/cm² was reached much earlier. This fuel cell failure is likely related to the concentration of the recirculating catholyte as seen in the next section. Therefore, investigation of different operating parameters to improve durability was carried out.

The following steps were taken to improve fuel cell durability:

1. Decreasing the hydrogen flow rate: to reduce the possibility of hydrogen bubbles forming by lowering the pressure on the liquid acid electrolyte. When hydrogen flow is extremely high the hydrogen forces the liquid electrolyte into the cathode channels and the hydrogen can be seen exiting in the catholyte stream. This leads to fuel cell failure.
2. Increasing the redox catholyte flow rate: to improve the removal of gas bubbles from the cathode by increasing the velocity of the liquid catholyte in the channels.
3. Using a thinner 3-D cathode (no BASF TGP-H-120): to reduce the build-up of bubbles in the cathode by providing a smaller distance for the bubbles to travel to the cathode channels.

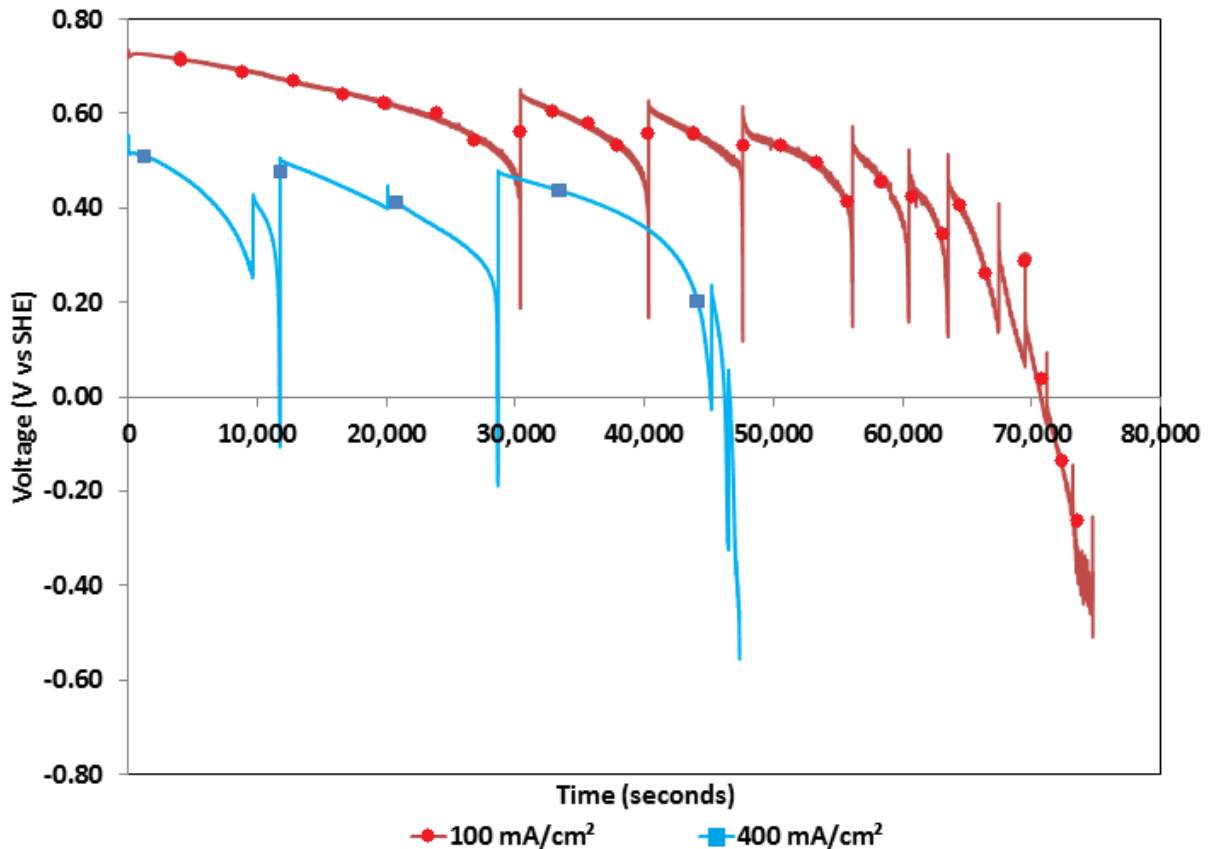


Figure 6.23: Durability testing of the HRFC under different current densities.

Temperature: 60°C, Bladder Pressure: 20 psi, Anode: 0.1 mg/cm² 20% Pt/C (30% Nafion®), 1 mg/cm² C sublayer (20% PTFE) on Toray TGP-H-090 20% WP, Cathode: Sigracet 25 DA GDL 20% WP, TGP-H-120, 1 mg/cm² C MPL (15% Nafion®) on TGP-H-090 no WP, Catholyte: 4 ml/min, 2 M Fe(ClO₄)₃, 0.22 M Fe(ClO₄)₂, 0.2 M HClO₄, Fuel: 105 ml/min non-humidified hydrogen at line pressure of 30 psi, Electrolyte in spacer: 0.5 M HClO₄.

Figure 6.24 shows system durability at 60°C with 0.5 L of the catholyte 2 M Fe(ClO₄)₃, 0.22 M Fe(ClO₄)₂, 0.2 M HClO₄ recirculated at 6 ml/min and a non-humidified hydrogen flow rate of 55 ml/min compared to the previous test of 4 ml/min and 105 ml/min, respectively. Much improved durability and system stability was observed for this configuration emphasizing the effect different components and operating conditions can have on the operation of this type of fuel cell. It was expected that at a lower current density such as 100 mA/cm² fuel cell operation over 24 hours would degrade much more significantly than the 5.4 mV/hour (page 111) degradation observed due to relatively higher rates of redox

electrolyte crossover leading to fuel cell failure but this was not the case over the 24 hour duration of the experiment. Although redox electrolyte crossover definitely contributes to cell voltage degradation other factors including loss of liquid acidic electrolyte and discharge of the recirculating redox electrolyte also contribute to cell voltage degradation. Though ionic conductivity between the electrodes remains for the duration of the experiment the composition of the acidic liquid electrolyte changes with ferrous ions and perchloric acid build up in the gap over time change electrolyte composition. This could potentially have some impact on fuel cell voltage degradation with respect to adsorption of the acid on to the Pt anode. Furthermore evaporation of the acidic liquid electrolyte and its subsequent loss through the anode exit stream could also affect the overall cell resistance leading to some cell voltage loss.

Also shown in Figure 6.24 are the theoretical voltage change that would be expected at equilibrium potential if the concentration of the ferric ions in solution, and thus the ratio of ferric to ferrous ions were changing at a Faradaic rate of 100 mA/cm² and 400 mA/cm². It would be expected that the voltage degradation at 100 mA/cm² over 24 hours related to ferric concentration would be 47 mV. Correcting for this the membraneless hydrogen redox fuel cell voltage degradation at 100 mA/cm² over 24 hours was approximately 75 mV, or a degradation rate of approximately 3.1 mV/hour.

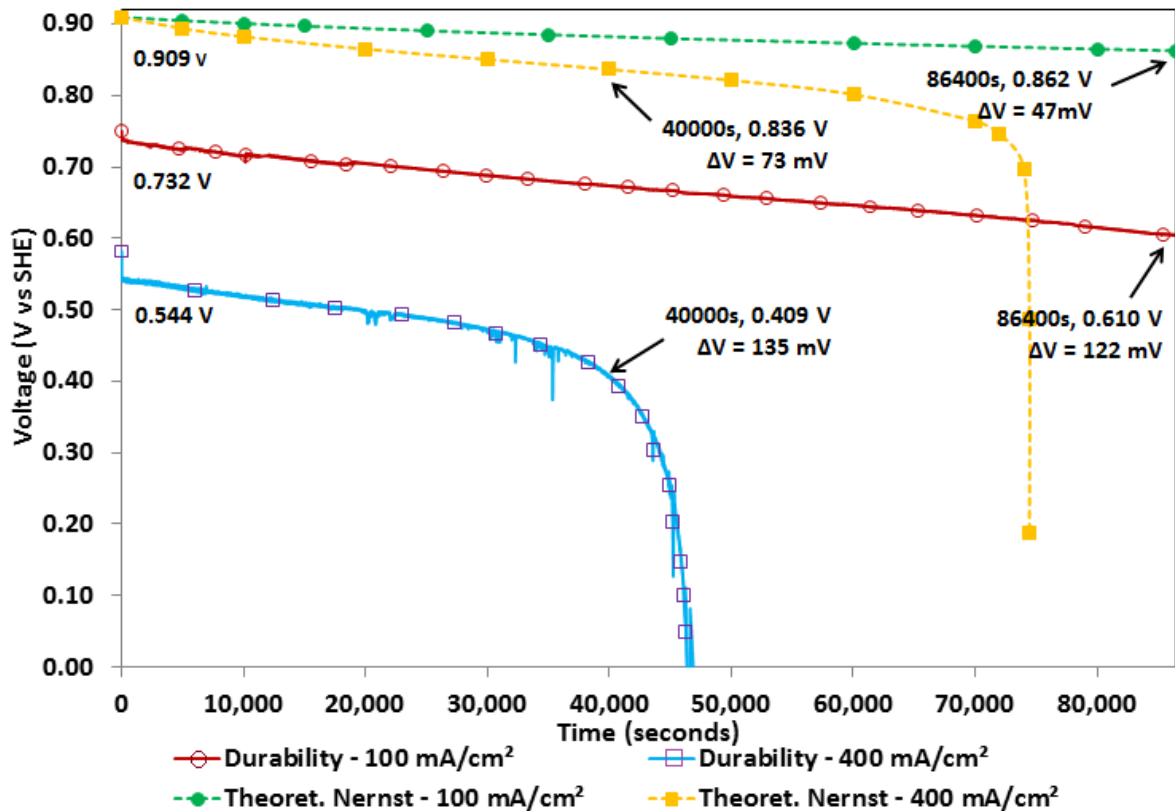


Figure 6.24: Durability testing of the DHRFC under different current densities with expected degradation due to concentration change of the iron redox catholyte.

Temperature: 60°C, Bladder Pressure: 20 psi, Anode: 0.1 mg/cm² 20% Pt/C (30% Nafion®), 1 mg/cm² C sublayer (20% PTFE) on Toray TGP-H-090 20% WP, Cathode: Sigracet 25 DA GDL 20% WP, 1 mg/cm² C MPL (15% Nafion®) on TGP-H-090 no WP, Catholyte: 6 ml/min 2 M Fe(ClO₄)₃, 0.22 M Fe(ClO₄)₂, 0.2 M HClO₄, Fuel: 55 ml/min non-humidified hydrogen at 30 psi, Electrolyte in spacer: 0.5 M HClO₄.

Fuel cell failure at 400 mA/cm² begins to occur just before 11 hours (40000 seconds). This failure is related to the changing concentration of the ferric ion. A Faradaic calculation suggest that at this current density for 40000 seconds approximately 0.54 mol of the ferric ion or 54% of the initial ferric content (0.5 L of 2 M Fe³⁺ initially) would have been consumed. As the solution was initially at 90% state of charge (9:1 Fe³⁺ to Fe²⁺ ratio) the state of charge of the ferric redox electrolyte after 40000 seconds is 41%. The molar flow rate at this concentration of 0.0056 mol/min should be enough to satisfy the Faradaic requirement of 0.00081 mol/min. However, as a large portion of this reactant reaching the

catalyst is product ferrous ions the diffusion at the catalyst surface of the required ferric ions is likely too low for the reaction to be sustained. Furthermore, a similar trend is observed for the theoretical Nernst potential for 400 mA/cm² as seen in the sharp drop in cell voltage in Figure 6.24. Fuel cell voltage degradation in the time period before fuel cell failure begins (11 hours) was approximately 135 mV over 11 hours. The concentration related voltage degradation correction at this current density over 11 hours is approximately 73 mV. This corresponds to a fuel cell voltage degradation not related to catholyte concentration change of approximately 5 mV/hr. which is similar to that at 100 mA/cm².

Figure 6.24 is a comparison of membraneless DHRFC polarization curves with different state of charge (SOC) catholytes. The 90% SOC is associated with catholyte concentrations at the beginning of the durability tests in Figure 6.24 while the 41% SOC is associated with concentrations after 40000 seconds of operation at 400 mA/cm². The polarization curves shown in Figure 6.24 are under the same conditions as the durability tests in Figure 6.24.

Membraneless DHRFC polarization curves at 41% SOC indicate that fuel cell voltage at this concentration should be ~0.23 V. However, at the same concentration fuel cell voltage (40000s) in the durability test is significantly higher at ~0.41 V. It may be hypothesized that a threshold SOC of the redox catholyte exists above which fuel cell performance due to the concentration of the redox species at the catalyst surface is not significantly affected. After the redox catholyte concentration falls below this threshold concentration, effects of the redox species concentration at the catalyst surface start to become magnified. For the durability testing as the concentration of the redox catholyte decreases and drops below a threshold concentration the cell voltage begins to degrade faster. It is likely that fuel cell

voltage predicted by polarization curves for even moderately higher SOC electrolytes (e.g., 50%) are closer to those in the durability testing. This could possibly explain the large discrepancy between the results in the polarization curve and durability testing at 400 mA/cm². Regardless of the reason for this discrepancy it is clear the fuel cell performance failure in the durability testing in Figure 6.24 is related to the concentration of the iron redox catholyte.

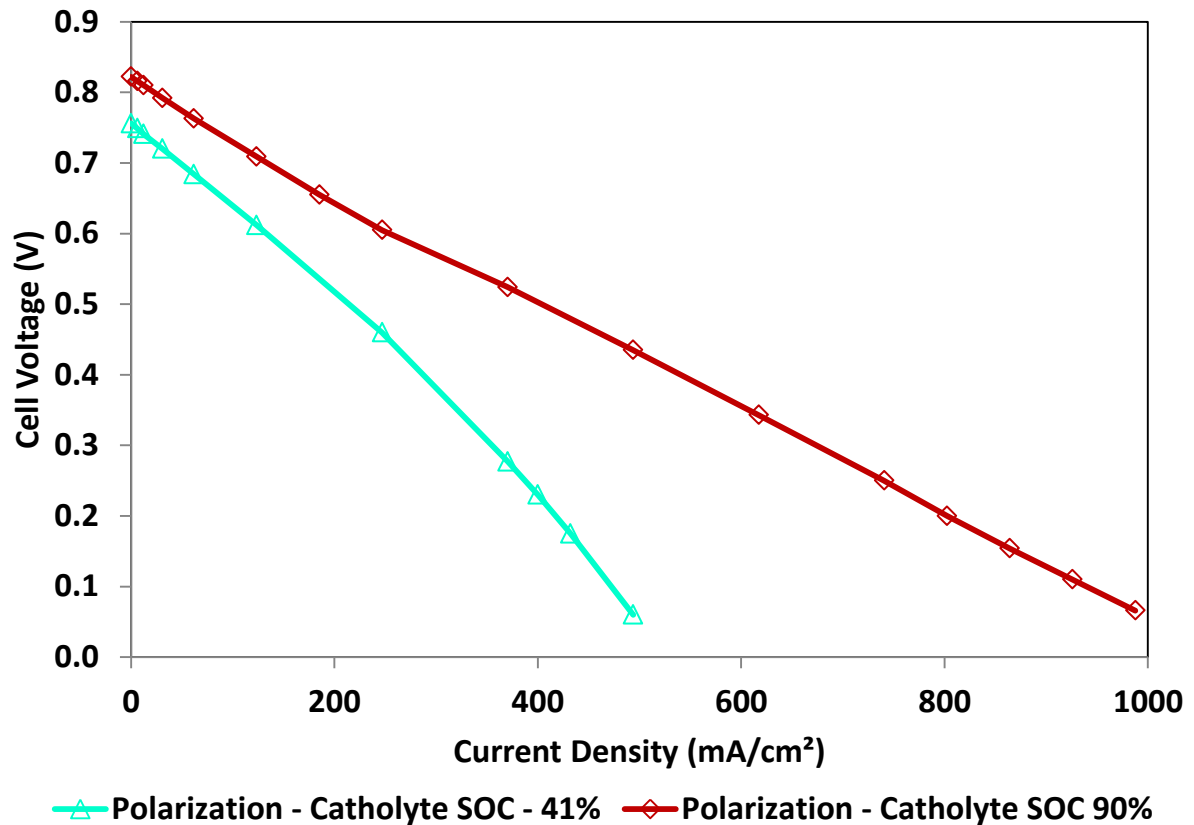


Figure 6.25: Effect of catholyte state of charge (SOC) on membranless DHRFC performance. Temperature: 60°C, Bladder Pressure: 20 psi, Anode: 0.1 mg/cm² 20% Pt/C (30% Nafion®), 1 mg/cm² C sublayer (20% PTFE) on Toray TGP-H-090 20% WP, Cathode: Sigracet 25 DA GDL 20% WP, 1 mg/cm² C MPL (15% Nafion®) on TGP-H-090 no WP, Catholyte: 6 ml/min 2 M Fe(ClO₄)₃, 0.22 M Fe(ClO₄)₂, 0.2 M HClO₄, Fuel: 55 ml/min non-humidified hydrogen at 30 psi, Electrolyte in spacer: 0.5 M HClO₄.

6.3 Demonstration of Flexibility of Membraneless

Design

The first part of this thesis (sections 6.1 and 6.2) met three of the four objectives of this project; developing a membraneless electrode assembly for an active fuel cell system, using the membraneless electrode assembly to help address membrane issues in the DFRFC and the demonstration of a low cost hydrogen fuel cell (i.e., no membrane and very low total PGM-catalyst). The remaining objective of this project was to demonstrate the flexibility of the 3-D electrode design to different fuels, oxidants, electrolytes and platforms. For the membraneless direct hydrogen redox fuel cell a 3-D cathode with a conventional anode was used for this gas/liquid system. Previous work by Lam, Wilkinson et. al had developed a passive membraneless DMFC with a 3-D anode [69]. The membraneless DMRFC developed and discussed below demonstrates a liquid/liquid system with both a 3-D cathode and a 3-D anode. The testing performed was not as exhaustive with respect to different parameters as for the membraneless DHRFC. However, an effort is made to explain some of the phenomena though much work remains to determine optimized operating conditions, electrode designs and electrolyte compositions and gain complete understanding of this system.

6.3.1 The Membraneless DMRFC

In general the design of the 3-D cathode for the membraneless DMRFC was the same as that shown in Figure 6.1 for the membraneless DHRFC though the components used were slightly different. A comparison of the membraneless electrode assemblies for the DMRFC and DHRFC can be found in Table 6.5. The hydrophobic cathode GDL in component 6

(Figure 6.1) has a hydrophobic micro-porous layer applied to it. The rest of the 3-D cathode components were kept the same. The 3-D anode structure used for the membraneless DMRFC was different to that for the hydrogen system. The catalyst layer here was applied on a hydrophilic GDL without a carbon sublayer present. In addition the catalyst layer was applied to both sides of the GDL. Finally, the cathode flow channels were of the same dimensions as for the DHRFC but the anode flow channels were different and had dimensions of 0.58 mm (width) x 0.30 mm (depth). The membraneless DMRFC was operated with a 0.5 M HClO₄ electrolyte initially provided into the gap between the anode and cathode. The liquid acid electrolyte was then supplied to the fuel cell from the methanol fuel stream as opposed to from the redox catholyte stream as in the membraneless DHRFC. In a liquid-liquid system the acid electrolyte may be supplied to the fuel cell from either the anolyte or the catholyte.

Table 6.5: Comparison of the components used for the gas/liquid membraneless DHRFC and the liquid/liquid membraneless DMRFC.

	DHRFC (gas/liquid)	DMRFC (liquid/liquid)
3-D Cathode Component		
Component 4: Hydrophilic MPL	1 mg/cm ² C MPL (15% Nafion®)	1 mg/cm ² C MPL (15% Nafion®)
Component 5: Hydrophilic GDL	non-WP TGP-H-090	non-WP TGP-H-090
Component 6: Hydrophobic GDL	Sigracet 25 DA GDL	Sigracet 25 BC GDL(MPL w/20% PTFE)
Anode Structure		
Gas Diffusion Layer	Hydrophobic: 20%WP TGP-H-090	Hydrophilic: non-WP TGP-H-060
Microporous Layer	Hydrophobic: 1 mg/cm ² C (20% PTFE)	None
PGM Catalyst Layer	Hydrophilic: 0.2/0.1/0.05 mg/cm ² Pt 30% Nafion	Hydrophilic: 3,5 mg/cm ² Pt/Ru black 15% Nafion

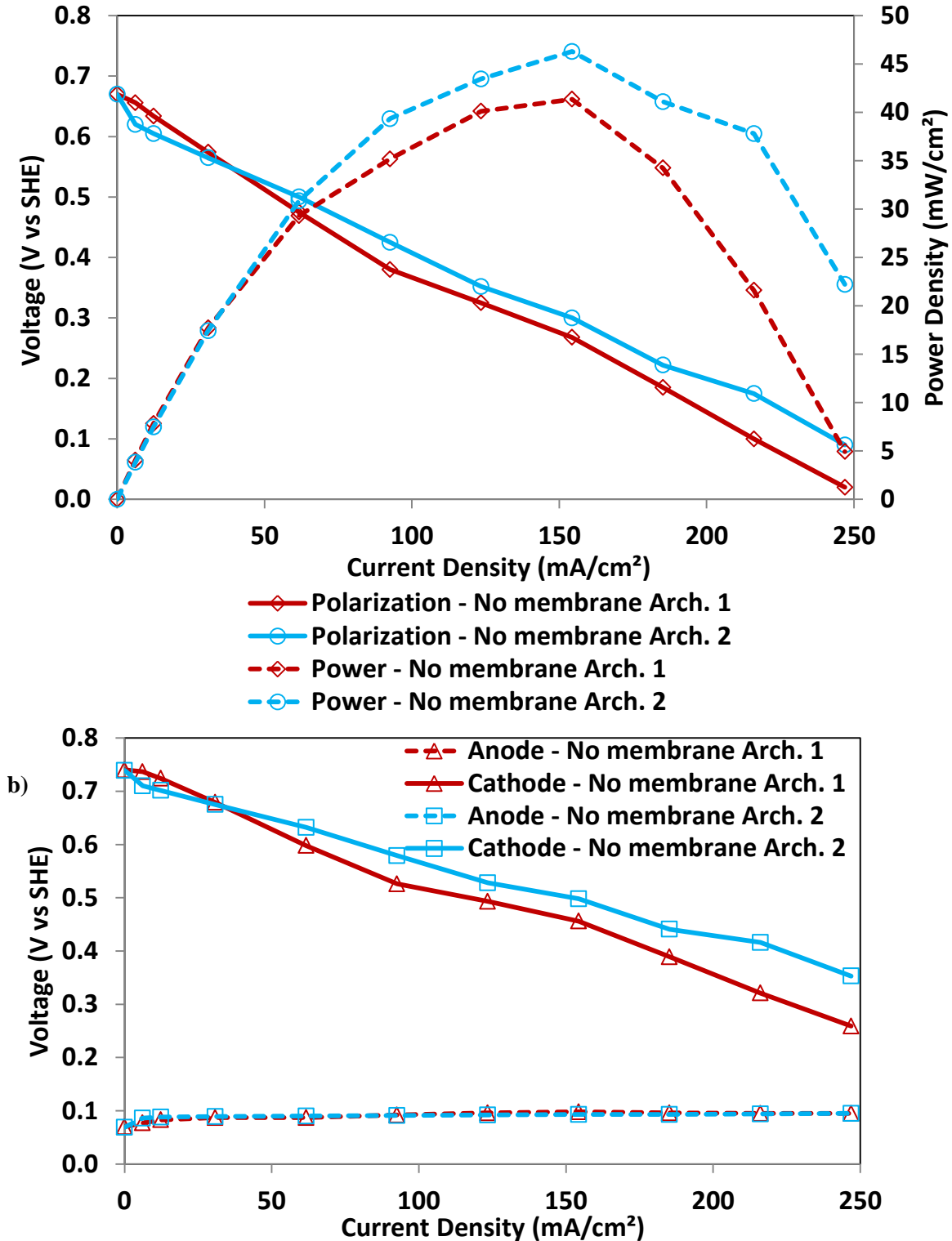


Figure 6.26: Comparison of different 3-D cathode architectures on membraneless DMRFC performance. a) Polarization and power density curves. b) Anode and cathode (iR-corrected) reference potentials.

Temperature: 60°C, Bladder Pressure: 10 psi, Anode: 3 mg/cm² and 5mg/cm² Pt-Ru black (15% Nafion®) on opposite sides of Toray TGP-H-060 20% WP, Cathode: as in Figure 3.22, Fuel: 1 M MeOH 0.1 M HClO₄ at 10 ml/min, Catholyte: 2 M Fe(ClO₄)₃, 0.22 MFe(ClO₄)₂ at 9 ml/min Electrolyte in spacer: 0.5 M HClO₄.

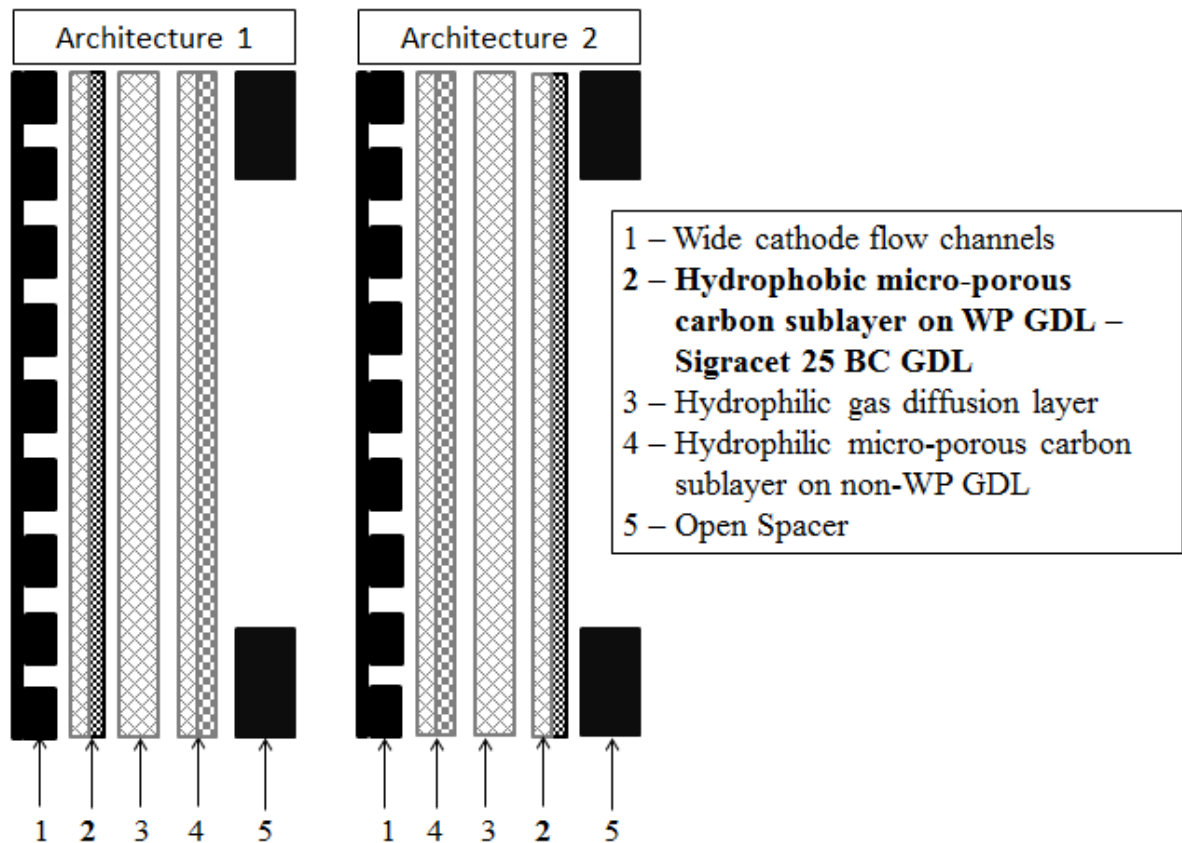


Figure 6.27: Different architectures for the 3-D cathode used in the membraneless DMRFC.

Figure 6.26a shows fuel cell polarizations for the membraneless DMRFC with two different configurations of the 3-D cathode. A conceptual non-optimized 3-D anode developed by Lam, Dara et. al. [75] and used in a co-publication with the author is also used for the membraneless DMRFC. Shown in Figure 6.26b are the anodic and cathodic polarizations for the membraneless DMRFC at the conditions in the caption. The architectures, referenced Arch. 1 and Arch. 2 in Figure 6.26, are shown in Figure 6.27. Fuel cell reference electrode measurements were performed using a saturated calomel electrode at the inlet of the anode fuel stream. The circuit was then completed by connecting the reference electrode to the multistat and the multistat to the anode current collector. The only difference between the architectures is the position of the Sigracet 25 BC GDL. It is evident

from identical anode polarizations in Figure 6.27b that the change in architecture does not affect anode performance. This also indicates that both of the 3-D cathode architectures provide equally effective control over redox catholyte crossover since the anode polarizations are nearly identical. It is also observed that ‘Architecture 2’ performs slightly better than ‘Architecture 1’ with peak power densities achieved of 46 mW/cm² compared to 41 mW/cm². However, these differences between the two architectures are attributed to variability in this system and the performance for the different architectures is considered similar.

Figure 6.28a shows a comparison of the membraneless DMRFC and the conventional Nafion-117 PEM-based DMRFC under the same conditions (see Figure 6.28 caption) while Figure 6.28b shows the anodic and cathodic performance for the membraneless DMRFC. The PEM-based DMRFC had a higher OCV of 0.72 V compared to 0.67 V for the membraneless DMRFC. Theoretical Nernst potential calculations at redox catholyte concentrations of 2 M Fe(ClO₄)₃ and 0.22 M Fe(ClO₄)₂, and a methanol concentration of 1 M and a pH of 1 suggest the OCV should be 0.817 V vs. SHE at 60°C. The large difference between the measured OCV and the theoretical Nernst potential for both the membrane and membraneless cases can likely be attributed to crossover of the iron catholyte. The crossover of the iron catholyte to the methanol anode results in mixed potentials at the anode which is likely the largest contributor to the lowered OCV. As the cathode does not contain any catalyst that is electrochemically active towards methanol, crossover of methanol does not have any adverse effects at the cathode with respect to a mixed potential. However, crossover of the methanol fuel solution can result in dilution of the iron catholyte which would also lower the measured OCV. In addition some difference in measured and calculated OCV can

also be attributed to the values (i.e., concentration and pH) used for activity of species to calculate the Nernst potential and actual activity of the species at the catalyst sites.

The Nafion® 117 DMRFC demonstrated higher OCV compared to the membraneless DMRFC. This difference is due to the Nafion® membrane having lower rates of crossover of the iron redox catholyte than the membraneless architecture. A comparison of the anode OCV in Figure 6.28b shows that the anode in the PEM-based DMRFC performed better with a voltage of 0.020 V compared to an anode polarization for the membraneless DMRFC of 0.070 V while the cathode OCVs are identical. As the standard electrode potential of the $\text{Fe}^{3+}/\text{Fe}^{2+}$ redox couple is 0.77 V vs. SHE while that of methanol is 0.016 V vs. SHE crossover of the redox catholyte to the anode will shift the anode polarization in a more positive direction which is as observed.

Fuel cell and cathode performance in the activation region ($< 15 \text{ mA/cm}^2$) are similar for the membraneless and Nafion® 117 DMRFC. However, some differences in the activation region for the anode for the membraneless and Nafion® 117 DMRFC are observed. The anode for the PEM-based DMRFC has lower potentials than those for the membraneless DMRFC though the relative losses at the anode with increasing current density are similar for the two cases. Hence, improvements in anode polarization for the PEM-based DMRFC are related to lower crossover of the iron catholyte and not necessarily improved kinetics.

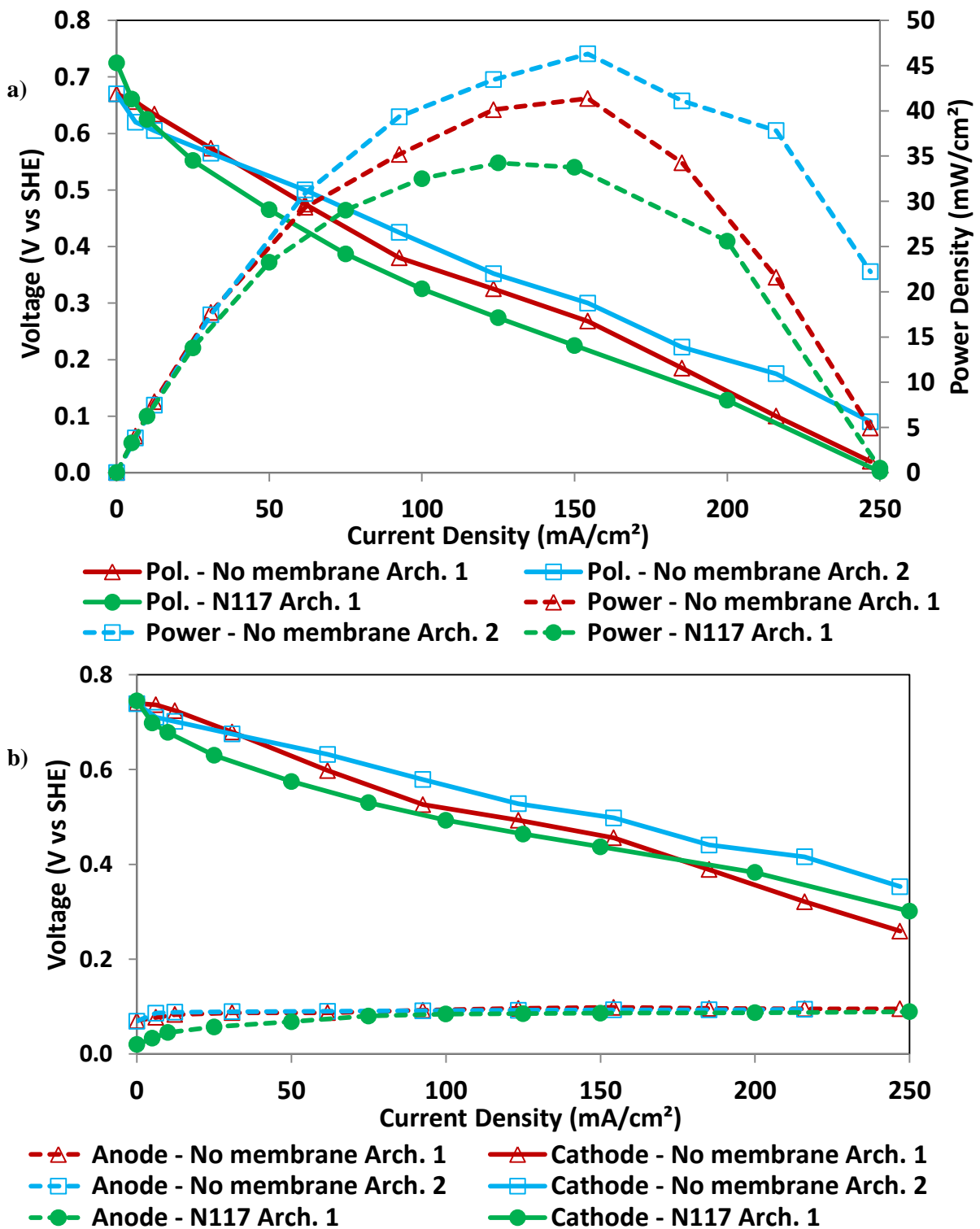


Figure 6.28: Comparison of membraneless DMRFC performance with a conventional Nafion 117 based DMRFC. a) Polarization and power density curves. b) Anode and cathode (iR-corrected) reference potentials.

Temperature: 60°C, Bladder Pressure: 10 psi, Anode: 3 mg/cm² and 5mg/cm² Pt-Ru black (15% Nafion®) on opposite sides of Toray TGP-H-060 20% WP, Cathode: as in Figure 3.22 for membraneless, Arch. 1 for membrane case Fuel: 1 M MeOH 0.1 M HClO₄ at 10 ml/min, Catholyte: 2 M Fe(ClO₄)₃, 0.22 M Fe(ClO₄)₂ at 9 ml/min Electrolyte in spacer: 0.5 M HClO₄, Nafion® 117 for membrane case.

The benefits of improved conductivity and lower resistance due to the use of the acid electrolyte and open spacer over the membrane are seen in the ohmic region of the polarization curves. The overall cell resistance for the membraneless and Nafion 117 based DMRFC were measured to be 0.170 Ω and 0.210 Ω , respectively. This resulted in slightly divergent fuel cell performance with the membraneless DMRFC outperforming the membrane based DMRFC. Finally, under the conditions of this demonstration neither the membraneless DMRFC nor the Nafion 117 based DMRFC became mass transport limited.

A comparison of the anode and cathode potentials for both the membrane and membraneless DMRFC shows that the anode polarization losses are significantly lower than the cathode polarization losses. It appears that the cathode is limiting fuel cell performance which is counter-intuitive to what would be expected of this system. The $\text{Fe}^{3+}/\text{Fe}^{2+}$ reduction reaction has a very high exchange current density ($\sim 10^{-2}$ A/cm² on carbon) and is a single electron transfer process while the methanol oxidation reaction (MOR) is a six electron transfer process which proceeds through multiple steps and is well known to have high performance losses. It is unclear whether this is an artifact of experimental error with respect to the reference electrode or whether effects related to the electrochemical reactions are responsible for this. A deeper understanding of the reactions involved and the electrochemical system is required to understand this system better. However, this does not take away from the project objective of demonstrating flexibility of design of the membraneless electrode assembly as an active membraneless liquid-liquid fuel cell was successfully operated. In addition, this membraneless electrode assembly outperformed the conventional membrane electrode assembly.

6.3.2 Comparison with Conventional MEA DMFC

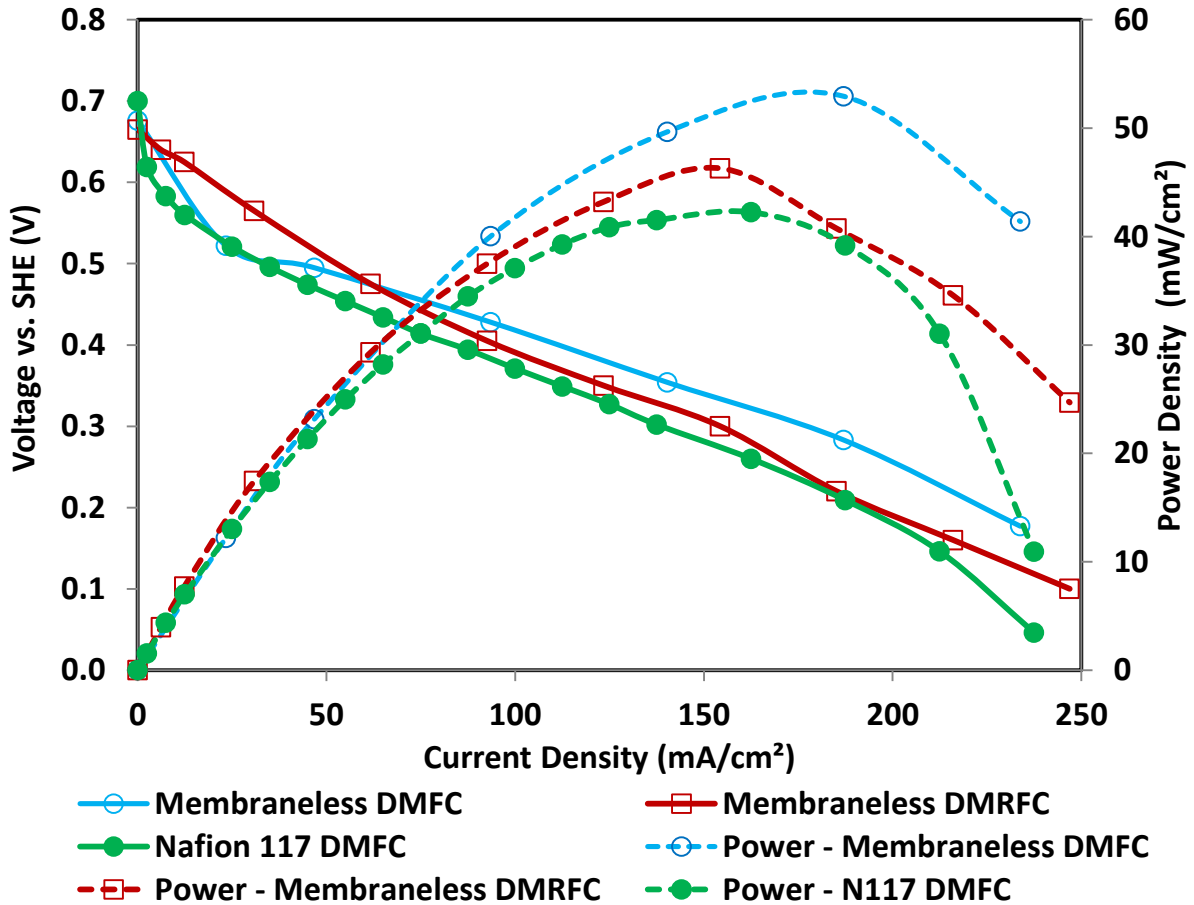


Figure 6.29: Comparison of membraneless DMRFC performance with a membraneless and Nafion® 117 DMFC.

Temperature: 60°C, Bladder Pressure: 10 psi, Anode: 3 mg/cm² and 5mg/cm² Pt-Ru black (15% Nafion®) on opposite sides of Toray TGP-H-060 20% WP, Cathode: Arch. 2 as in Figure 6.27 for DMRFC, 6.1 mg/cm² Pt-black (10% Nafion), 1 mg/cm² C MPL (20% PTFE) on 20% WP TGP-H-060, Fuel: 1 M MeOH 0.1 M HClO₄ at 10 ml/min for DMRFC, 1 M MeOH 0.2 M H₂SO₄ at 2 ml/min for DMFC, Oxidant: 2 M Fe(ClO₄)₃, 0.22 MFe(ClO₄)₂ at 9 ml/min for DMRFC, 36 ml/min air for DMFC, Electrolyte in spacer for membraneless: 0.5 M HClO₄ for DMRFC, 0.2 M H₂SO₄ for DMFC.

The DMFC and DMRFC are different systems with several similarities. A comparison between the performances of a conventional Nafion® 117 DMFC, membraneless DMFC and a membraneless DMRFC under similar conditions is shown in Figure 6.29. The details of the conditions can be found in the caption for Figure 6.29. The membraneless DMRFC demonstrated improved performance over both the membraneless

DMFC and the Nafion® 117 DMFC in the activation region ($< 15 \text{ mA/cm}^2$) as seen by the significantly lower fuel cell performance losses in this region. The membraneless DMFC demonstrated superior performance in the ohmic region over the membraneless DMRFC and Nafion® 117 DMFC. This is related to the lower resistance for the membraneless DMFC, 0.121Ω compared to 0.170Ω and 0.215Ω for the membraneless DMRFC and Nafion® 117 DMFC, respectively. Investigation and optimization of operating parameters, electrolyte composition, electrode and components design, and materials is expected to significantly improve fuel cell performance for both the membraneless DMFC and membraneless DMRFC.

6.3.3 Membraneless DMRFC Durability

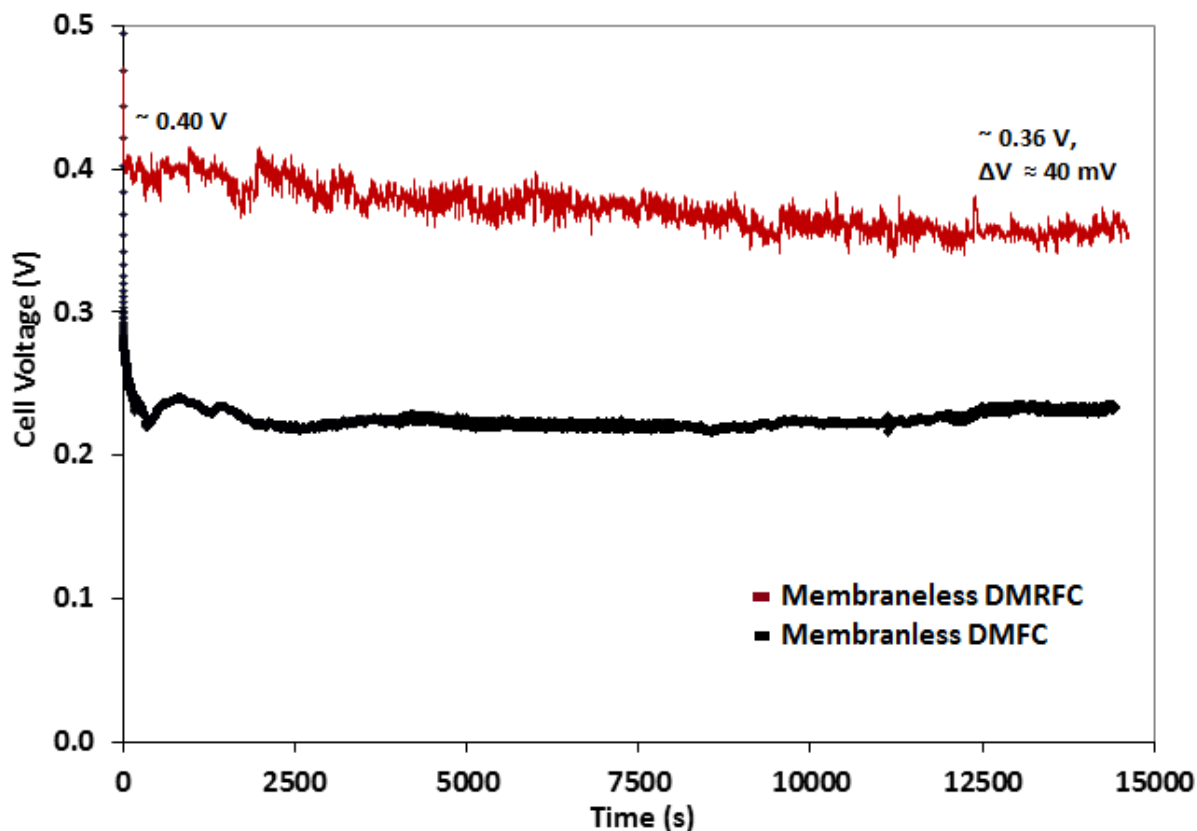


Figure 6.30: 4 hour durability of the membraneless DMRFC and DMFC at 100 mA/cm².

Temperature: 60°C, Bladder Pressure: 10 psi, Anode: 3 mg/cm² and 5mg/cm² Pt-Ru black (15% Nafion®) on opposite sides of Toray TGP-H-060 20% WP, Cathode: Arch. 2 as in Figure 3.22, Fuel : 1 M MeOH 0.1 M HClO₄ at 11 ml/min for DMRFC, 1 M MeOH 0.5 M H₂SO₄ at 1 ml/min for DMFC, Catholyte: 2 M Fe(ClO₄)₃, 0.22 M Fe(ClO₄)₂ at 10 ml/min, 36 ml/min air for DMFC Electrolyte in spacer: 0.5 M HClO₄ for DMRFC, 0.5 M H₂SO₄ for DMFC.

A 4 hour durability study at 100 mA/cm² for the membraneless DMRFC is shown in Figure 6.30. Like the membraneless DHRFC 0.5 L of the iron redox catholyte was recirculated while the methanol fuel was used in a single pass configuration for the membraneless DMRFC. For the membraneless DMFC 0.5 L of the methanol fuel was recirculated. Other details of the durability experiment can be found in the caption. Satisfactory performance under the conditions shown was observed although voltage oscillations and fluctuations for the all liquid membraneless DMRFC system were observed

to be larger than that for the gas-liquid membraneless DHRFC system or membraneless DMFC. While both the membraneless DHRFC and DMFC demonstrated negligible oscillations in voltage ($< 2\text{mV}$) the membraneless DMRFC demonstrated voltage oscillations in the range of 5-10 mV over very short periods of time (< 10 seconds). These voltage oscillations are associated with carbon dioxide production from methanol oxidation. Membraneless DMRFC performance decreases as the product carbon dioxide blocks access of the liquid reactants to catalyst sites and recovers as it is removed. Voltage degradation for membraneless DMRFC over the period of the durability study was approximately 9 mV/hr. In comparison the membraneless DMFC performed significantly better with almost no voltage degradation over the 4 hour period. This voltage degradation is approximately 4 mV/hr. greater than that for the membraneless DHRFC at the same load (100 mA/cm^2). The gas-liquid platform offers an advantage in this configuration in that mixing of the electrolytes is not a concern as the different phases largely prevent this from happening. The liquid-liquid system on the other hand suffers from mixing of the fuel and redox catholyte which in addition to Faradaic consumption of the ferric ions further lowers the concentration of the redox catholyte. This contributes to the additional membraneless DMRFC voltage degradation compared to the membraneless DHRFC at the same load.

7 Conclusions

The work in this thesis focused on developing a membraneless electrode assembly using a controlled reactant gradient approach for use in a direct fuel redox fuel cell. A 3-D electrode was used to control the reactant concentration gradients. This 3-D electrode in conjunction with an open spacer and liquid acid electrolyte was successfully used to eliminate the membrane from a conventional membrane electrode assembly under active conditions. In addition to a membraneless direct hydrogen redox fuel cell (DHRFC) preliminary membraneless electrode assembly design for a direct methanol redox fuel cell (DMRFC) was also developed to demonstrate the flexibility of this method to different electrolytes, fuels and oxidants. The elimination of the membrane and the reduction in Pt-catalyst content due to the use of the liquid acid electrolyte promises significant reductions in cost for a hydrogen fuel cell. The experimentation in this research led to several conclusions:

- Effective operation of this new membraneless electrode assembly requires control of not only the 3-D electrode(s) but also the anode and cathode flow channels in the flow fields. Control of the flow channels and their optimization can help control transport of the reactants into the 3-D electrode.
- Optimization of flow rates is important to balance full 3-D electrode utilization and reactant crossover rates.
- Increasing temperatures improve fuel cell performance by improving ionic conductivity of the solutions as well as by improving diffusion rates of the ions.
- The effects of lower activation losses, improved conductivity and lower ohmic losses for the membraneless electrode assembly were seen in the improved fuel cell performance compared to the conventional membrane electrode assembly. The

membraneless DHRFC achieved peak power densities upwards of 220 mW/cm² compared to 173 mW/cm² for the Nafion® 112 DHRFC under the same conditions when a non-humidified hydrogen fuel was used.

- The non-humidified hydrogen Nafion® 112 DHRFC was limited by the number of TPS available at the anode. This led to increased activation losses at the anode and the earlier appearance of the mass transport region with limiting current densities achieved of 600 mA/cm².
- Humidification of the hydrogen fuel for the Nafion® 112 DHRFC reduced activation losses and extended the mass transport region to 700 mA/cm². A peak power density of 208 mW/cm² was achieved for the Nafion® 112 DHRFC with humidified hydrogen which was an improvement over the non-humidified hydrogen Nafion® 112 DHRFC. However, this configuration still appeared to be limited by the number of TPS at the anode and performance was inferior to the membraneless DHRFC under the same conditions.
- The use of the liquid acid electrolyte in the membraneless DHRFC configuration increases the number of TPS available by infiltrating the pores and providing more effective ionic contact in the anode catalyst layer. This is seen in membrane and membraneless DHRFC performance comparison where the membraneless DHRFC achieved current densities significantly higher than those of the membrane DHRFC.
- The number of TPS available to the membraneless DHRFC allow for more effective utilization of the anode catalyst layer ensuring that the membraneless DHRFC is not limited at the anode. In addition the increased number of TPS significantly reduces activation losses relative to the Nafion® 112 DHRFC. Due to this increase in anode

TPS a clear activation region for the membraneless DHRFC does not appear and ohmic losses dominate.

- The extremely linear polarization curves of the membraneless DHRFC indicates that the fuel cell is mainly under ohmic control even though fuel cell performance compared to the Nafion® 112 DHRFC in the ohmic region has slightly improved.
- More effective utilization of the anode catalyst layer for the membraneless DHRFC allows for significant reduction in anode Pt-catalyst loadings. The membraneless DHRFC was operated with different Pt-loadings anode in the range of 0.05-0.2 mg/cm² Pt with no losses in fuel cell performance with regards to the 220 mW/cm² peak power densities achieved.
- Fuel cell performance for the 0.2, 0.1 and 0.05 mg/cm² Pt loadings anode was identical in the activation and ohmic regions. However, with consecutive halving of the anode catalyst loading the mass transport region appeared earlier. Limiting current density of 925 mA/cm² was achieved with the 0.2 mg/cm² Pt anode while a limiting current density of only approximately 700 mA/cm² was possible with the 0.05 mg/cm² Pt anode. This indicates the hydrogen oxidation reaction (HOR) becomes more performance limiting with Pt-catalyst reduction due to the lower number of TPS that are available.
- Humidification of the hydrogen in the membraneless DHRFC improved fuel cell performance in the ohmic region by reducing fuel cell resistance and extending the mass transport region. As activation losses are already very low humidification (and thus the associated increase in the number of TPS) does not affect fuel cell performance in the activation region. Virtually identical polarization curves with peak

power densities of 250 mW/cm² were observed for the humidified hydrogen membraneless DHRFC with both 0.05 mg/cm² and 0.2 mg/cm² Pt anodes. Compared to the non-humidified membraneless DHRFC and humidified Nafion® 112 DHRFC this represents an improvement of 14% and 20%, respectively.

- Further improvement of the membraneless DHRFC electrodes and fuel cell hardware is required to reduce ohmic losses as the fuel cell resistance is still relatively high but less than the Nafion® 112 DHRFC.
- A durability study on the membraneless DHRFC was carried out with a recirculating iron redox catholyte at 100 mA/cm² and 400 mA/cm². Fuel cell durability was found to be greatly affected by fuel and oxidant flow rates due to the formation of hydrogen bubbles. At lower catholyte flow rate, higher hydrogen flow rate and a thicker cathode fuel cell voltage degraded considerably during the durability study as hydrogen bubbles were observed to crossover to the cathode where they were trapped. Once these bubbles were removed fuel cell voltage recovered. This was observed for both current densities.
- Increasing the catholyte flow rate, decreasing hydrogen flow rate, and using a thinner cathode improved fuel cell durability. With these changes the membraneless DHRFC could be operated for at least 24 hours at 100 mA/cm² with no performance issues. Voltage degradation was due to a combination of lowering redox catholyte concentration and unreacted oxidant crossover. Fuel cell voltage degradation not related to changing redox catholyte concentration was approximately 3 mV/hr. for 100 mA/cm² over 24 hours.

- Fuel cell durability was satisfactory over 11 hours at 400 mA/cm² (degradation in absence of concentration change) with voltage degradation of approximately 5 mV/hr. However, fuel cell performance failure began before 11 hours. This failure is likely related to the recirculating redox catholyte concentrations being too low (SOC ~41% after 11 hours). It is estimated that a minimum catholyte state of charge greater than 50% should be maintained.
- A membraneless direct methanol redox fuel cell (DMRFC) was also demonstrated. This represents a liquid-liquid system as opposed to the membraneless gas/liquid DHRFC. The flexibility of the controlled reactant gradient membraneless electrode assembly was therefore successfully demonstrated for two different cases.
- The benefits of improved conductivity and lower ohmic losses were also observed for the membraneless DMRFC as its performance was superior to that of the Nafion® 117 DMRFC.
- The membraneless DMRFC was shown to operate for 4 hours at 100 mA/cm² under a recirculating catholyte and single-pass methanol fuel stream. Voltage degradation of approximately 9 mV/hr. was observed which is significantly higher than that for the membraneless DHRFC with redox catholyte concentration effects included. The higher voltage degradation for this system is attributed to fuel and oxidant mixing which dilutes the redox catholyte concentration resulting in lower concentrations at cathode catalyst sites.

The work in this thesis focused on fuel cell technology though the potential to apply this membraneless approach to other different electrochemical technologies exists. The most obvious application of this technology could be in redox flow batteries where membrane

servicing and maintenance over the life-time of the battery can be costly. In addition, the use of the membraneless electrode assembly can provide significant cost savings by elimination of the membrane and low precious metal content can be achieved with the use of a redox species based electrode. The use of the liquid acid electrolyte also allows for a significant reduction in Pt-content at the anode for the hydrogen redox fuel cell. This reduction in combination with no PGM-catalyst at the cathode, elimination of heat and possibly water management balance-of-plant components, allows for a significant reduction in the fuel cell system cost for a hydrogen based system. However, the benefits achieved for this overall system have the downside that this system would require the incorporation of a regeneration system. A novel regeneration system has been demonstrated by Ilicic, Wilkinson et. al in a power generating system [67] using air but the incorporation of such a system would clearly increase the complexity of the overall plant. Other non-PGM catalyst systems using oxygen for regeneration could also be potentially used [76, 77]. With regards to the membraneless DMRFC the same benefits would be expected. However, the mixing of the fuel and catholyte poses some challenges with respect to system durability and reliability. Although, the objectives of this research work were met and a low cost fuel cell technology approach demonstrated, future work should build on this to address some of the other challenges that still remain.

8 Future Work and Recommendations

Previous work with the DFRFC and the work in this thesis have made considerable progress towards addressing several issues with fuel cell technology. However, several other opportunities for research remain and have emerged as a consequence of the work in this thesis. These include:

- **Optimization:** Significant work was performed on the membraneless DHRFC though optimization of the system to find ideal operating conditions is far from complete. It is recommended that flow field design, catholyte and liquid acid electrolyte compositions, open spacer design and 3-D cathode and anode structures be investigated to further lower ohmic losses which have dominated fuel cell performance. One area of work with regards to electrode design that requires improvement is that incorporation of the different layers of the 3-D electrode into a single structure as this may improve cell resistance. It is recommended that avenues for improvement of catholyte charge concentration be investigated. These may include different salts or different redox couples as well complexation of these salts and redox couples to increase their concentration. A balance between optimum concentration with regards to maximum conductivity of the catholyte solution and concentration of the active ions should also be investigated. Detailed impedance analysis should also be performed on determining the factors contributing to high resistance of the fuel cell as ohmic overpotentials have been observed to be largely dominating fuel cell performance losses. It is the author's recommendation that future work focus on the hydrogen system as opposed to the direct methanol system. The hydrogen system offers significantly more benefits with respect to Pt-content in

addition to all the other benefits that are common to both systems. Furthermore, the membraneless DHRFC allows significantly higher power densities to be achieved.

- **Development of the membraneless DMRFC:** The membraneless DMRFC was demonstrated but losses for the membraneless DMRFC are still not fully understood. More thorough testing of this system should be carried out. If methanol systems are to be further investigated a large effort must be made to mitigate the effects of mixing of the methanol fuel and catholyte. The mixing of the electrolyte poses some issues with respect to regeneration of the ferric ions from the ferrous ions. The crossover of the ferrous ions into the methanol stream and their loss would over time result in a loss of the catholyte.
- **Mixed reactant membraneless DMRFC:** One avenue of research to solve some of the issues with mixing of methanol and catholyte in the membraneless DMRFC may be to investigate a mixed reactant fuel cell. Here, the catholyte, methanol fuel and liquid acid electrolyte would all be supplied to the cathode side. The 3-D cathode should then be optimized to ensure complete reaction of the ferric ions while the unreacted methanol would crossover and react at the anode with the liquid acid electrolyte providing ionic conductivity. The ferrous product would then be recovered with the unreacted methanol and the product carbon dioxide vented. The mixed-reactant would be recirculated. With regards to resupply of the methanol an external methanol and liquid acid electrolyte storage in combination with a control system would replenish the methanol in the mixed reactant supply as required. It is the author's belief that the best possibility for further progress in the methanol system will exist with investigation of the mixed reactant system.

- **Studies on crossover of the 3-D electrode(s):** Though the 3-D electrode concept has been developed and demonstrated in a fuel cell it has not been independently analyzed. It is recommended that some work focus on the analytical determination of the concentration gradients in the 3-D electrode.
- **Regeneration and incorporation into system:** Successful regeneration of the iron redox catholyte is a key area of research for the membraneless DHRFC or DMRFC to become a viable alternative to current electrochemical energy production devices. In-situ power producing regeneration in the same fuel cell is a possibility and was demonstrated by Ilicic, Wilkinson et. al. It is recommended that this avenue be further investigated and opportunities for incorporation with the membraneless DFRFC be studied. Other methods at regeneration should also be investigated. These may include chemical regeneration using molecular oxygen in a trickle bed reactor at relatively low temperatures over activated carbon [76, 77]. This regeneration column would become an external addition to the fuel cell with the catholyte circulating between the fuel cell and the regenerator.
- **Scale up:** So far the research has focused on small-scale fuel cell development and once the above mentioned systems have been investigated scale up to larger areas and a stack is highly recommended. Scale-up of the system will likely require the development of novel flow field designs to reduce crossover of the redox catholyte. It is unlikely that serpentine channels will continue to perform as well. It is recommended that pocket channels filled with the electrode, porous flow through electrodes and parallel flow channels be investigated. In addition, scale-up of the electrodes will likely result in large areas of the electrode which are not sufficiently

compressed against the flow channels leading to poor contact resistance. It is recommended that different gasket and open-spacer designs be investigated to more evenly spread the pressure over the electrodes.

- **High Temperature:** When conventional membrane electrode assemblies are used in a PEMFC fuel cell operation temperature is limited due to issues with membrane dehydration and durability. However, with the elimination of the membrane the fuel cell operation temperature is likely limited by the vapor pressure of the iron redox catholyte or liquid acid electrolyte. With respect to the liquid acid electrolyte the potential to use a high boiling point acid like 98% phosphoric acid exists. This could allow operation temperatures up to 200°C as opposed to typical temperatures less than 90°C with Nafion® membranes. An increase in temperature would significantly increase fuel cell efficiency as well as lower ohmic losses.

References

1. G. E. Moore, "Cramming more components onto integrated circuits". *Electronics* **38** (8) (1965).
2. W.R. Grove, "On Voltaic Series and the Combination of Gases by Platinum", *Philosophical Magazine and Journal of Science* vol. XIV (1839), pp. 127-130.
3. L. Mond and C. Langer, "A New Form of Gas Battery". *Proc. Roy. Soc. London* 46 (1889).
4. "The Fuel Cell Today Industry Review 2011"
http://www.ballard.com/files/PDF/Media/The_Fuel_Cell_Today_Industry_Review_2011.pdf retrieved July 10, 2012.
5. W.T. Grubb, "Fuel Cell", US Pat. 2,913,511 (17 November, 1959).
6. W.T. Grubb and L.W. Niedrach, "Batteries with Solid Ion-Exchange Membrane Electrolytes II. Low-Temperature Hydrogen-Oxygen Fuel Cells". *J. Electrochem. Soc.*, **107** (2), (1960).
7. R.P. O'Hayre, S. Cha, W. Collela, F.B. Prinz, *Fuel Cell Fundamentals* (John Wiley & Sons Ltd., New York, 2006).
8. F. Barbir, *PEM Fuel Cells: Theory and Practice* (Academic Press, Burlington, 2005).
9. J. Zhang, "PEM fuel cell electrocatalysis", *SciTopics* (2008) Retrieved March 8, 2012, from http://www.scitopics.com/PEM_fuel_cell_electrocatalysis.html
10. D. Thompsett in *Handbook of Fuel Cells, Fundamentals, Technology and Applications*, Vol. 3, W. Vielstich, H. A. Gasteiger, and A. Lamm, Editors, Chap. 37, p.467, (John Wiley & Sons Ltd., New York 2003).

11. T. Patterson in *Fuel Cell Technology Topical Conference Proceedings*, 2002, AIChE Spring National Meeting, March, 2002.
12. K. Kinoshita, J. T. Lundquist, and P. Stonehart, "Potential Cycling Effects on Platinum Electrocatalyst Surfaces". *J. Electroanal. Chem. Interfacial. Electrochem.*, **48** (157) (1973).
13. H. Gasteiger, S.S. Kocha, B. Sompalli and F.T. Wagner, "Activity benchmarks and requirements for Pt, Pt-alloy, and non-Pt oxygen reduction catalysts for PEMFCs," *Applied Catalysis B: Environmental* **56** (2005).
14. V. Mehta and J.S. Cooper, "Review and analysis of PEM fuel cell design and manufacturing," *J. Power Sources* **114** 32-53 (2003).
15. C. Xu and T.S. Zhao, "New flow field design for PEMFCs," *Electrochem. Comm.* **9** 497-503 (2007).
16. S.G. Kandlikar and Z. Lu, "Thermal Management in a PEMFC Stack: A Brief Review of Current Status," *Applied Thermal Engineering* **29** 1276-1280 (2007).
17. R. Dillon, S. Srinivasan, A. S. Arico and V. Antonucci, "International activities in DMFC R&D: status of technologies and potential applications," *J. Power Sources*, **127** (1-2) 112-126 (2004).
18. S. K. Kamarudin, W. R. W. Daud, S. L. Ho and U. A. Hasran, "Overview on the challenges and developments of micro-direct methanol fuel cells (DMFC)," *J. Power Sources*, **163**, 2 743-754 (2007).
19. B. D. McNicol, D. A. J. Rand and K. R. Williams. "Direct methanol-air fuel cells for road transportation," *J. Power Sources*, **83**, (1-2) 15-31 (1999).

20. S. Surampudi, S.R. Narayanan, E. Vamos, H. Frank and G. Halpert, "Advances in Direct Oxidation Methanol Fuel Cells," *J. Power Sources*, **47** 377-385 (1994).
21. W. Qian, D.P. Wilkinson, J. Shen, H. Wang and J.J. Zhang, "Architecture for portable direct liquid fuel cells," *J. Power Sources*, **154** 202, (2006).
22. J. B. Ge and H. T. Liu, "Experimental studies of a direct methanol fuel cell," *J. Power Sources*, **142** (1-2), 56-69 (2005).
23. J. K. Norskov, J. Rossmeisl, A. Logadottir, L. Lindqvist, J. R. Kitchin, T. Bliggard and H. Jonsson, "Origin of the overpotential for oxygen reduction reaction at a fuel-cell cathode," *J Phys. Chem.*, **108** , 17886-17892 (2004).
24. U. A. Paulus, T. J. Schmidt, H.A. Gasteiger and R. J. Behm, "Oxygen reduction on a high-surface area Pt/Vulcan carbon catalyst: a thin-film rotating ring-disk electrode study," *J. Electroanalytical Chem*, **495**, 134-145 (2001).
25. V. Neburchilov, J. Martin, H. Wang and J. Zhang, "A review of polymer electrolyte membranes for direct methanol fuel cells," *J. Power Sources*, **169**, 221-238 (2007).
26. C. Lamy, A. Lima, V. LeRhun, F. Delime, C. Coutanceau and JM. Leger "Recent advancements in the development of direct alcohol fuel cells (DAFC)," *J. Power Sources*. **105**, 283-296, (2002).
27. T.Schaffer, T. Tschinder, V. Hacker and J. O. Besenhard, "Determination of methanol diffusion and electroosmotic drag coefficients in proton-exchange-membranes for DMFC," *Journal of Power Sources*, **153**, 210–216 (2006).
28. N. Carretta, V. Tricoli and F. Picchioni, "Ionomeric membranes based on partially sulfonated poly(styrene): synthesis, proton conduction and methanol permeation," *J. Membr. Sci.*, **166** (2), 189-197 (2000).

29. A. Sungpet, "Reduction of alcohol permeation through Nafion[®] by polypyrrole," *J. Membr. Sci.*, **226** (1-2), 131-134 (2003).
30. A. Lam, D. P. Wilkinson and Z. JiuJun. *Proton Exchange Membrane Fuel Cells*, The Electrochemical Society Proceedings Series, Pennington, NJ, pp 273–281.
31. S. Hikita, K. Yamane and Y. Nakajima. "Measurement of methanol crossover in direct methanol fuel cell," *JSAE Review*, **22** 2, 151-156 (2001).
32. D.P.Wilkinson, M. C. Johnson, K. M. Colbow and S. A. Campbell, US Patent No 5,672,439 (1997).
33. A. K. Shukla and R. K. Raman, "Methanol resistant oxygen-reduction catalysts for direct methanol fuel cells," *Ann. Rev. Mater. Research*, **33**, 155-168 (2003).
34. Z. Qi and A. Kaufman, "Low Pt loading high performance cathodes for PEM fuel cells," *J. Power Source*, **113**, 37-43 (2003).
35. R. O'Hayre, D.M. Barnett and F.B. Prinz, "The Triple Phase Boundary A Mathematical Model and Experimental Investigations for Fuel Cells," *J. Electrochem. Soc.* **152**, A439-A444 (2005).
36. A. Lindermeir, G. Rosenthal, U. Kunz and U. Hoffmann, "On the question of MEA preparations for DMFCs," *J. Power Sources*, **129** (2), 180-187 (2004).
37. F.Q. Liu, G.Q. Lu and C.Y. Wang. "Low Crossover of Methanol and Water Through Thin Membranes in Direct Methanol Fuel Cells," *J. Electrochem. Soc.* **153** 3 A543-A553 (2006).
38. X. Ren and S. Gottesfeld, "Electro-osmotic Drag of Water in Poly(perfluorosulfonic acid) Membranes," *J. Electrochem. Soc.* **148** (1), A87-A93 (2001).

39. V.S. Bagotzky, Y. Vassiliev and O.A. Khazova, "Generalized scheme of chemisorption, electrooxidation and electroreduction of simple organic compounds on platinum group metals," *J. Electroanal. Chem.*, **81** (2), 229-238 (1977).
40. T. Biegler and D.F.A. Koch, "Adsorption and Oxidation of Methanol on a Platinum Electrode," *Electrochem. Soc.*, **114** (9), 904-909 (1967).
41. M.W. Breiter, "Comparative oxidation of chemisorbed carbon monoxide, reduced carbon dioxide and species formed during the methanol oxidation," *J. Phys. Chem.*, **19** (1-2) 131-136 (1968).
42. M.R. Andrew and R.W. Glazebrook, *An Introduction to Fuel Cells*, (Elsevier Pub. Co., Amsterdam, New York, 1966) pp. 127.
43. C. Ponce de Leon, A Frias-Ferrer, J. Gonzalez Garcia, D.A. Sz'anto and F.C. Walsh, "Redox flow cells for energy conversion," *J. Power Sources*. **160**, 716-732 (2006).
44. L.H. Thaller in *PV 9th Intersociety Energy Conversion Engineering Conference Proceedings*, San Francisco, CA, USA, 1974 pp. 924-928.
45. J. Giner, L. Swette and K. Cahill, "Screening of Redox Couples and Electrode Materials," NASA-CR-134705, (1976).
46. M. Kazacos, D. Kasherman, D.R. Hong and M. Kazacos, "Characteristics and performance of 1 kW UNSW vanadium redox battery," *J. Power Sources.*, **35** (4), 399-404 (1991).
47. Q. Lao, H. Zhang, J. Chen, P. Qian and Y. Zhai, "Modification of Nafion membrane using interfacial polymerization for vanadium redox flow battery applications," *J. Membrane Sci.*, **311**, 98-103 (2008).

48. Y.Y. Wang, M.R. Lin and C.C. Wan, "A study of the discharge performance of the Ti/Fe redox flow system," *J. Power Sources*, **13** (1), 65-74 (1984).
49. T. Mohammadi and M. Skyllas-Kazacos, "Characterisation of novel composite membrane for redox flow battery applications," *J. Membr. Sci.*, **98** (1-2), 77 (1995).
50. M. Kazacos, M. Cheng and M. Skyllas-Kazacos, "Vanadium redox cell electrolyte optimization studies," *J. Appl. Electrochem.*, **20** (3), 463-467 (1990).
51. M. Skyllas-Kazacos, A. Mousa, and M. Kazacos, PCT Application, PCT/GB2003/001757, (April, 2003).
52. M. Skyllas-Kazacos and Y. Limantari, "Kinetics of the chemical dissolution of vanadium pentoxide in acidic bromide solutions," *J. Appl. Electrochem.*, **34**, (2004).
53. P. Lex and B. Jonshagen, "The zinc/bromine battery system for utility and remote area applications," *Power Engineering Journal.*, **13** (3), (1999).
54. R.B. Hodgdon, W.A. Waite and S.S. Alexander, NASA CR-174725, DOE/NASA/0264-1, (1984).
55. M. Lopez de Atalaya, G. Codina, J.R. Perez, M.A. Climent, J.L. Vazquez, and A. Aldaz, "Behaviour of the Cr(III)/Cr(II) reaction on gold-graphite electrodes. Application to redox flow storage cell," *J. Power Sources*, **35** 225 (1991).
56. G. Codina, J.R. Perez, M. Lopez-Atalaya, J.L. Vazquez and A. Aldaz, "Development of a 0.1 kW power accumulation pilot plant based on an Fe/Cr redox flow battery Part I. Considerations on flow-distribution design," *J. Power Sources*, **48** 293, (1994).
57. G. Kear, A.A. Shah and F.C. Walsh, "Development of the all-vanadium redox flow battery for energy storage: a review of technological, financial and policy aspects," *Int. J. Energy Res.*, **36** (11), (2011).

58. B.Dunn, H. Kamath and JM Tarascon, "Electrical Energy Storage for the Grid: A Battery of Choices," *Science.*, **18** (334), 928-935 (2011).
59. F. Moraw, K. Fatih, D. Wilkinson and F. Girard, "Evaluation of the Fe(III)/Fe(II) redox fuel cell cathode couple in a bioelectrolytic solution," *Advanced Materials Research Vols.* , 15-17, pp. 315-320 (2007).
60. K. Fatih, D.P. Wilkinson, F. Moraw, A. Ilicic and F. Girard, "Advancements in the direct hydrogen redox fuel cell," *Electrochem. And Solid-State Letters*, **11** (2), (2008).
61. A.B. Ilicic, D.P. Wilkinson, K. Fatih and F. Girard, "High fuel concentration direct-liquid fuel cell with a redox cathode couple," *J Electrochem. Soc.*, **155** (12), B1322-B1327 (2008).
62. F. C. Anson, "Exchange current densities for Fe(II)-Fe(III) solutions in sulfuric acid and perchloric acid," *Anal. Chem.*, **33** (939), (1961).
63. A. Damjanovic, A. Dey and J. O. Bockris, "Kinetics of oxygen evolution and dissolution on Pt electrodes," *Electrochim. Acta*, **11** 376, (1966).
64. M.R. Ronholm, J. Warna, D. Valtakari, T. Salmi and E. Laine, "Kinetics and mass transfer effects in the oxidation of ferrous sulfate over doped active carbon catalysts," *Catalysis Today*, **66**, 447-452 (2001).
65. M. Bartolozzi, "Development of redox flow batteries. A historical bibliography," *J. Power Sources*, **27** 219, (1989).
66. D. Karamanev, PCT no. PCT/CA04/00943 (2004), U.S. Pat. Appl., 20 060 251 959.
67. A.B. Ilicic, D.P. Wilkinson and K. Fatih, "Advancing Direct Liquid Redox Fuel Cells: Mixed-Reactant and In Situ Regeneration Opportunities," *J Electrochem. Soc.*, **157** 4, (2010).

68. A.B. Ilicic, M.S. Dara, K. Fatih and D.P. Wilkinson, "Improved performance of the direct methanol redox fuel cell," *J Appl. Electrochem.*, **40** (4), 2125-2133 (2010).
69. A. Lam, D.P. Wilkinson and J. Zhang, "Novel approach to membraneless direct methanol fuel cells using advanced 3D anodes," *Electrochimica Acta*, **53**, 6890–6898 (2008).
70. E. Kjeang, N. Djilali and D. Sinton, "Microfluidic fuel cells: A Review," *Journal of Power Sources*, **186**, 353–369 (2009).
71. A.K. Shukla, R.K. Raman and K. Scott, "Advances in mixed-reactant fuel cells," *Fuel Cells*, **4**, 436-447 (2005).
72. M.A. Priestnall, V.P. Kotzeva, D.J. Fish and E.M. Nilsson, "Compact mixed reactant fuel cells," *Journal of Power Sources*, **106**, 21-30 (2002).
73. R. Battino, T.R Rettich, T. and Tominaga, "The solubility of oxygen and ozone in liquids," *J. Phys. Chem. Ref. Data*, **12** (163), (1983).
74. F.C. Walsh, *A First Course in Electrochemical Engineering*, (The Electrochemistry Consultancy, Burlington, 1993)
75. A. Lam, M. S. Dara, D.P. Wilkinson and K.Fatih, "Aerboic and anaerobic operation of an active membraneless direct methanol fuel cell," *Electrochem. Comm.*, **17**, (2012).
76. M.R. Ronholm, J. Warna, T. Salmi, I. Turunen and M. Luoma, "Kinetics of oxidation of ferrous sulfate with molecular oxygen," *Chemical Engineering Science*, **54**, 4223-4232 (1999).
77. M.R. Ronholm, J. Warna, D. Valtakari, T. Salmi and E. Laine. "Kinetics and mass transfer effects in the oxidation of ferrous sulfate over doped active carbon catalysts," *Catalysis Today*, **66**, 447-452 (2001).

Appendix A – Catalyst Spraying Instructions

Pt/C/Nafion Ink Preparation + Spraying Instructions (v1.4)

- 1) Choose an appropriate catalyst loading (ex. 2 mg/cm²).
- 2) Calculate the mass of Pt/C powder mixture that should be used:

Notes for calculation

-Catalyst loading symbolized by $\sigma_{Catalyst}$ (mg per geometric cm²; actual can be calculated later)

-The catalyst is purchased as a dispersed deposit on Vulcan XC carbon powder. Some common compositions of this powder based on mass are given: (20% Pt, 80% C; etek-inc.com ~\$1500/100g), (40% Pt, 60% C), (20% Pt, 20% Ru, 60% C) and (10% Pt, 10% Ru, 80% C). The following example uses the last composition. Let $f_{Catalyst}$ denote the mass fraction of catalyst on the carbon

-To account for losses (i.e. off-edge spraying, air-borne spray) while spraying the ink, the premixed

Pt/C is added with an excess factor of 3 for hand-spraying or 2 for the automatic sprayer, which may vary with preference, technique or procedure.

-The active area for the automatic sprayer is 11cm x 11cm, which equates to 121 cm².

$$m_{Catalyst+VulcanXC} = \frac{E\sigma_{Catalyst}A_{Geom}}{f_{Catalyst}}$$

$$\text{Ex. } m_{Catalyst+VulcanXC} = \frac{(2)\left(2\frac{mg}{cm^2}\right)(121cm^2)}{(0.2)}\left(\frac{1g}{1000mg}\right) = 2.42g$$

- 3) Choose an appropriate Nafion loading (~30% w/w is common). Sprayed Nafion provides bonding when pressing the MEA and increases the triple-phase boundary length.
- 4) Calculate the mass of Nafion solution required:

Notes for calculation

-Nafion loading is symbolized as f_{Nafion} (fraction Nafion in catalyst + Vulcan XC + Nafion)

-Nafion is available as a 5% w/w solution. Mass of solution expressed as m_{Naf_Sol}

$$m_{Naf_Sol} = \frac{f_{ionomer}m_{Catalyst+VulcanXC}}{1-f_{ionomer}}\left(\frac{1}{f_{ionomersolution}}\right)$$

$$\text{Ex. } m_{Naf_Sol} = \frac{(0.3)(2.42g)}{(1-0.3)}\left(\frac{1}{0.05}\right) = 20.74g$$

-The derivation can be realized by starting with:

$$m_{Nafion} = f_{Nafion}(m_{Catalyst+VulcanXC} + m_{Nafion})$$

- 5) Clean an appropriate size beaker with isopropanol.
- 6) Weigh the calculated amount of premixed Catalyst/C powder in the beaker.
- 7) Add water (before adding isopropanol) to the weighed powder. The carbon powder will agglomerate over the water surface. Submerge as much of the carbon powder as possible by stirring.
- 8) Add isopropanol (after adding water) to completely solvate the carbon powder. Try to obtain reasonable dispersion by stirring. One can constantly adjust the amount of water and isopropanol added to find what works best. Generally, much less isopropanol is added than water. If the isopropanol is added before water, the carbon powder and isopropanol will combust together.
- 9) Add the calculated mass of Nafion solution (after adding water) with a micropipette. Stir.
- 10) Cover the mixing beaker with parafilm and sonicate the mixture for 30-60 min. Inspect and stir the mixture every 10-15 minutes. A homogenous dispersion is desired.

If you are using the automatic sprayer, spray the catalyst while periodically measuring the change in weight. Once you have the desired loading, proceed to step 19).

Notes for Calculation

-The weight change is determined from the catalyst loading, mass fraction of catalyst on carbon

- 11) Thoroughly clean the spray gun with isopropanol.
- 12) Release the trigger while attaching the purple nozzle to ensure a tight fit.
- 13) Ensure that the purple nozzle cover is horizontal.
- 14) Partially pressing the spray gun trigger will permit air to pass through the nozzle, but not ink. While shooting air, adjust the air pressure to read 15psi. The pressure should be greater than 15psi after releasing the trigger.
- 15) Select your substrate and record the initial weight. The difference between this weight and the weight after spraying indicates the catalyst loading.
- 16) Set the hotplate to 3 (~80°C).
- 17) Pour approximately 2/3 of the prepared ink into the spray gun. Spray all of it, acknowledging that it won't be enough to overspray. Spraying an electrode for use in a fuel cell should be done only after practicing proper spraying techniques. Some general guidelines:
 - a) Point the spray gun perpendicular to the substrate plane while spraying. If a perfectly perpendicular gun alignment is uncomfortable, be sure to carefully spray the edge that is affected by the angle.
 - b) Spray the substrate in a variety of directions to obtain an even loading (horizontally, vertically, diagonally etc.). Spray the entire substrate one direction at a time.

- c) Move the spray gun at a constant velocity.
 - d) Choose whether you prefer to spray continuously or line after line. Find what works best for you.
 - e) If spraying continuously, exercise caution when approaching the edges and changing the direction of gun movement. Changing direction too slowly can result heavier loadings around the edges. Change direction when the gun is over the protective border.
 - f) If spraying line by line, exercise caution when pressing and releasing the gun trigger. Both actions should be done when the gun is over the protective border.
 - g) Spray slowly.
- 18) Add the last third of the ink to the gun and weigh the sprayed substrate periodically to achieve your desired catalyst loading.
- 19) Place the sprayed substrate in the oven at 80°C for 30min to remove the water and isopropanol.

Adding a Sublayer

- 1) Decide if you want to add a sublayer, which is a sprayed layer of carbon and Teflon (PTFE) underneath your catalyst layer. A sublayer serves as a hydrophobic layer to enhance water removal and can significantly improve electrode performance. A sublayer is frequently added for hydrogen anodes and oxygen cathodes.
- 2) Choose an appropriate Teflon loading. (0.2 mg/cm² is common). The Teflon is available as a 60% w/w solution.
- 3) The ink will be comprised of 20% Teflon and 80% C w/w (excluding the Teflon solvent, water and isopropanol). Calculate the amount of Teflon solution and carbon needed for the ink:

Notes for calculation

-An excess factor of 3 is used here as well.

$$m_{PTFE} (g) = 3\sigma_{PTFE} A_{Geom} \left(\frac{1g}{1000mg} \right)$$

$$m_{PTFE_Sol} (g) = \frac{m_{PTFE}}{0.6}$$

and finally,

$$m_{VulcanXC} (g) = 4m_{PTFE}$$

- 4) Combine the Vulcan carbon and the Teflon solution with some water and isopropanol to obtain the ink. Go back to step 10. Note that 1mg/cm² would have to be sprayed here in order to obtain a PTFE loading of 0.2mg/cm² since the solids after drying the sprayed ink contain only 20% PTFE.
- 5) The PTFE needs to be sintered to achieve good hydrophobicity. Sinter the sublayer in the oven at 350°C for 30min. (Obviously you can exclude step 19).

MEA Pressing

- 1) Choose an appropriate pressing temperature (135°C is common).
- 2) Turn on the heating panel on the press. It is the left switch.
- 3) Set plates 1 and 2 to the desired temperature by pressing the arrow buttons. The top temperature is the current reading and the bottom is target temperature.
- 4) Choose an appropriate pressure to press at. Note that only the force can be set on the machine, thus you will have to calculate the resulting pressure based on the dimensions of your MEA. Titichai recommends operating between 75-220 kg/cm² (340-1000 psi).
- 5) Turn on the power panel on the press.
- 6) Decide whether you want to operate the press in manual or automatic mode. Automatic is easier.
- 7) In automatic mode, do the following to set your MEA pressing conditions:
 - a) Press “Menu” until you see “View/Edit Recipe”.
 - b) Press “Set”. Enter the desired force with the up and down buttons. 700 lbs is the minimum.
 - c) Press “Set”. Enter the desired pump speed with the up and down buttons. A low pump speed will minimize force overshoot when pressing. At the minimum force, even the minimum pump speed will exhibit 100-200lbs of overshoot. The higher the target force, the lower the overshoot. The minimum pump speed is 15%.
 - d) Press “Set”. Choose the units you wish to count down in.
 - e) Press “Set”. Select the duration of the press. (3 minutes is common)
 - f) Press “Menu” twice to go back to “Carver”. The press is now ready.
- 8) Prepare a Niobium/Teflon/MEA/Teflon/Niobium sandwich. The Teflon can be omitted if you think over-adhesion to the niobium sheets will not be a problem.
- 9) Press the MEA by holding the two green buttons until the press has closed and afterwards carefully peel the MEA away from the pressing sheets.

**Appendix B – Detailed Dimensions of Flow Field
Channels and Flow Field Plates**

All dimensions in millimetres.

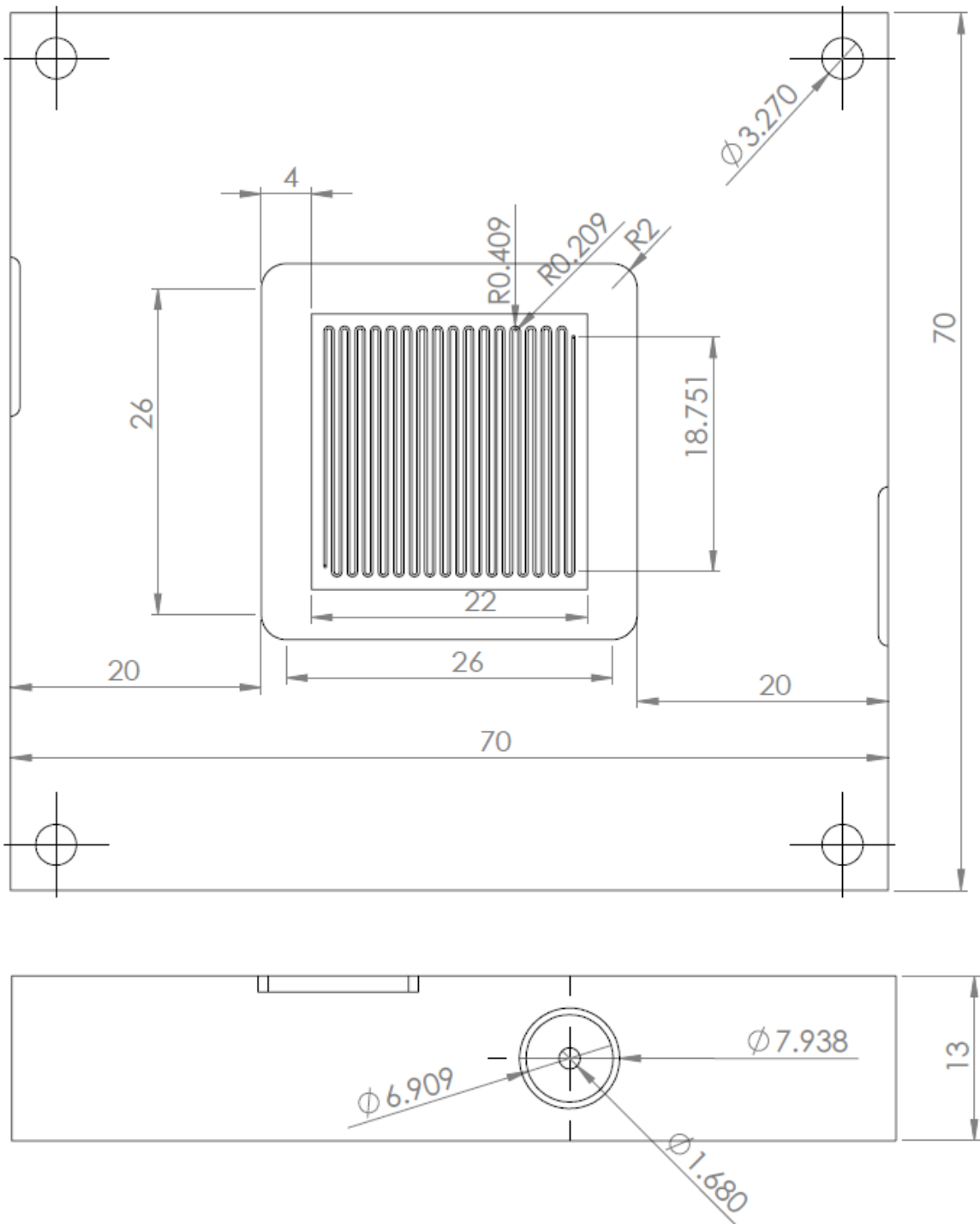


Figure B.1: Detailed drawings of the anode flow channels. Top: Bird's eye view of channels face. Bottom: View of thickness of plate. All dimensions in millimetres.

All dimensions in millimetres.

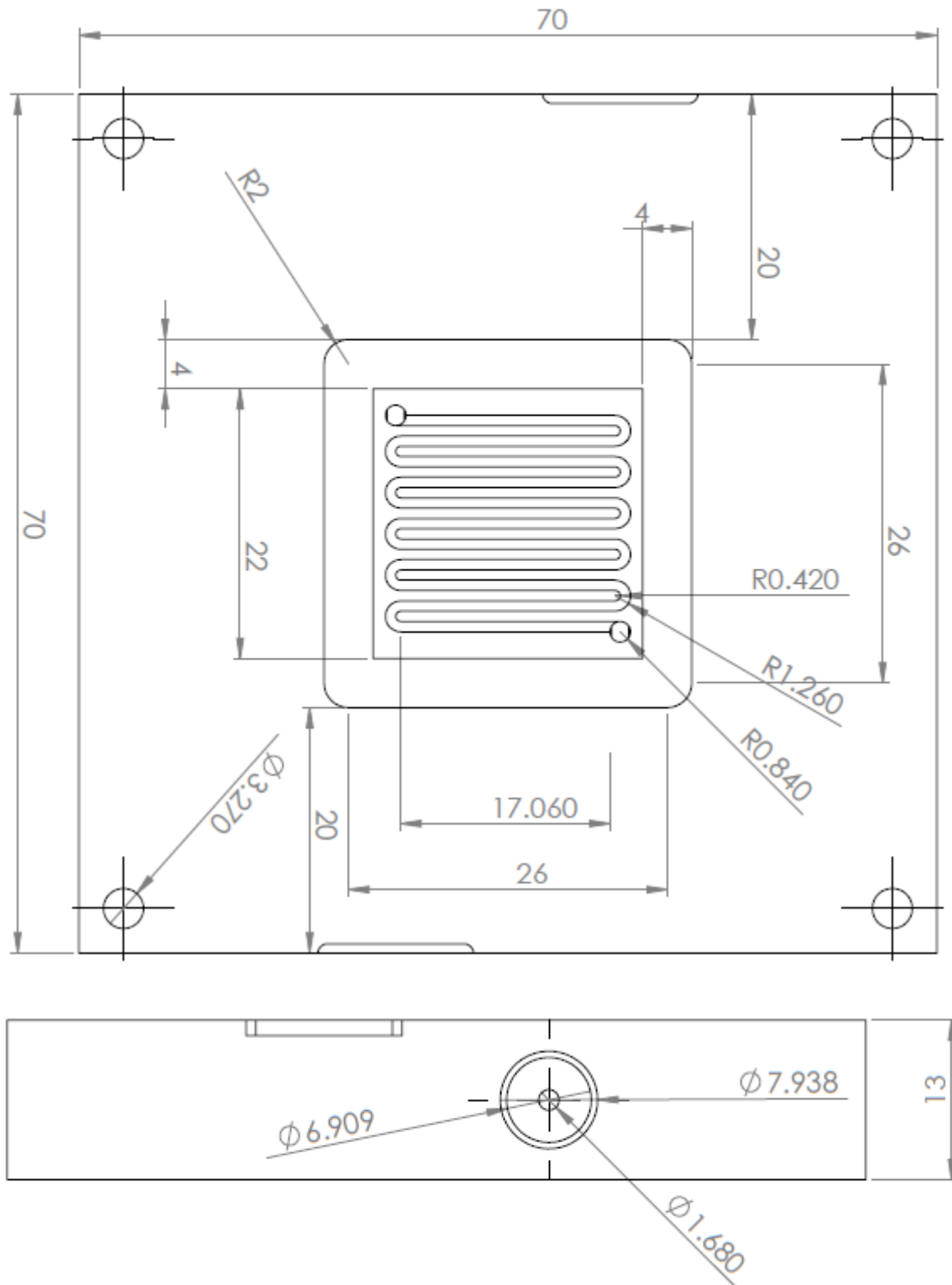


Figure B.2: Detailed drawings of the cathode flow channels. Top: Bird's eye view of channels face. Bottom: View of thickness of plate. All dimensions in millimetres.

**Appendix C – iR-Corrected Polarization and Power
Density Curves**

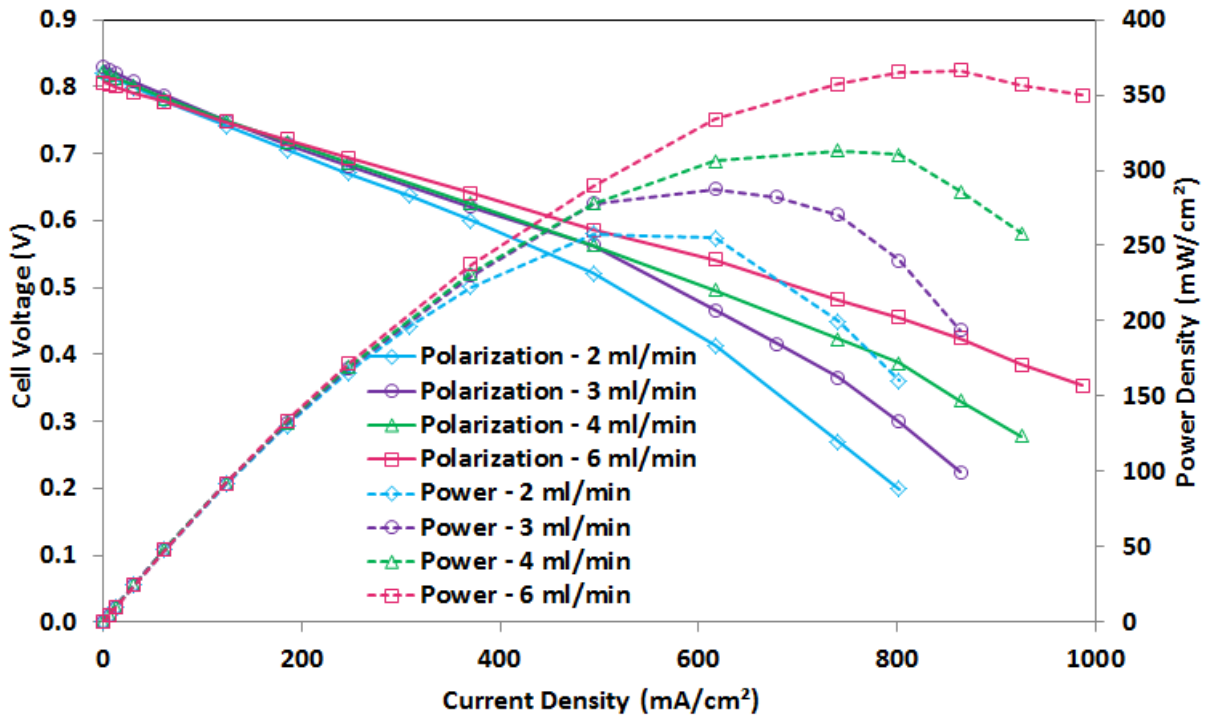


Figure C.1: iR-Corrected polarization curves for the effect of iron redox catholyte flow rates of fuel cell performance at 60°C. See Figure 6.3.

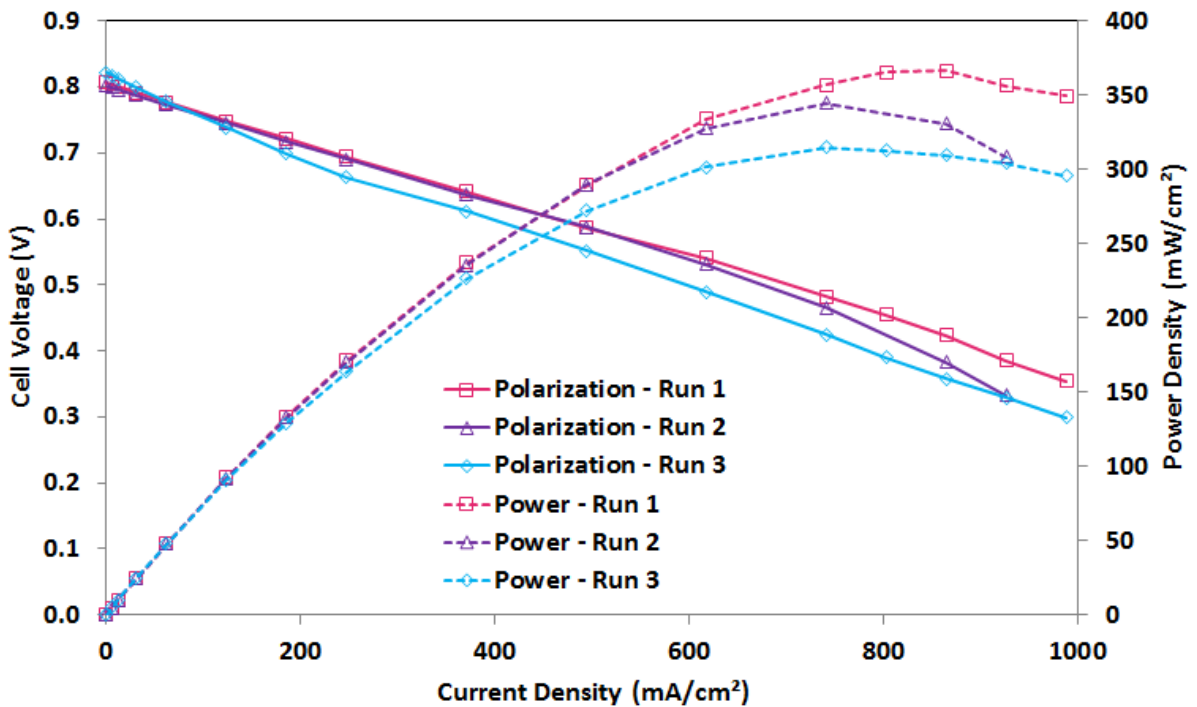


Figure C.2: iR-corrected fuel cell performance repeatability with new components for all three runs at 60°C. See Figure 6.4.

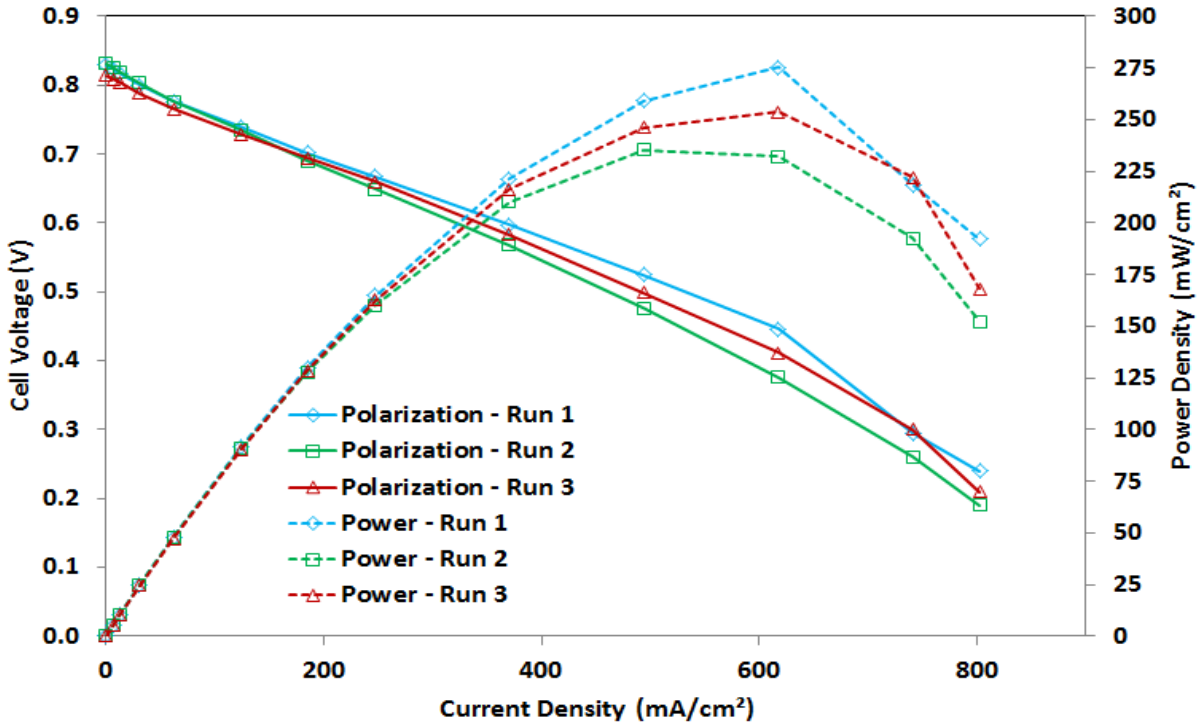


Figure C.3: iR-corrected fuel cell performance repeatability with the same membraneless electrode assembly at 60°C. See Figure 6.5.

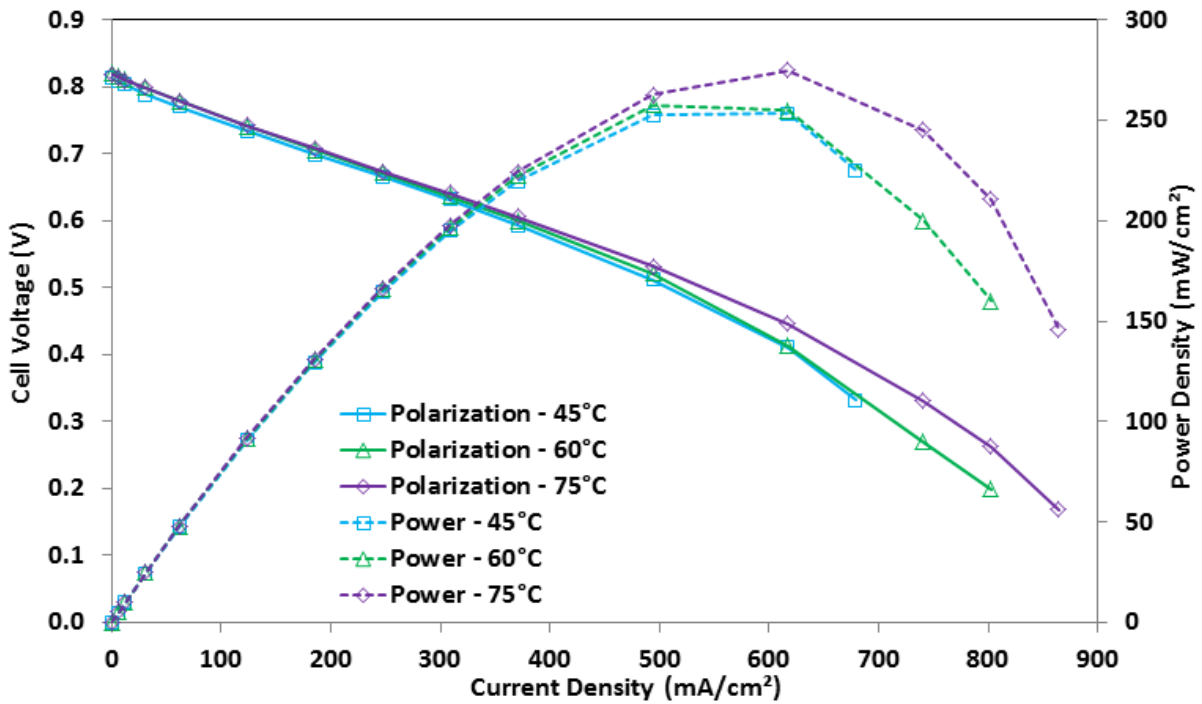


Figure C.4: iR-Corrected polarization curves for the effect of temperature on fuel cell performance. See Figure 6.6.

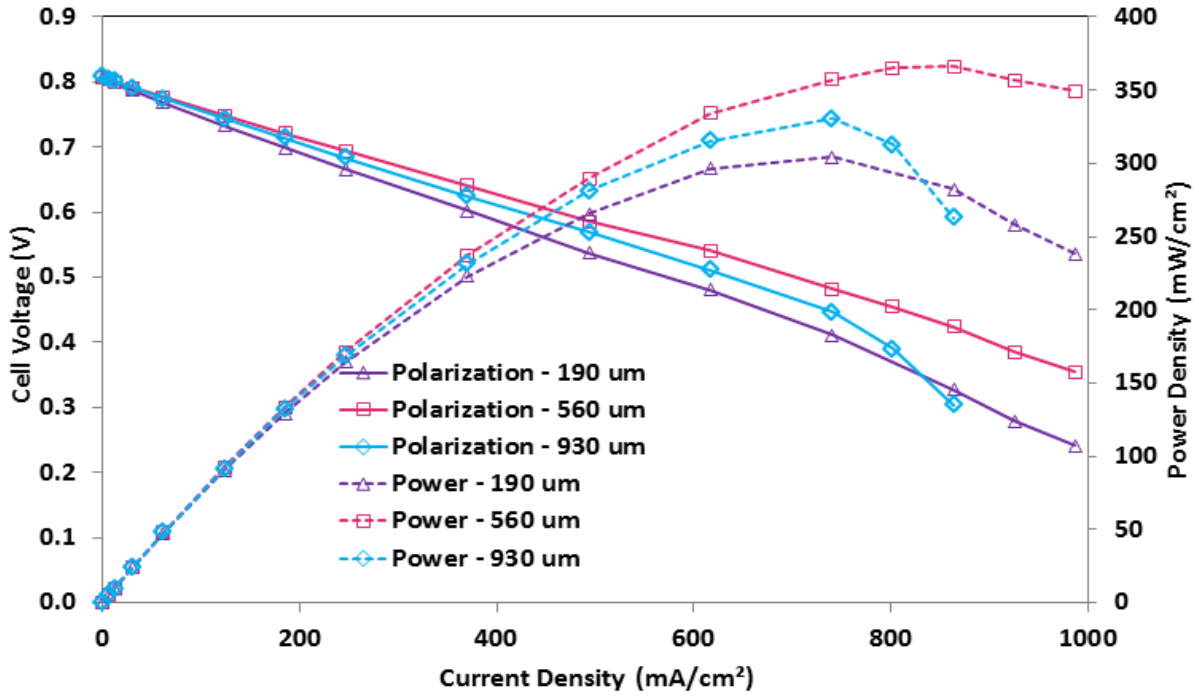


Figure C.5: iR-corrected polarization curves for the effect of 3-D cathode thickness on fuel cell performance at 60°C. See Figure 6.10.

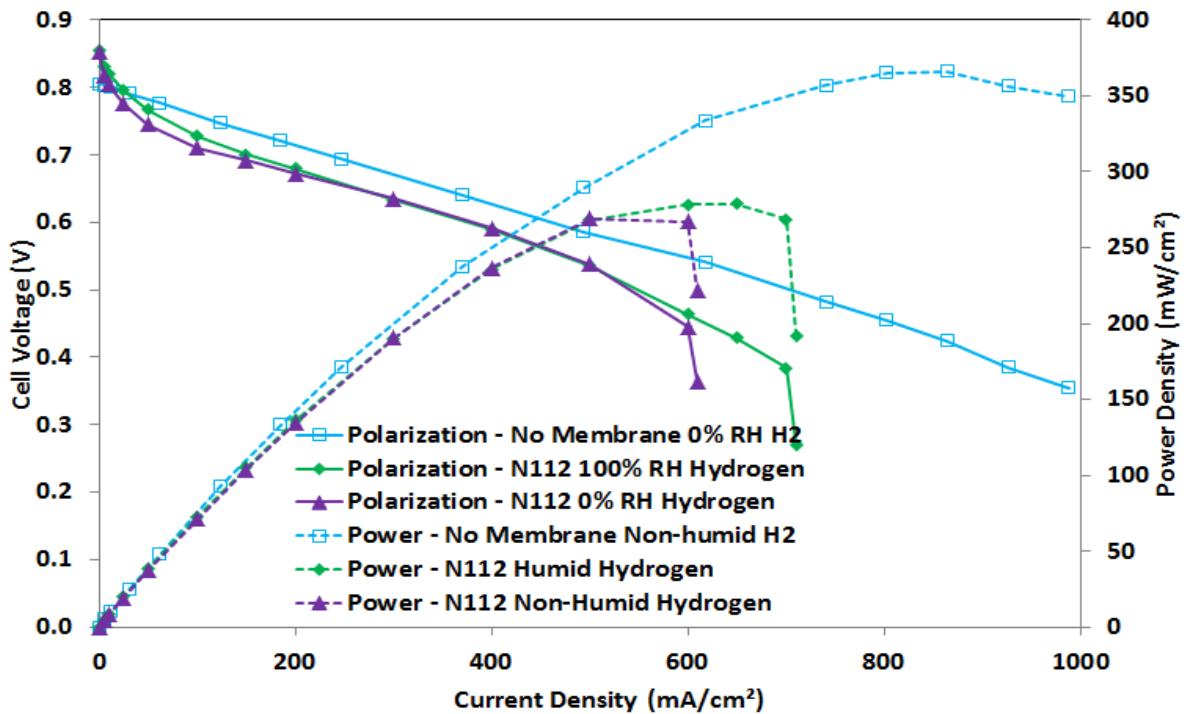


Figure C.6: iR-corrected comparison of polarization curves of the non-humidified fuel membraneless DHRFC with a humidified and non-humidified fuel Nafion® 112 DHRFC. See Figure 6.14.

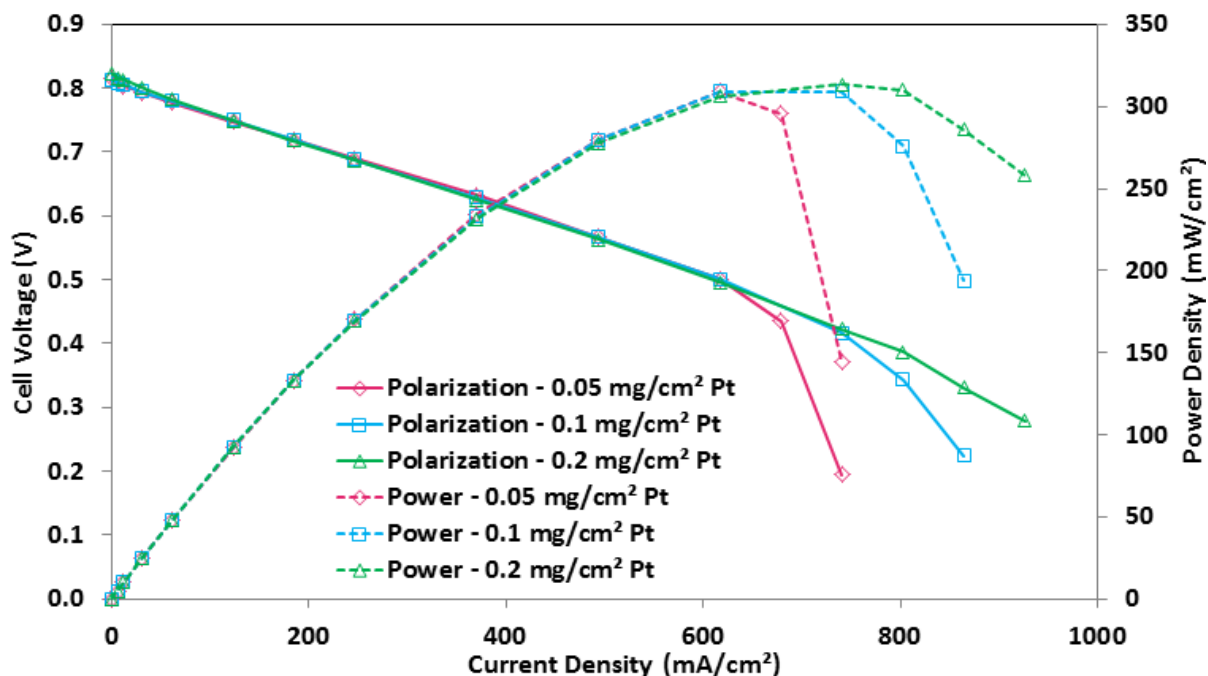


Figure C.7: iR-corrected polarization curves showing the effect of anode Pt catalyst content on fuel cell performance at 60°C. See Figure 6.15.

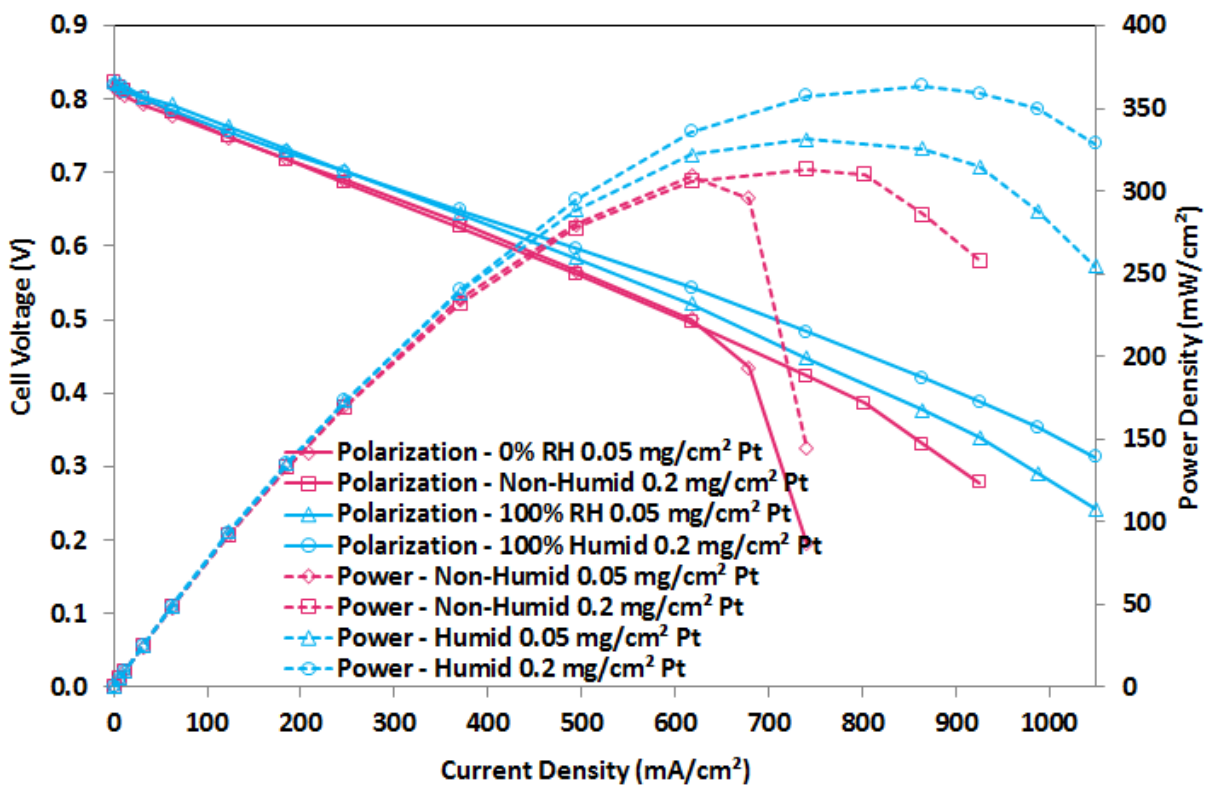


Figure C.8: Effect of hydrogen fuel humidification on fuel cell performance for different anodes at 60°C. See Figure 6.16.

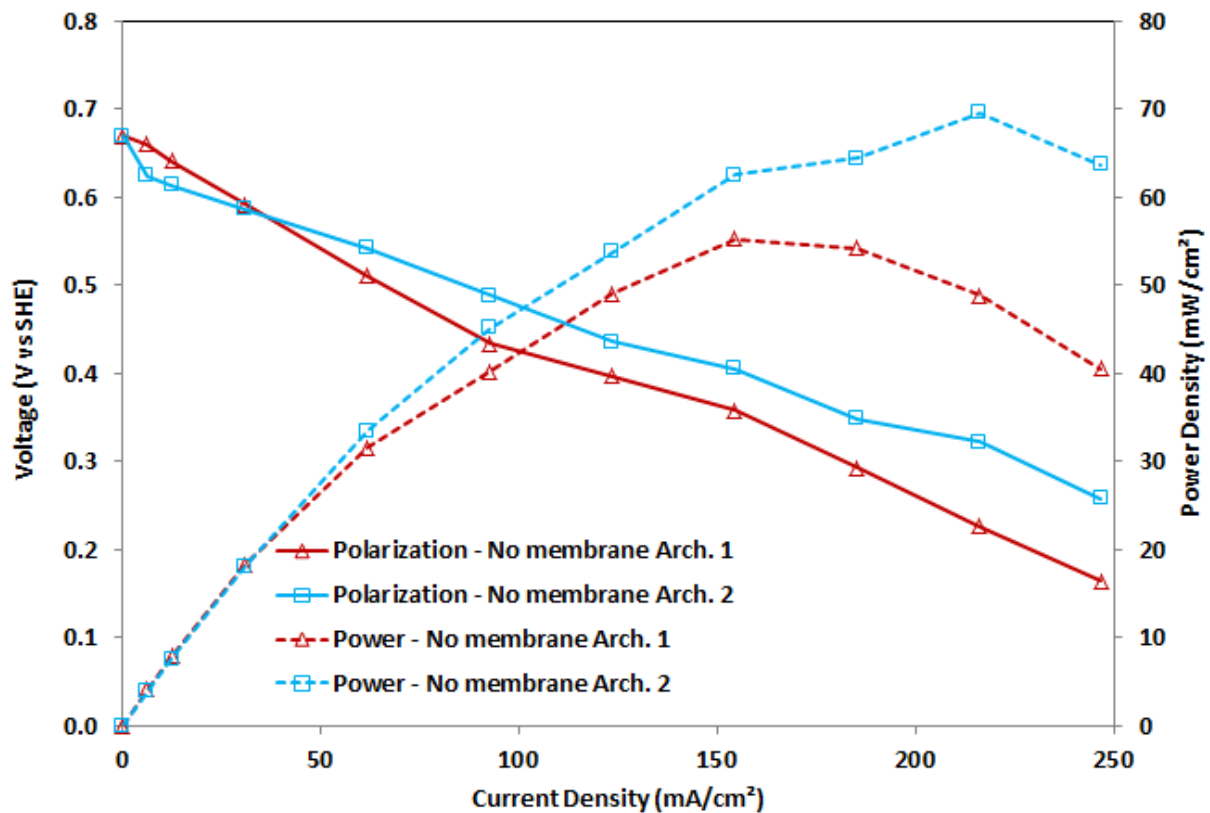


Figure C.9: *i*R-corrected comparison of different 3-D cathode architectures on membraneless DMRFC performance. See Figure 6.26.

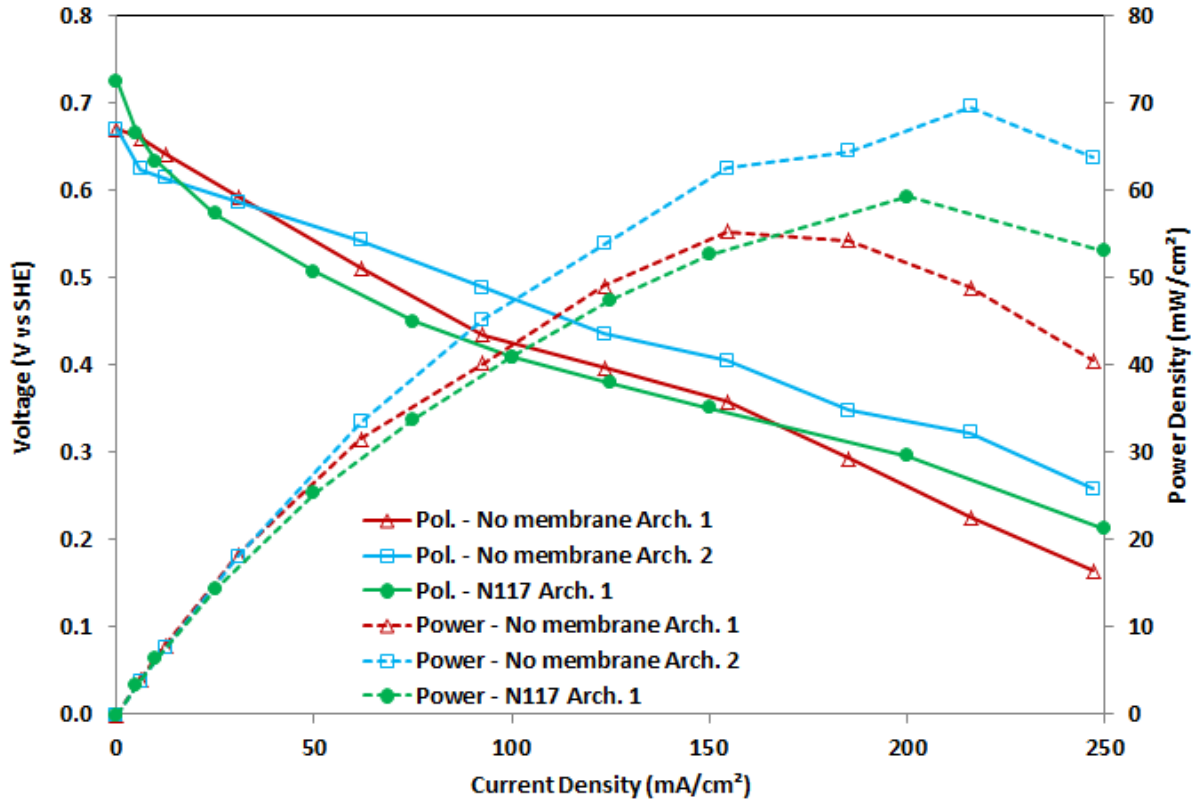


Figure C.10: iR-corrected comparison of membraneless DMRFC performance with a conventional Nafion 117 based DMRFC. See Figure 6.28.

Appendix D – Publications and Presentations

Publications

- M. S. Dara, D.P. Wilkinson, A. Lam and K.Fatih “Low Pt-loading Membraneless Hydrogen Redox Fuel Cell” – *Electrochemical Society Transactions*, submitted July 2012.
- A. Lam, M. S. Dara, D.P. Wilkinson and K.Fatih. “Aerobic and Anaerobic Operation of an Active Direct Methanol Fuel Cell” *Electrochemistry Communications* 17 (2012)
- A. B. Ilicic, M. S. Dara, D. P. Wilkinson and K. Fatih. “Improved performance of the direct methanol redox fuel cell” *Journal of Applied Electrochemistry* 40 12 (2010)

Presentations

- “Aerobic and Anaerobic Operation of an Active Direct Methanol Fuel Cell”. M. S. Dara, A. Lam and D.P. Wilkinson. Meeting of the Electrochemical Society, May 2012, Seattle, WA, USA
- “Low-cost Hydrogen Fuel Cell”. M. S. Dara, A. Lam and D.P. Wilkinson. Meeting of the Electrochemical Society, May 2012, Seattle, WA, USA